Trapping Low Energy Antiprotons in an Ion Trap

A thesis presented

by

Xiang Fei

to

The Department of Physics

in partial fulfillment of the requirements

for the degree of

Doctor of Philosophy

in the subject of

Physics

Harvard University

Cambridge, Massachusetts

September, 1990

Abstract

A fraction of antiprotons from the Low Energy Antiproton Ring (LEAR) of CERN are slowed from 5.9 MeV to below 3 keV as they pass through thin foils. Transmitted particle energy distribution and low energy antiproton yield are measured by a time-of-flight technique. The difference in the range of protons and antiprotons (known as the Barkas effect) is observed. While still in flight, up to 1.3×10^5 antiprotons with energies between 0 eV to 3 keV are stored in an ion trap from a single pulse of 5.9 MeV antiprotons leaving LEAR, thus a trapping efficiency exceeding of 4×10^{-4} is established. Trapped antiprotons maintain their initial energy distribution unless allowed to collide with a cloud of trapped electrons, whereupon they slow and cool below 1 meV in 10 s, and fall into a harmonic potential well suited for precision mass measurements. The slowing, trapping and cooling of antiprotons are the main focus of this thesis. The stored antiprotons are in thermal equilibrium at 4.2 K. In this ion trap, the antiproton cyclotron frequency is measured and compared with the proton (or electron) cyclotron frequency. Our new measured ratio of the antiproton and proton inertial masses, with its 4×10^{-8} uncertainty, is more than three orders of magnitude more accurate than previous measurements using exotic atoms. This is the most precise test of CPT invariance with baryons. The antiproton lifetime in an ion trap was measured to be more than 103 days by trapping a cloud of antiprotons for 59 days. This indicates the number density of atoms is less than $100/cm^3$ which corresponds to the pressure in the vacuum chamber being less than 5×10^{-17} Torr at 4.2 K if we apply the ideal gas law.

Contents

Acknowledgements

During my years of Ph.D. study, I have had help from many people. First I would like to thank my thesis advisor, Prof. Gerald Gabrielse, who led the TRAP (TRapped AntiProton) Collaboration and made this work possible. His ideas and insights can be found throughout this thesis. I benefitted a great deal from the other members of the TRAP Collaboration: Johannes Haas, Kris Helmerson, Dr. Hartmut Kalinowsky, Dr. William Kells, Dr. Luis A. Orozco, Dr. Steven L. Rolston, Robert L. Tjoelker, and Prof. Thomas A. Trainor. It is my great pleasure to acknowledge assistance from many people in the Department of Physics at Harvard University, the European Organization for Nuclear Research (CERN) and LEAR, and the Department of Physics at University of Washington during my stay there. While working with Prof. Trainor, we carried out the initial tests of slowing protons and of PPAC detectors at the Nuclear Physics Laboratory of University of Washington. I also appreciate help from my fellow graduate students Ching-Hua Tseng, Loren Haarsma, and Joseph Tan, and from Dr. Benjamin Brown, and Dr. Won Ho Jhe at various stages of this work. This work is supported by the National Science Foundation, the National Bureau of Standards (Precision Measurement Grant), and the Air Force Office of Scientific Research.

Papers published by the author during his Ph.D. study

1. *First capture of antiprotons in a Penning trap: a kiloelectronvolt source.*
   G. Gabrielse, X. Fei, K. Helmerson, S.L. Rolston, R. Tjoelker, T.A. Trainor, H. Kalinowsky, J. Haas, and W. Kells,
   Phys. Rev. Lett. **57**, 2504 (1986).

2. *High-voltage switching for in-flight capture of keV antiprotons in a Penning trap.*
   X. Fei, R. Davisson, and G. Gabrielse,
   Rev. Sci. Instrum. **58**, 2197 (1987).

3. *Barkas effect observed with antiprotons and protons.*
   G. Gabrielse, X. Fei, L.A. Orozco, S.L. Rolston, R.L. Tjoelker, T.A. Trainor, J. Haas, H. Kalinowsky, and W. Kells,
   Phys. Rev. **A40**, 481 (1989).

4. *Cooling and slowing of trapped antiprotons below 100 meV.*
   G. Gabrielse, X. Fei, L.A. Orozco, R.L. Tjoelker, J. Haas, H. Kalinowsky, T.A. Trainor, and W. Kells,
   Phys. Rev. Lett. **63**, 1360 (1989).

5. *Thousandfold improvement in the measured antiproton mass.*
   G. Gabrielse, X. Fei, L.A. Orozco, R.L. Tjoelker, J. Haas, H. Kalinowsky, T.A. Trainor, and W. Kells,
   Phys. Rev. Lett. **65**, 1317 (1990).

6. *Prospects for experiments with trapped antiprotons.*
G. Gabrielse, K. Helmerson, R. Tjoelker, X. Fei, T.A. Trainor, W. Kells, and H. Kalinowsky,
in **Proceedings of the first workshop on antimatter physics at low energy**, ed. by B.E. Bonner, L.S. Pinsky (Fermilab, Batavia, 1986), p.211.

7. *First antiprotons in an ion trap.*
G. Gabrielse, X. Fei, K. Helmerson, S.L. Rolston, R. Tjoelker, T.A. Trainor, H. Kalinowsky, J. Haas, and W. Kells,
in **Laser Spectroscopy VIII**, ed. by W. Persson and S. Svanberg, (Springer-Verlag, New York, 1987), p.22.

8. *First capture of antiprotons in an ion trap: progress toward a precision mass measurement and antihydrogen.*
G. Gabrielse, X. Fei, L. Haarsma, S.L. Rolston, R. Tjoelker, T.A. Trainor, H. Kalinowsky, J. Haas, and W. Kells,
Physica Scripta, **T22**, 36 (1988).

9. *Cryogenic antiprotons: a 1000-fold improvement in their measured mass.*
G. Gabrielse, X. Fei, W. Jhe, L.A. Orozco, J. Tan, R.L. Tjoelker, J. Haas, H. Kalinowsky, T.A. Trainor, and W. Kells,
in **Atomic Physics XII**. (1990).

List of Figures

Chapter 1

Introduction

1.1 Motivation and history

Low energy antiprotons in storage rings [1,2,3] make a large number of nuclear- and particle-physics experiments and a few atomic physics experiments possible. The availability of cold antiprotons with energies much lower than the beam energies in storage rings opens the way to various interesting experiments and important physics in a new range of the energy spectrum. A comprehensive description of slowing, trapping, and cooling antiprotons below 1 meV is given in this thesis. For the first time, antiprotons have been stored indefinitely in an ion trap, at energies 10 orders of magnitude lower than realized in any storage rings. This makes possible a new antiproton mass measurement [4], a direct antiproton lifetime measurement, and antiproton-atom interaction studies at low energies. In the future, the antiproton source in an ion trap can be compact and movable so that a series of experiments could be carried out in a non-accelerator environment. Trapped antiprotons can be used for possible antihydrogen production [5] and gravitational mass measurements [6]. The technology and experience gained during the trapping experiment are also important for other studies. For example, antiprotons make a very sensitive gauge for vacuum studies based on the antiproton lifetime measurement. An antideuteron mass measurement may be possible in a similar fashion as

for antiproton.

In early 1986, we first captured keV protons in an ion trap [7]. In April and May, we used a simple time-of-flight apparatus to measure the energy distribution of protons and antiprotons emerging from a thick degrader. A fraction of protons and antiprotons were slowed below 3 keV [8]. In July 1986, antiprotons were first captured in an ion trap by our TRAP Collaboration during a single 24 h period [9]. During the next two years, while the European Organization for Nuclear Research (CERN) was upgrading their antiproton facility, we prepared a new apparatus for slowing, trapping, and cooling of antiprotons, and for measuring the antiproton mass. Since September 1988, we have made great progress toward our goal [10,11,12] and thus laid the foundation for further achievement.

1.2 Slowing, trapping, and cooling antiprotons

Ultracold antiprotons of the order of meV are not available in any storage rings. Even the Low Energy Antiproton Ring (LEAR) which is the best low energy antiproton facility can only supply beams with an energy down to 5.9 MeV (a 3 MeV beam is now being developed at LEAR). This is 10 orders of magnitude higher in energy (see Fig. 1.1) than we desire (≈ 0.5 meV) for low energy antiproton physics experiments. The major challenge is to produce ultracold antiprotons from the high energy antiproton beams available from LEAR. Slowing antiprotons by atomic collisions and electron cooling is demonstrated in our experiments to be the solution.

Charged particles lose energy when they pass through matter, in collisions with bound electrons in the degrader which cause electron excitation and ionization. Due to the statistical behavior of such collisions, transmitted antiprotons

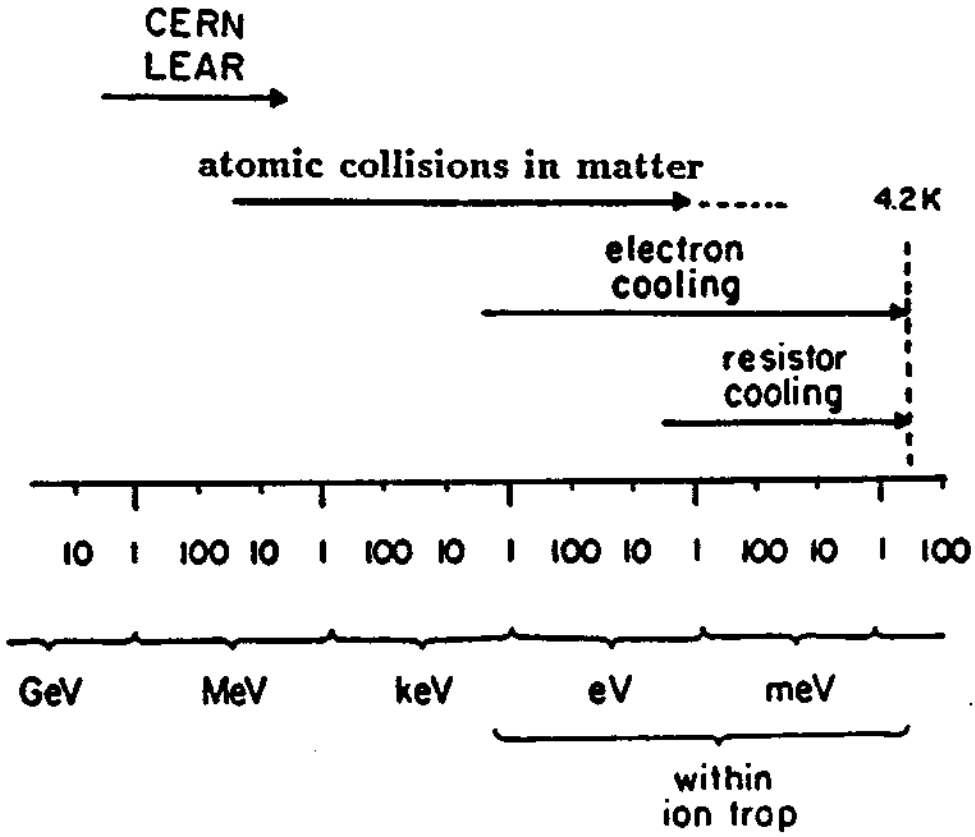

Figure 1.1: The energy span from the LEAR beam energy of about 10 MeV to the energy required for antiproton mass measurements and the methods to slow and cool antiprotons below meV.

have different energies. Only a very small fraction of them are below a few keV even when the degrader thickness is optimized for low energy antiproton yield. Great care must be taken to make the thickness of the degrader as close to the range of the energetic particles as possible. Tests with protons are carried out first due to very precious antiproton beam time. The difference in the range between protons and antiprotons (known as the Barkas effect) must be compensated by adding more material for antiproton experiments.

Our experiment shows that 10^4 to 10^5 antiprotons can be trapped routinely in a 3 keV potential well from one 300 ns pulse of 5.9 MeV antiprotons which contains up to 3×10^8 particles from LEAR [11]. The maximum number of antiprotons trapped from one pulse is 1.3×10^5 antiprotons. It is sufficient to use the degrader technique to slow antiprotons since we only need a modest number of antiprotons to perform some needed experiments. A single antiproton in the trap will eventually be used for the mass measurement. However, more antiprotons are demanded for other experiments.

Antiprotons are initially stored in a long (13 cm) ion trap with energies ranging from 0 eV to 3 keV. If a large number of electrons can be loaded in the center part (approximately 0.5 cm long) of the long trap, antiprotons oscillating through the bound electron cloud will lose kinetic energy the same way as in the material except no annihilations will occur [4]. The electrons rapidly radiate the excess heat from the hot antiprotons via synchrotron radiation. The slowing efficiency for antiprotons is nearly 100%. The slowing process within the ion trap effectively reduces antiproton random energies in 3 dimensions. Therefore it is also a cooling process. This is the first time that electron cooling has been applied in an ion trap.

Fig. 1.1 shows the energy span from the LEAR beam energy of about 10 MeV to below meV. Atomic collisions in matter reduce some particle energies to keV

so they can be trapped in an ion trap. Very a few particles have energies less than 100 meV. Further slowing and cooling are accomplished by electron cooling which is very effective and efficient. A thermal equilibrium state can be achieved at 4.2 K. Resistor cooling can damp and maintain the antiproton motions in thermal equilibrium, once most of the antiproton's energy is removed by the electrons.

1.3 Antiproton mass measurement

The antiproton inertial mass $m_{\bar{p}}$ is an important physical quantity. It is of great interest to make increasingly precise measurements of such a basic quantity. High precision measurements of the mass ratio of antiproton to proton also provide experimental verification of the CPT theorem, thus increasing our confidence in this basic symmetry in nature. The CPT theorem states that any quantum field theory described by a local Lorentz-invariant Hermitian Hamiltonian is invariant under the operations of charge conjugation (C), parity inversion (P), and time reversal (T) in any order [13]. The theorem implies that a particle and its antiparticle must have the same magnetic moment (with opposite sign), the same mass, and the same mean life.

When the antiproton was discovered at the University of California at Berkeley in 1955 [14], the new negatively charged particle was identified as the antiproton mainly because it has a mass within 5% of the proton mass. Using an exotic-atom method, the inertial mass of the antiproton was measured to higher precision at the Proton Synchrotron (PS) of CERN [15]. Antiprotons stopped in a thallium target were captured into orbits with high principal quantum numbers. In the antiprotonic atom, the energy eigenvalues are proportional to the reduced mass of the hadron-nucleus system. By measuring the transition energies of X-rays originated from the antiprotonic cascade and making comparisons with the calculated

ones, the inertial mass of the antiproton was deduced. Similar experiments were performed at Brookhaven National Laboratory [16,17,18] using various targets. A fractional uncertainty of 5×10^{-5} was achieved in the most accurate measurement and it is consistent with the much better known proton mass (see Fig. 1.2). Due to the complexity of the antiprotonic system, many corrections, such as nuclear finite-size effects, radiative corrections, interactions between the antiproton and higher moments of the nucleus, electron screening, and the anomalous magnetic moment of the antiproton, were needed to obtain the quoted precision.

The lowest energy antiproton beam in a storage ring is on the order of MeV at LEAR of CERN. Further deceleration to meV or below, 10 orders of magnitude lower in energy, can be achieved by inelastic collisions with electrons in degraders and in ion traps. A much more accurate measurement of the antiproton inertial mass becomes feasible with cold antiprotons by well established Penning trap technique once antiprotons are confined in the trap. An ion trap is a device to hold charged particles in the combination of a homogeneous magnetic field and an electrostatic potential. The ion trap technique has been widely used for high precision measurements of fundamental constants and mass comparisons [19,20]. The g factor (representing the magnetic moment of the particle) of the electron has been measured to a fractional uncertainty of 4×10^{-12} [21]. This allows the most precise comparison between theory and experiment for a property of an elementary particle. Its agreement with theory is the most accurate test for Quantum Electrodynamics (QED) theory. Precise measurements of the g factor ratio [21] for electron and positron, with an accuracy of 2×10^{-12}, provide a stringent test of the CPT theorem for leptons. The proton-electron mass ratio previously measured by the ion trap technique [22,23] has an uncertainty of 2×10^{-8}. A mass ratio measurement for single CO^+ and N_2^+ ions with an accuracy of 4×10^{-10} has been reported [20].

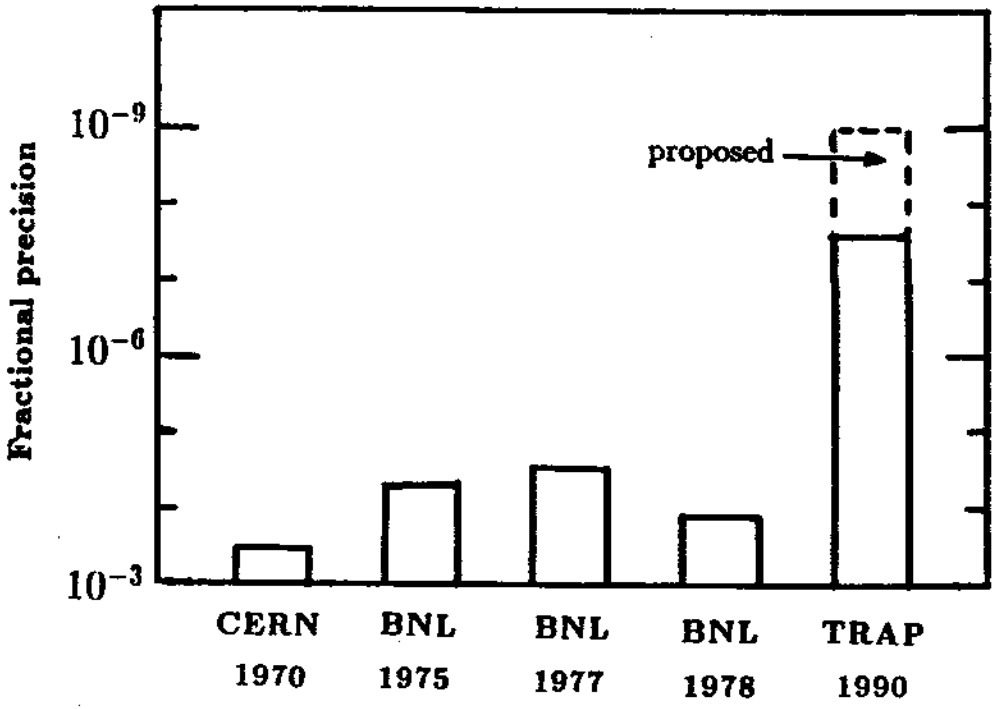

Figure 1.2: The fractional accuracy of antiproton mass measurements by exotic atom methods and by the ion trap technique.

The principle of ion trap mass spectroscopy for ion mass comparison is very simple and elegant. A particle of charge q and mass m in a uniform and stable magnetic field B undergoes a constant circular motion (cyclotron motion) around a magnetic field line with frequency $\omega_c = qB/mc$ with c the speed of light. If a second particle with a different charge and mass is placed in the same magnetic field, the ratio of cyclotron frequencies gives the ratio of charge-to-mass-ratios. If we assume that the proton and antiproton have identical charges, the cyclotron frequency ratio is the inverse mass ratio. Nevertheless, the measurement is actually a comparison of charge-to-mass-ratios.

There are many advantages of using this technique. A conventional FET preamplifier cooled to liquid helium temperature can detect a single particle with a good signal to noise ratio. An excellent resolution of 10^{-10} [19] has been mentioned while 10^{-8} can be routinely obtained. Based on this successful and extremely promising technique, an accuracy of 1 part in 10^9 for the comparison of the antiproton and proton masses was proposed [4,24]. This would be a 50 000-fold improvement in accuracy over previous measurements. Fig. 1.2 shows the fractional accuracy of antiproton mass measurements by exotic atom methods and by the ion trap technique. We have obtained a fractional accuracy of 4×10^{-8} in an ion trap [12,25]. This is already a 1000-fold improvement over previous measurements. The dashed region represents the proposed accuracy. This new measurement of the ratio of antiproton to proton inertial masses by the ion trap resonant method is the most precise test of the CPT theorem with baryons.

1.4 Antiproton lifetime in an ion trap and antiproton-atom (molecule) interaction

Interactions between antiprotons and atoms (or molecules) can be studied by controlled antiproton-atom collisions. The direct antiproton lifetime measurement in an ion trap can probe and indicate an extremely high vacuum beyond the capability of conventional vacuum measurement equipment. An upper limit to the pressure can be established with the knowledge of antiproton-atom cross section.

The measured lower limit of proton lifetime is now above 10^{25} years independent of decay mode [26], though for specific decay modes the lifetime now exceeds 3.1×10^{32} [27]. The CPT theorem thus suggests that the antiproton lifetime is no shorter than 10^{25} years. If baryon number is conserved then there can be no antiproton decay. The speculation that baryon number might not be conserved comes from grand unified theories which unify the strong force with the electroweak force [28,29]. If quarks can become leptons, then a proton (antiproton) might not be absolutely stable. A lower limit of 32 hours was given by a previous direct antiproton lifetime measurement in a storage ring [30], though measurements of specific decay channels yield a lifetime of more than one month [31]. Antiprotons were recently held 11 days at the CERN Antiproton Accumulator, with a particle loss rate corresponding to a storage lifetime of 1.4 months in the rest frame of the energetic antiprotons [32]. We found that the antiproton lifetime in an ion trap was more than 103 days (3.4 months) by trapping a cloud of antiprotons for 59 days (see Chapter 6). This is the best directly measured limit on the antiproton lifetime. The lifetime measurement in an ion trap can also be used for collision studies and vacuum technology development. As discussed in Chapter 6, we use stored antiprotons as a vacuum gauge to measure the residual gas number density and the pressure. The number density is measured to be less than 100 atoms/cm^3. For an ideal gas at 4.2 K, this would correspond to a pressure less than 5×10^{-17} Torr

which is the best reported value.

Finally, it has been suggested that measured $\overline{p}/p$ ratios in cosmic rays, together with model calculations of the interaction of cosmic rays and the interstellar medium, may indicate an antiproton lifetime of order the cosmic ray storage time ($\approx 10^7$ years). However, this rather indirect argument has not been studied in any detail, being mentioned in only one sentence [33]. Moreover, the cosmic ray storage time for antiprotons has not been measured to our knowledge.

1.5 Summary

In Chapter 2, the degrader technique used to slow antiprotons will be discussed. Studies include energy distributions of particles passing through a degrader measured by a time-of-flight technique, and the yield of low energy antiprotons at the keV level suited for trapping. It is followed by the observation of the Barkas effect in the range difference between protons and antiprotons. In Chapter 3, we describe the antiproton trapping experiment and discuss the results. In Chapter 4, the high-voltage switching required to capture of keV antiprotons in ion traps are described. Electron cooling as a means of slowing antiprotons until they fall into the harmonic potential well is discussed in Chapter 5. Two important applications of stored antiprotons are presented in the last two chapters. First is the antiproton lifetime measurement in an ion trap and its technical implications in Chapter 6. Second is the antiproton mass measurement at the 4×10^{-8} level in Chapter 7. Other experimental possibilities are discussed in the last chapter.

Chapter 2

Slowing antiprotons

Antiprotons are produced and then decelerated to 5.9 MeV energy at CERN. Slowing of antiprotons from LEAR energies of 5.9 or 21 MeV, down to keV energies is accomplished by sending the beam through a degrader which consists mainly of thin foils of mylar, Ti, Be, and Al. Various gases provide fine adjustment of thickness of the degrader. We prepared a simple time-of-flight spectrometer to study the range curve and the transmitted particle energy distribution. Particular interest is in the low energy particle yield since those particles can be trapped in an ion trap for further studies.

2.1 Production and deceleration of antiprotons at CERN

Antiprotons are generated at CERN by impinging 26 GeV protons on a heavy target [34,35]. Fig. 2.1 shows the facility for antiproton production at CERN. First, protons are obtained in the Pre-injector where electrons are stripped off from hydrogen atoms by ionization. Protons then are accelerated to 50 MeV in a linear accelerator (LINAC). In the next stage, the Booster increases the proton energy to 1 GeV. At the Proton Synchrotron (PS) ring proton energy reaches 26 GeV. A

high-intensity 26 GeV proton beam is sent to the antiproton production area and directed onto the target. Negative secondaries in a 6% momentum bite around 3.5 GeV/c (2.7 GeV) are selected and transferred to the Antiproton Collector (ACOL) ring. After bunch rotation and stochastic cooling, the antiproton beam is transferred into the Antiproton Accumulator (AA) and then stochastically cooled. In the stochastic cooling process, the longitudinal and transverse random motions of the antiproton beam are first detected. Then the signals are fed back to suppress the antiprotons momentum spread and transverse emittances. Typically a momentum spread $\Delta p/p$ of a few parts in 10^3 can be achieved by stochastic cooling [36].

The 26 GeV proton beam consists of five proton bunches, each containing 2×10^{12} protons. Every beam of five bunches hits the target in a burst of $0.5\mu s$ duration. This can be repeated every 2.4 s or in multiples of this period, mostly 4.8 sec. The bunch length in every beam is 20 ns and the time between bunches is 110 ns. The beam is focused at the target with small divergence of 2 mrad, and 95% of the beam hits a circular spot of 1 mm radius which is smaller than the target wire radius of 1.5 mm. The metal target being used at present is a 55 mm long iridium wire, which is along the direction of the beam, because of its high antiproton yield and high thermal conductivity for cooling. Other metals such as copper and tungsten were used before. The iridium wire is pressed into a graphite cylinder and sealed in a titanium alloy container cooled by water. The iridium wire and a 20 mm diameter lithium magnetic lens are in a very compact assembly. The lithium lens is used to focus antiprotons when a current pulse synchronized with the antiproton beam bunch flows through a cylinder of solid lithium. A magnetic field is created and the Lorentz force steers antiprotons back toward the beam axis.

The present antiproton production yield is 5×10^{-6} $\overline{p}/p$. This corresponds to a maximum production rate of 7.5×10^{10} $\overline{p}$/hr for a beam of 10^{13} protons every

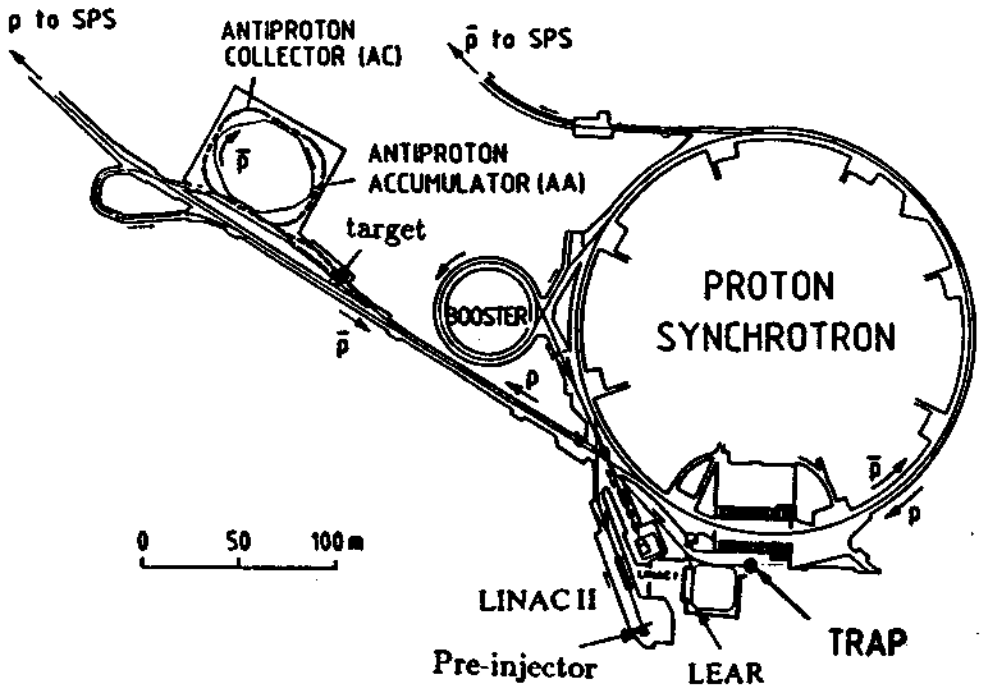

Figure 2.1: CERN facility for producing, transferring, storing and cooling antiprotons.

2.4 sec. Accumulation rates are about 30% to 50% of the production rates due to losses during the collection and stacking processes. Therefore the overall production and accumulation efficiency for 3.5 GeV/c antiprotons is about 2×10^{-6} $\overline{p}/p$ which is 3×10^{10} $\overline{p}$/hr.

Cooled antiprotons from the AA are decelerated in the PS from momentum of 3.5 GeV/c to 609 MeV/c (180 MeV). The decelerated antiprotons are transferred to the LEAR, the unique facility for providing large numbers of low energy antiprotons suitable for the trapping experiments. It is a square with side length of 20 meters. Typically 3×10^9 particles are transferred from the PS in each fill which takes up to 10 minutes including setup time. They are decelerated from 609 MeV/c to 309 MeV/c, then to 200 MeV/c, and finally to 105 MeV/c (5.9 MeV) within 20 minutes. The beam lifetime at 5.9 MeV is approximately one hour. Stochastic cooling is used again in the LEAR machine to reduce the energy spread and transverse emittances before and after each deceleration. The momentum spread $\Delta p/p$ is typically 10^{-3}. The well tuned beams of low energy antiprotons with energy as low as 5.9 MeV are extracted to the experimental area. The LEAR machine provides beams in two ways. Slow extraction is the normal mode of operation in which a slow and uniform spill of up to 10^9 particles is sent to experiments over approximately 1 h with rates from 10^3 to 10^5 Hz. Fast extraction is a special operation mode developed for the antiproton trapping experiment in which a 300 ns pulse containing up to 3×10^8 antiprotons is sent to our TRAP experiment.

The zone layout of our TRAP experiment (PS196) is shown in Fig. 2.2. The beam from LEAR in a horizontal beam line with a height of 1.6 m is bent by two dipole magnets (each one bending the beam 45^0 with a 0.3 Tesla field) into the vertical direction. A quadrupole focusing magnet is located between the two bending magnets. The last dipole magnet (Fig. 2.2) has a height of 3.1 m. The distance between its center and the center of our magnet is 1.7 m. The configuration of

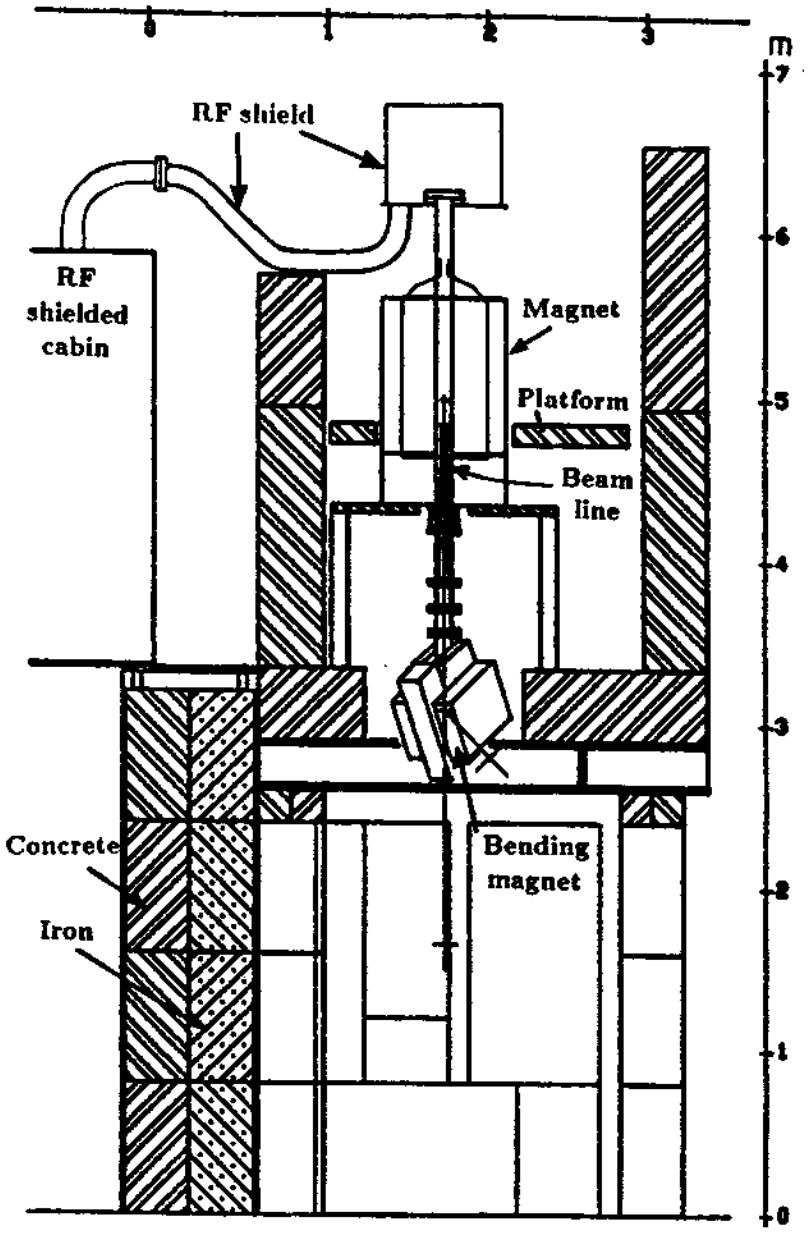

Figure 2.2: The zone layout of the TRAP experiment (PS196).

two 45^0 bending magnets allows focusing particles which differ slightly in energy to the same entrance to our apparatus. This feature is not possible for a single 90^0 magnet. Our extension of the LEAR beamline protrudes up into the bore of the superconducting solenoid and has an extremely thin Ti window just below the solenoid center (to minimize the multiple scattering effects, see Chapter 3). The Ti window separates the LEAR vacuum and 1 atm environment. Electronics for antiproton trapping studies are in a radio frequency (RF) shielded cabin, since there are strong RF noise sources in the experimental hall. There is an aluminum cap on the top of the magnet for RF shielding. Cables between the trap apparatus and the RF cabin (mostly double shielded cables) are within a flexible aluminum tube preventing external RF interference from leaking into our system.

2.2 The stopping and range of ions in matter

Energetic heavy charged particles (particle mass is much larger than electron mass m) in matter interact with atomic electrons and nuclei. The collisions with atomic electrons in matter constitute the main cause of energy loss by excitation and ionization of atoms or molecules, while nuclear scattering determines the spatial distribution of particle trajectories.

The average energy loss per unit path length is called the stopping power, S = −dE/dx, where E is the particle kinetic energy, and x is the absorber thickness. The stopping power [37] is the summation (and integration for ionized states) of each collision cross section σ_n times the corresponding energy transition E_n:

$$S = N\Sigma_n E_n \sigma_n \tag{2.1}$$

where N is the density of atoms in the target. For a heavy particle of charge Z and velocity v passing through a medium of atomic number Z_t, the stopping power S

is given as [38]:

$$S = -dE/dx = (4\pi e^4/mv^2)NZ_tZ^2L \tag{2.2}$$

where m is the electron rest mass, NZ_t is the electron density n_e in the matter, and L is a function of the particle velocity and stopping material. Using the Bethe stopping function, we have [38]

$$L = L_0(v, Z_t) = \ln(2mv^2/I) - \ln(1 - v^2/c^2) - v^2/c^2 - C/Z_t. \tag{2.3}$$

Here, I is the target mean-excitation and ionization potential (it is 166 eV for Al), and C/Z_t is the shell correction. The stopping power for heavy charged particles depends largely on the velocity and the charge of the particle, but not on its mass. For proton energies above 100 keV the smaller the velocity, the larger dE/dx is. Therefore more energy loss per unit length will happen near the final stage of slowing.

A theoretical range is obtained by integrating the inverse stopping power over the total energy loss [37]. A parallel monoenergetic beam of heavy charged particles in matter has a relatively well defined range, which is essentially the thickness of the absorber stopping practically all the particles. (The energy loss is not like the exponential absorption for the electromagnetic radiation.) In Fig. 2.3(a), a range curve shows the fraction of particles in a beam penetrating to a given depth x. Initially the beam loses energy in matter without changing the number of the particles in the beam. All the particles go a long way together. When the thickness of the absorber is very close to the range, the number of particles starts to decrease rapidly. The mean range R_0 is the thickness of the absorber allowing 50% of the particles to pass. Particles do not stop sharply at R_0 because of the statistical nature of the energy loss process. Random interactions produce fluctuations in energy loss or in range. Straggling is just the fluctuation in energy loss or the particle penetration depth (range). For a given energy loss, each particle stops near the average value R_0 with its own range R. For particles with a mean value

R_0, the probability of finding a particle with range between R and R+dR is [37]:

$$f(R)dR \approx (1/\sigma\sqrt{2\pi})exp[-(R-R_0)^2/2\sigma^2]dR. \quad (2.4)$$

Here, the distribution function f(R) of ranges around the average R_0 is approximated by an Gaussian, and the mean-square fluctuation σ^2 is defined by:

$$\sigma^2 = < R^2 > - R_0^2. \quad (2.5)$$

In this approximation, the largest number of low energy particles can be found at R_0. The relative Gaussian distribution function:

$$f_1 = exp[-(R-R_0)^2/2\sigma^2] \quad (2.6)$$

is plotted in Fig. 2.3(b). It has a FWHM of 2.35 σ and $f_1 = 61\%$ when $|R-R_0| = \sigma$. The range straggling parameter σ/R for protons of kinetic energy E in some elements can be found in Ref.[37]. For example, σ/R is 1.38% for Be and 1.56 % for Al at beam energy of 5.9 MeV. At 21 MeV (where we did initial demonstration experiments) the numbers are 1.25% (Be) and 1.37% (Al).

When a heavy particle collides elastically with a target nucleus, the Coulomb force from the nucleus deflects it by Rutherford scattering. The angular distribution of the transmitted particles passing through a thin foil is mainly determined by nuclear multiple scattering. A cumulative effect of many nuclear scatterings will make a significant deviation from the original direction of a particle. The collisions with electrons produce only a small angular scattering of heavy particles. The importance of multiple scattering from nuclei for particle trapping is discussed in Section 3.5.

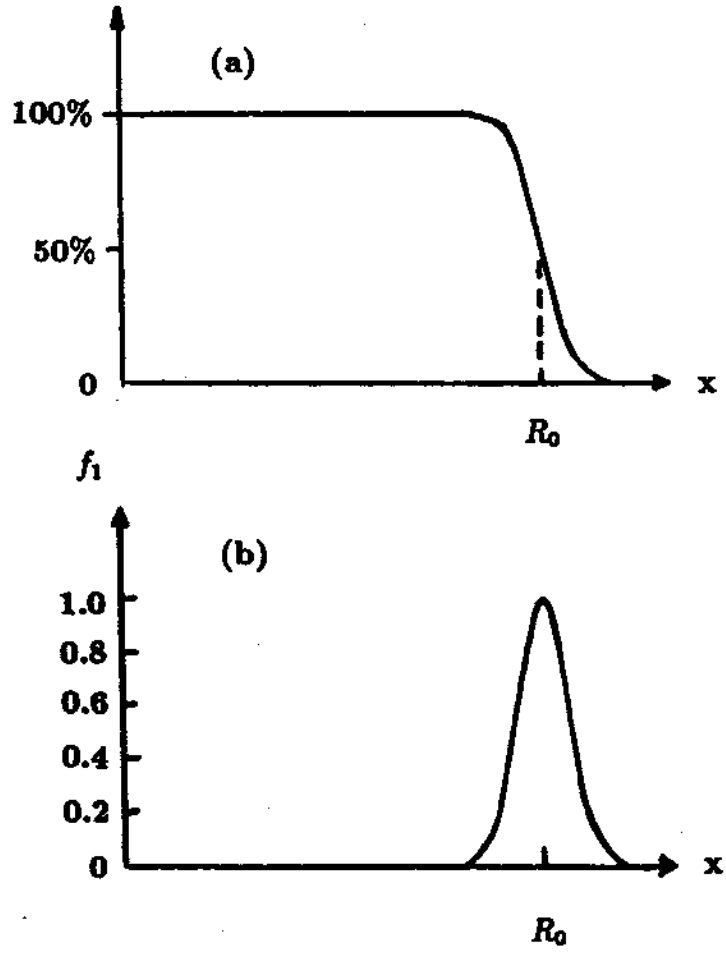

Figure 2.3: (a) An idealized range curve showing the fraction of particles in a beam penetrating to a given depth x. The mean range R_0 is the point passed by half the particles. (b) The relative distribution of particles near mean range.

2.3 Experimental setup for slowing protons and antiprotons in matter

The main purpose of the experiment is to obtain as many low energy antiprotons as possible. It is necessary to adjust the degrader thickness to just "range out" particles at the beam energy. Slow extraction is the normal mode of operation at LEAR in which a slow and uniform spill of up to 10^9 particles is sent to experiments over approximately 1 h with rates available from 10^3 to 10^5 Hz. Experimental methods of range measurements are discussed in Ref. [39]. A simple way to perform the experiment is by the transmission method. The basic idea of the transmission method for range curve and energy distribution measurements is illustrated in Fig. 2.4. A particle in the incident beam first goes through a Start detector, the parallel plate avalanche counter (PPAC), which provides a start signal and itself is also a part of the degrader. The particle then moves into a stack of thin foils and gases. If the particle passes through all the degrading material it can be counted by the microchannel plate detector (MCP) [40] which we used at both 300 and 77 K, to provide a stop signal from the transmitted particle. The time-of-flight Δt of the particle in passing from the degrader to the back detector over a distance L is recorded. If the degrader material is unchanged, a time-of-flight distribution can be obtained when a large number of particles are detected. From the flight time $\Delta t = L\sqrt{m_p/2E}$, we obtain the energy distribution of the transmitted particles and the low energy particle yield. The range curve can be traced out by changing the thickness of degrader and plotting the transmitted ion fraction, given by the ratio S_{stop}/S_{start} of the Stop detector counting rate and the Start detector counting rate, versus the thickness of the degrader.

A simplified logic diagram for the detection electronics is given in Fig. 2.4. It shows that signals from detectors are amplified, and then shaped by constant fraction discriminators before being sent to counters. Scalers count the signals from

both detectors. A qVt multichannel analyzer (LeCroy 3001) operating in the time analysis mode records the time delay between start and stop signals, as does a time-amplitude-convertor (TAC) plus an analog-digital-convertor (ADC). A microcomputer collects and stores the data, and displays the time spectrum.

The Stop detector subtends a finite solid angle to the center of the last surface. The half-angle in the side view plane θ_0 is 21^0 in this experiment, because the distance L is 2.54 cm and the MCP detector has an active diameter of 2 cm. Transmitted particles deflected away from beam axis by multiple scattering with $\theta < \theta_0$ will be counted.

2.3.1 The variable degrader for energy tuning

For incident 21 MeV antiprotons, we rotated thin degraders in and out of the beam [8]. This was not possible for 5.9 MeV antiprotons because the degraders must be 10 times thinner (0.25 mm Al). These degraders must also be located within the bore bore of the superconducting solenoid (See Fig. 3.3) to avoid large loss from multiple scattering. We use **dE/dx gas cells** to fine tune the degrader thickness for a given beam energy thus yield maximum number of low energy antiprotons for trapping. The apparatus used for proton and antiproton tests at about 6 MeV is as follows. High energy particles extracted from the machine through a thin titanium window enter from below at a rate of 1 to 10 kHz. To vary the energy loss of the particles by a small amount, we use two gas cells indicated in Fig. 2.5. Either SF_6 or N_2 at a pressure of 1 atm is kept flowing slowly through gas cell 1. The energy loss in the N_2 is smaller than the energy loss in the SF_6 by approximately 250 keV so the energy of the protons and antiprotons leaving gas cell 1 can be changed discontinuously by this amount. A mixture of SF_6 and He, also at 1 atm, is sent through gas cell 2. The mix can be adjusted continuously

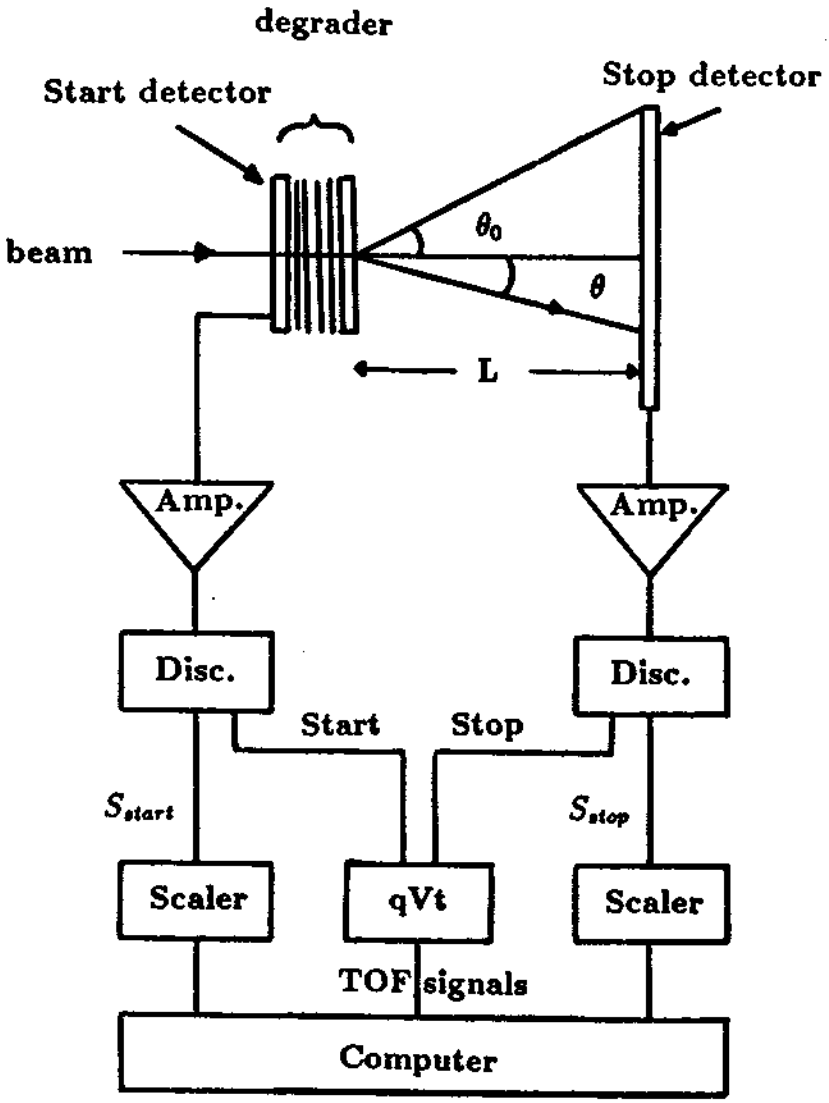

Figure 2.4: Transmission method for range curve and energy distribution measurements.

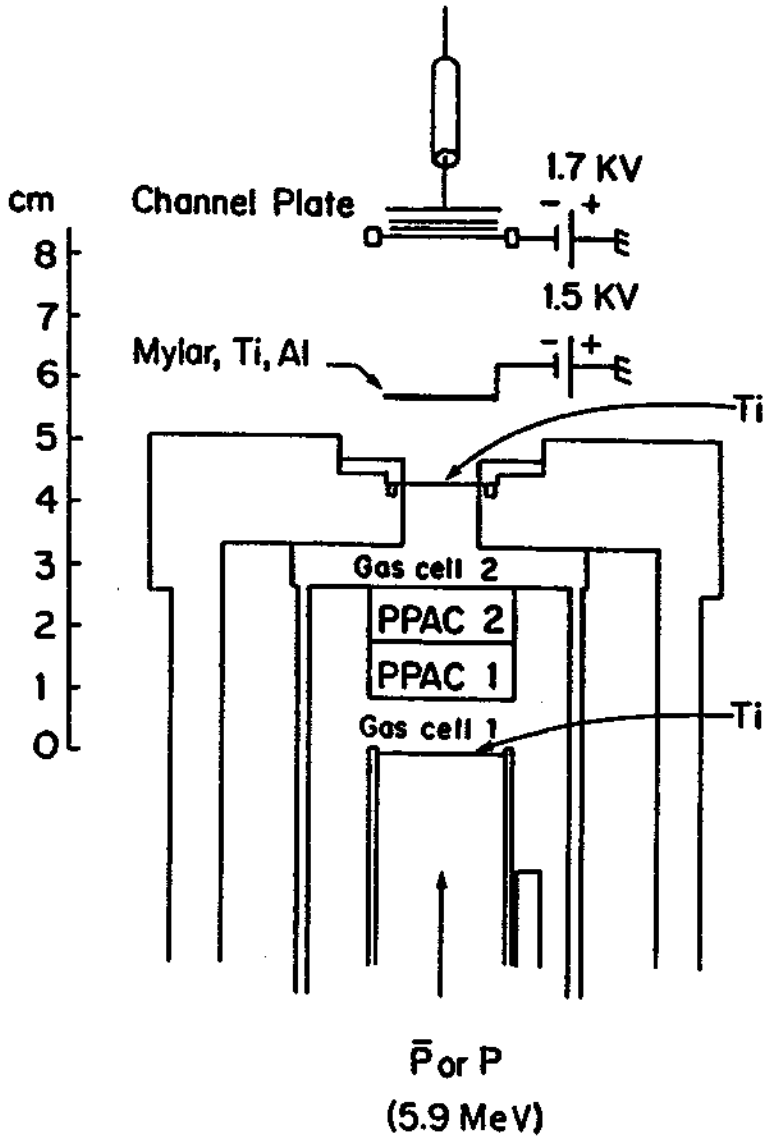

Figure 2.5: Time-of-flight apparatus. The apparatus from below 5 cm on the vertical scale remained in place for trapping experiments so that the incident antiprotons could be monitored and their energy tuned slightly. PPAC is the parallel plate avalanche counter.

with electronically controlled flow meters, allowing the energy of the antiprotons leaving gas cell 2 to be continuously adjustable over an additional 500 keV when the number of molecules in the mixture is changed from 0% SF_6 (i.e., 100% He) to 100% SF_6 (i.e., 0% He). These energy shifts were calibrated using the variable energy proton beam of the tandem accelerator of the Nuclear Physics Laboratory at the University of Washington, in Seattle, to produce range curves such as those in Fig. 2.9 which are discussed later. The energy loss was linear in the percentage of SF_6.

Helium and SF_6 flow in gas cell 2 are controlled by an OMEGA electronics package (FMA-2DV) with dual channel and setpoint potentiometers, and two OMEGA electronic mass flow controllers (FMA-116). The mass flow can be read and set for flow measurement and control by the package FMA-2DV unit. It can power and operate 2 independent flow controllers simultaneously. The display for reading flow value is linear with a $0-100\%$ full scale. The display shows the flow value when in the READ mode and the set point when in the SET mode. The mass flow controllers FMA-116 directly monitor the flow of gas molecules. This flow meter uses a heated sensing element and thermodynamic heat conduction principles to determine the true mass flow rate with 1% accuracy and 0.2% repeatability. The response time is 1 second. The mass flow controllers are factory calibrated for nitrogen (N_2). Nitrogen flow range is from 0 to 1 litre/min. The actual flow rate for any gas is equal to the flow rate of nitrogen unit times the correction factor. The correction factors for various gases are available from OMEGA Engineering Department. It is 1.45 for helium and 0.27 for SF_6. That is, when the flow display is 100%, the actual flows for He and SF_6 are 1.45 l/min and 0.27 l/min, respectively. In our system we use $SF_6\%$ as the percentage of molecules (or reference fraction) in the gas cell 2. The total flow is kept at 0.27 l/min. The corresponding helium setting (to keep the total flow constant) can be calculated as:

$$He(READ/SET) = 18.6 \times (100\% - SF_6\%). \tag{2.7}$$

For example, we need to set SF_6 at 10 and He at 16.7 to have 10% SF_6 and 90% He in gas cell 2. If we need 90% SF_6 and 10% He, then the setting should be 90 for SF_6 and 1.86 for He.

A simple **time-of-flight apparatus** (see Fig. 2.5) is used for proton and antiproton tests. A beam of 5.9 MeV particles extracted from LEAR through a thin (10 μm) titanium window, enter this apparatus from below at a rate of 1 to 10 kHz. Gas cells 1 and 2 permit particle energy tuning. Two PPACs located between the two gas cells determine when a proton or antiproton enters the apparatus with near unit efficiency and nanosecond resolution. Typically, the beam is focused into a spot diameter of less than 6 mm (full width half maximum) on the PPACs. The antiprotons slow in several layers of material needed for the trapping experiments being prepared. Each layer is listed in order in Table 2.1, along with the equivalent thickness of aluminum (to allow easy comparisons) and the approximate energy loss [41] in each layer. As shown in Table 2.1, most of the slowing, nearly 4 MeV, occurs in the final aluminum layer. The aluminum foil has mirror surfaces with very little surface roughness. The antiprotons stop and are detected with near unit efficiency in the channel plate detector located 2.5 cm down beam. The final degrader window and the channel plate are biased as indicated to minimize the probability of detecting a secondary electron liberated from the aluminum. The number of coincidences of the PPAC detectors with the channel plate are divided by the number of PPAC counts to give a measure of the fraction of the incident particles transmitted through the degrader. This gives the range curve when the number versus the equivalent thickness of the aluminum degrader is plotted. It will be discussed in connection with the Barkas effect below. Time-of-flight spectra of the transmitted protons and antiprotons are also recorded, making it possible to study the energy spectra of the transmitted protons and antiprotons.

Material	Equivalent thickness of Al (μm)		Energy loss (MeV)	
10-μm-thick Ti	16		0.21	
Gas cell 1 with N_2	4.4		0.06	
with SF_6		23		0.31
PPAC 1	11		0.16	
PPAC 2	11		0.16	
Gas cell 2 with He	1.4		0.02	
with SF_6		34		0.52
10-μm-thick Ti	16		0.24	
51-μm-thick Mylar	31		0.52	
10-μm-thick Ti	16		0.27	
117-μm-thick Al	117		3.70	
Total	224	275	5.34	6.09

Table 2.1: Matter traversed by protons and antiprotons.

2.3.2 The detection system

A chevron-pair **microchannel plate detector** with an active diameter of 20 mm (Varian 8960ZS) is used as the stop detector. It is used at 300 K (and with higher gain at 77 K). The gain for each plate is approximately 10^4 at about 850V bias potential. For the MCP pair at bias potential of 1700V, the total maximum gain is 10^8. The efficiency of the MCP is about 65% for fast particles measured by the transmission method (the coincidence signals of PPAC and CP divided by PPAC signals). The detection efficiency should be around 60 to 85% (see Ref. [40]) for low energy particles (2 to 50 keV). We use one as the detection efficiency for conservative number counting which allows a lower limit of the particle yield. Signals detected by MCP are denoted CP.

A beam diagnostic system of two **parallel plate avalanche counters** (PPAC) with position sensitivity was developed [42] as the Start detector for diagnostics of the incoming beam intensity and position (focusing). It meets the requirements for thickness (only 10% of the total Al degrader equivalent), time resolution (<0.5 ns), beam profile resolution (2.5 mm in both X and Y directions), and works well in the environment of the 6 T magnetic field.

PPACs are usually used in heavy ion detection for precise timing measurements in nuclear physics [43]. This type of gas counter with large active area is more useful when combined with position sensitive counters to have both timing and position information. The problem with light ion detection is that the specific ionization is much smaller as is the signal. However at an energy of a few MeV, ionization in the gas is high enough even for light particles due to the velocity dependency of dE/dx that a detection efficiency of nearly unity is achievable.

Each PPAC consists of two parallel aluminized mylar foils as electrodes, sepa-

rated by a narrow gap L to achieve good time resolution. The gap is normally filled with isobutane gas (C_4H_{10}). An energetic particle moves through the counter perpendicular to the foils, and electron-ion pairs are produced in the gas. When the high voltage V applied across the electrodes is sufficiently large, the homogeneous strong electric field V/L makes secondary ionization and an avalanche is formed. The number of secondary electrons produced by one primary electron is given by $e^{\alpha l}$, where l is the distance from primary electron initial location to the anode, the drift length. The α is the first Towsend coefficient, the mean ionization probability per unit path length and is a function of the reduced field strength V/Lp, here p is the gas pressure:

$$\alpha/p = A\ exp[-B/(V/Lp)]. \tag{2.8}$$

A and B are constants for the specific gas. In our system, the reduced field strength is 120 V/cm/torr for V = 900 Volts, L = 1.25 mm, and p = 60 Torr. Primary electrons produced near the cathode have the longest drift length L and hence the largest gain $e^{\alpha L}$. They contribute most to the signal. We denote the total number of primary electrons as N_0, and assume they are produced uniformly from l = 0 to L. Then the total number of secondary electrons within the gap generated by a single energetic proton or antiproton is:

$$G = \int_0^L (N_0/L)e^{\alpha l}dl = N_0(e^{\alpha L} - 1)/\alpha L. \tag{2.9}$$

Since $e^{\alpha L} >> 1$, the effective gain of the PPAC is:

$$G = N_0 e^{\alpha L}/\alpha L. \tag{2.10}$$

In our case, a 5.9 MeV proton or antiproton makes about 100 primary electrons, the effective gain G is about 10^6 for αL = 12. The resulting signal has an amplitude of about a 5 mV on a 50 Ω impedance with a 2 ns width and a very fast rise time due to the motion of electrons. Positive ions are collected over about 1μs and are too weak to see. With further amplification ($\times$ 100), a 500 mV signal can be observed by a 350 MHz scope and is fed into a discriminator for processing.

In each PPAC, the anode mylar is stretched and epoxied to a PC board disk. The cathode is stretched over a lucite boss contour to minimize breakdown at the edge of the active region and epoxied to another PC board disk. The active area has a diameter of 1.8 cm. Two PPACs with their gas lines and RG174/U coaxial cables are mounted in a 5 cm diameter by 3.5 cm long lucite assembly. Two 9 μm thick mylar vacuum windows supported by 125 μm thick 90% transparent molybdenum grids seal the detector assembly at both ends from the 1 atm ambient. The isobutane gas flow rate can be controlled up to 100 atm-cc/min. In Fig. 2.6(a), the two anodes are each etched into five parallel segments. Each of the 3 at the center is 2.5 mm wide. The position resolution of 2.5 mm is achieved in both X and Y directions when the first PPAC segments (X) are perpendicular to the second (Y). The PPAC detectors and their electronics are shown in Fig. 2.6(b). The ten segments (5X, 5Y) are brought to two stages of Phillips 776 amplifiers (each has a gain of 10) and discriminators. For continuous beam flux ($10^3 - 10^4$ particles/sec) the discriminator signals are sent to a 10-channel rate meter with 0.1 sec integration time constant. The 0 to 10 V analog output for each channel is fed into an LED display for X and Y beam profile histograms.

The electronics and logic circuits are shown in Fig. 2.4 and Fig. 2.6. Similar to the PPAC signal, the microchannel plate signal CP is amplified by a factor of 100 and shaped by a discriminator. The NIM pulses of the PPAC (x1, x2, x3, x4, x5, and y1, y2, y3, y4, y5) and CP are sent to scalers, and a logic unit (AND/OR logic). The important logic signals obtained are the start signal,

$$S_{start} = PPACX \bigcap PPACY, \tag{2.11}$$

and the stop signal,

$$S_{stop} = CP \bigcap PPACX \bigcap PPACY = CP \bigcap S_{start}, \tag{2.12}$$

where PPACX = $x2 \bigcap x3 \bigcap x4$, and PPACY = $y2 \bigcap y3 \bigcap y4$. As discussed earlier, S_{stop}/S_{start} determines the range curve, and relative timing of S_{stop}, S_{start} gives the

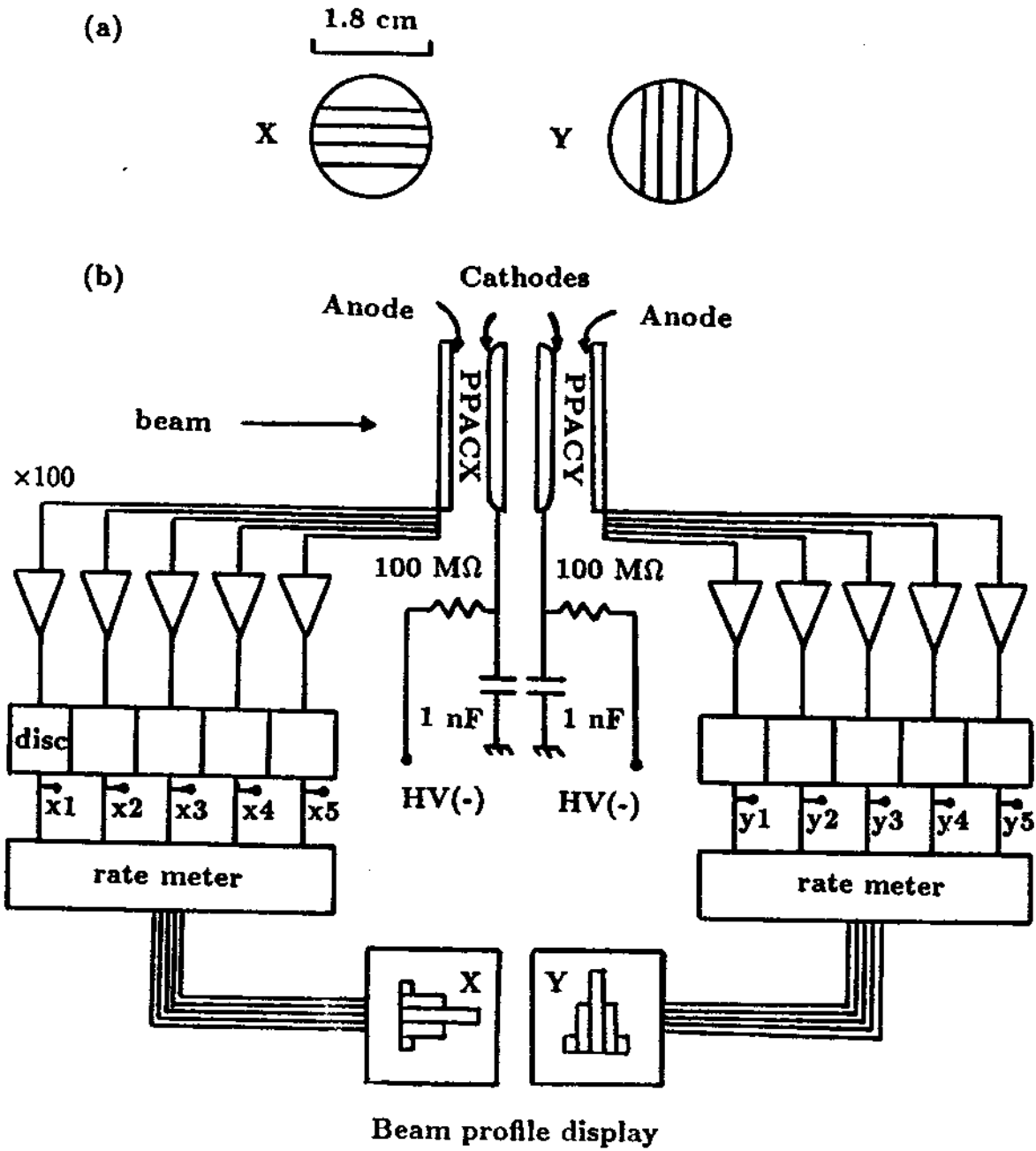

Figure 2.6: (a) The anodes of PPACX and PPACY. (b) PPAC detectors and their electronics.

energy distribution information.

2.4 Low energy antiproton yield and energy distribution of transmitted particles

A preliminary degrader test was carried out for 21.3 MeV antiprotons passing through Be [8]. The number of antiprotons which emerge from the degrader with low kinetic energy (along the beam axis), between 2 and 8 keV, is peaked at about the half intensity point in the range curve for antiprotons of all energies. Approximately 1 in 10^4 of the incident antiprotons emerges from the degrader with energy below 3 keV. The reason for using a 5.9 MeV beam instead of 21 MeV antiprotons is that a higher yield of low energy antiprotons is expected. The straggling parameter σ/R is essentially unchanged, but the range drops by nearly an order of magnitude when the energy is reduced from 21 MeV to 6 MeV. The distribution width (FWHM) ΔR therefore is reduced by an order of magnitude. Particles will stop in a much narrower slice of degrader. For example, the range in Be for 21 MeV beam is 3.0 mm with $\Delta R = 0.088$ mm while the range in Al for the 5.9 MeV beam is 0.25 mm with $\Delta R = 0.0093$ mm. The distribution is narrower by a factor of 9.5. Under ideal circumstances, we might thus expect 9.5 times more low energy antiprotons.

Fig. 2.7 shows the energy distribution of 5.9 MeV antiprotons after they pass through a degrader adjusted to give maximum low energy antiproton yield when the percentage of SF_6 in the gas cell is 60%. There are 5.1×10^5 Start signals and 10^5 Stop signals counted by scalers for this run. The normalized transmitted fraction is about 40%. The channel numbers (thus the flight time), kinetic energies, and the counts are indicated. Each channel represents 0.1 ns. The small bumps

before the TOF peak may be due to the antiproton annihilation secondary or the PPAC ringing that triggered the start counter. Because the gates of our discriminators were set at 60 ns, the signals from ringing reflect the TOF events after the 60 ns flight time. However, they do not affect the information we need, which is the spectrum within 60 ns and after the main TOF peak. The solid line is for a constant energy distribution of 100 counts/keV. The line fits the data well at the energy below 500 keV indicating that the particle energy distribution is fairly flat, and it falls when energy is near and above 500 keV. The average antiproton yield below 500 keV is approximately 2×10^{-4}/keV. Antiprotons between 20 ns and 40 ns correspond to the kinetic energies of 8 keV down to 2 keV. Changing the percentage of the SF_6 gas in gas cell 2 gives the antiproton yield between 2 to 8 keV versus the effective degrader thickness, as is plotted in Fig. 2.8. The peak yield is $1.6(0.1) \times 10^{-4}$/keV (which is a lower limit since we used 1 as the detection efficiency) when SF_6 in gas cell 2 is 60%, which is very close to the degrader setting of the half intensity point for antiprotons of all energies (see Fig. 2.9). It is approximately a factor of 8 increase compared with the previous test of 21.3 MeV beam traversing Be target ($2.1(0.1) \times 10^{-5}/keV$, also a lower limit). The surface roughness could make things worse. Only 1.7 μm broadening is needed to decrease the yield by 17%. There are about 20 surfaces in the degrader foils. If each surface contributes 0.4 μm in average (which is possible in our experiment), then it could make such difference. We observed this effect as many fewer antiprotons were trapped when very rough degrader surfaces were used.

Even though the proton data we have is only 10% of antiproton data, we can still qualitatively say that the energy distribution of protons emerging from the degrader is similar to the one for antiprotons. The low energy proton yield is $2.0(0.2) \times 10^{-4}$/keV which is consistent with the antiproton yield.

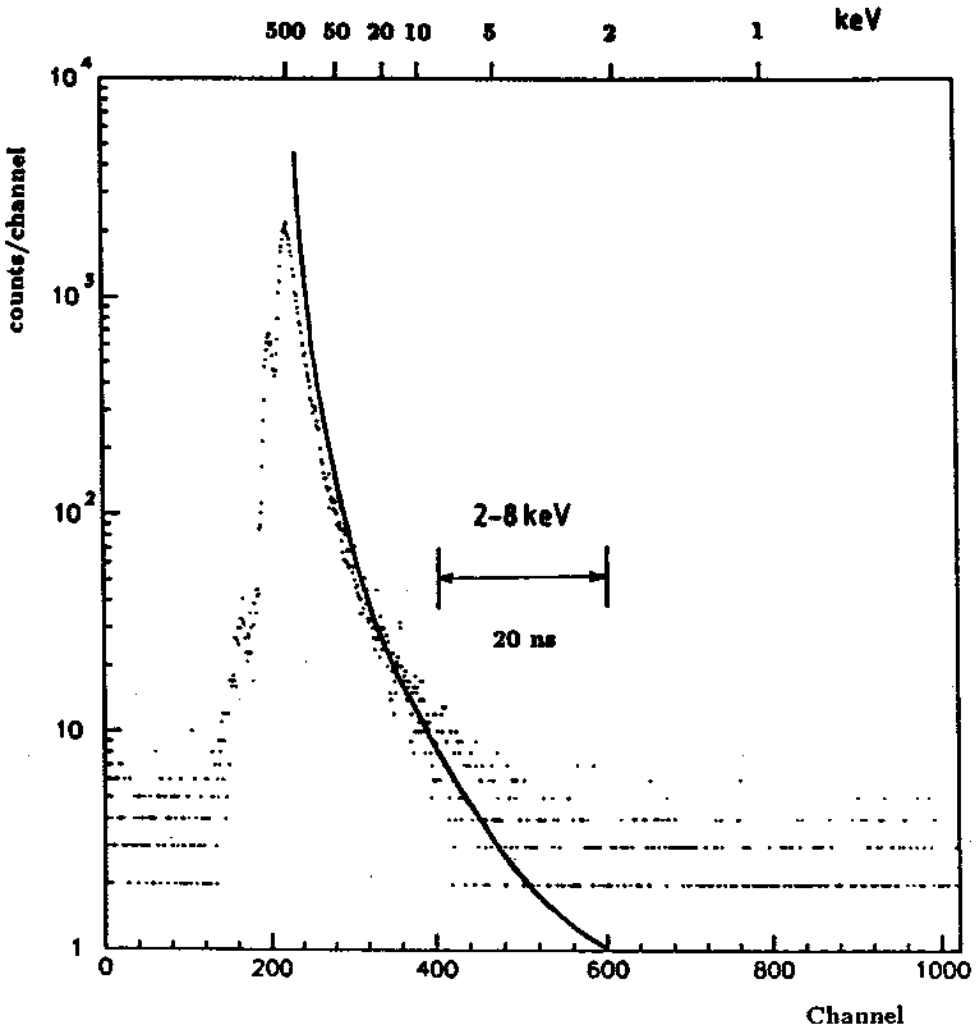

Figure 2.7: Energy distribution of exit antiprotons through degrader with maximum low energy particle yield.

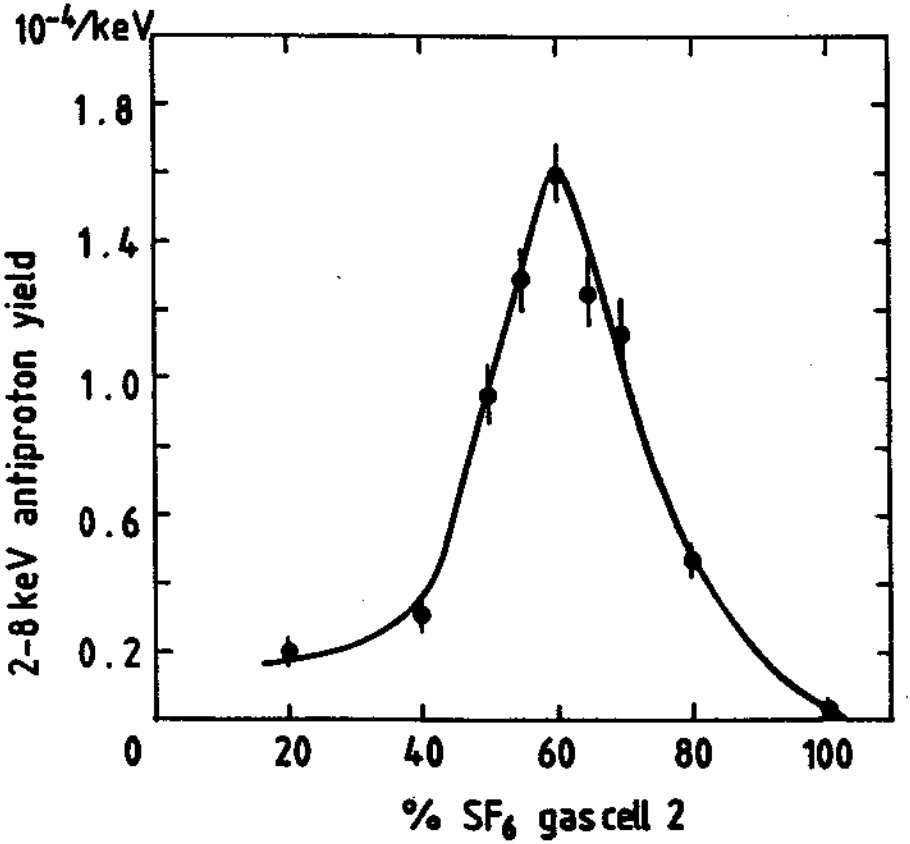

Figure 2.8: 2 to 8 keV antiproton yield versus the effective degrader thickness for 5.9 MeV antiprotons in the apparatus shown in Figs. 2.4 and 2.5.

2.5 Observation of the Barkas effect with protons and antiprotons

Energy-loss and range measurements carried out to improve our understanding of charged heavy particle penetration of matter appear to be of great interest for basic and applied physics. Barkas and his collaborators [44] first observed the striking difference of the energy loss processes in emulsion track studies for π^+ and π^-, and also for Σ^+ and Σ^-. The difference in the range of heavy particles of opposite charge under otherwise identical conditions is known as the Barkas effect. This charge-sign-dependent effect comes from distortions of the target electron motion or wave function during the atomic collision, so it is also referred as the polarization effect. For a heavy particle of charge Z and velocity v passing through a medium of atomic number Z_t, the stopping power S may be written as

$$S = -dE/dx = (4\pi e^4/mv^2)NZ_tZ^2(L_0 + L_1Z + L_2Z^2) \qquad (2.13)$$

where N is the atom number density of the stopping element, m is the electron rest mass, and L_0, L_1 L_2 are functions of the particle velocity and stopping material. Here, higher-order terms in Z are included unlike the Equation (2.3). The existence of a Z^3 term with a positive coefficient L_1 implies a greater range for a negative particle than for a positive one under conditions of equal mass and equal initial velocity. With protons and antiprotons of the same energy, observed differences in the stopping power and range arise only from L_1 (higher-order terms odd in Z are neglected here). The effect of the terms of even order in Z cancel.

Observations of the Barkas effect using positive and negative muons have been reported [45,46]. Higher order terms in the stopping power have been accurately measured for positive ions of H, He and Li [47]. There are many other ion experiments and the available experimental data indicates a positive coefficient L_1. Theoretical investigation of Z^3 correction was made first by Ashly, Ritchie and

Brandt [48](ARB theory) and later Jackson and McCarthy [49] and by Lindhard [50] in classical calculations. Though in general they agree well with experiments qualitatively, current analytical results differ by approximately a factor of 2, and there are even larger discrepancies arising from numerical calculations.

The range curve data obtained verified the existence of the Barkas effect for the proton-antiproton system [10]. The points in Fig. 2.9 represent two measurements of the number of transmitted projectiles versus the effective thickness of the degrader. The left curve is for protons, the right curve is for antiprotons. The vertical scale is proportional to the coincidence signal divided by the number of incident projectiles, as described earlier. A small and flat pion background of $\approx$ 10% (from annihilation pions striking the channel plate) was subtracted off in the case of the antiprotons. The horizontal scale indicates the fraction of SF_6 in gas cell 2 with either N_2 in the first gas cell (tick marks above the axis) or with SF_6 in the first gas cell (tick marks below the axis). The horizontal scale thus essentially represents the thickness of the degrader. Increasing the aluminum thickness by 51 μm would cover the same range covered by this scale. Alternatively, the horizontal scale represents the relative scale corresponding to a shift of approximately 750 keV in the incident energy. The shift of the proton range curve as a function of incident proton energy was used to calibrate the gas cells.

The error bars on the measured points in Fig. 2.9 represent the largest variations observed in the measured points over several hours. These variations were observed to be correlated with beam intensity, beam steering, etc. The size of the points themselves represent the short-term repeatability over several minutes. The proton and antiproton curves have a similar shape, as illustrated by the identical smooth curves sketched through the measured points, but the antiproton curve is shifted by 150$\pm$20 keV. Several corrections and additional uncertainties must be included. The LEAR staff measured the difference in beam energy between

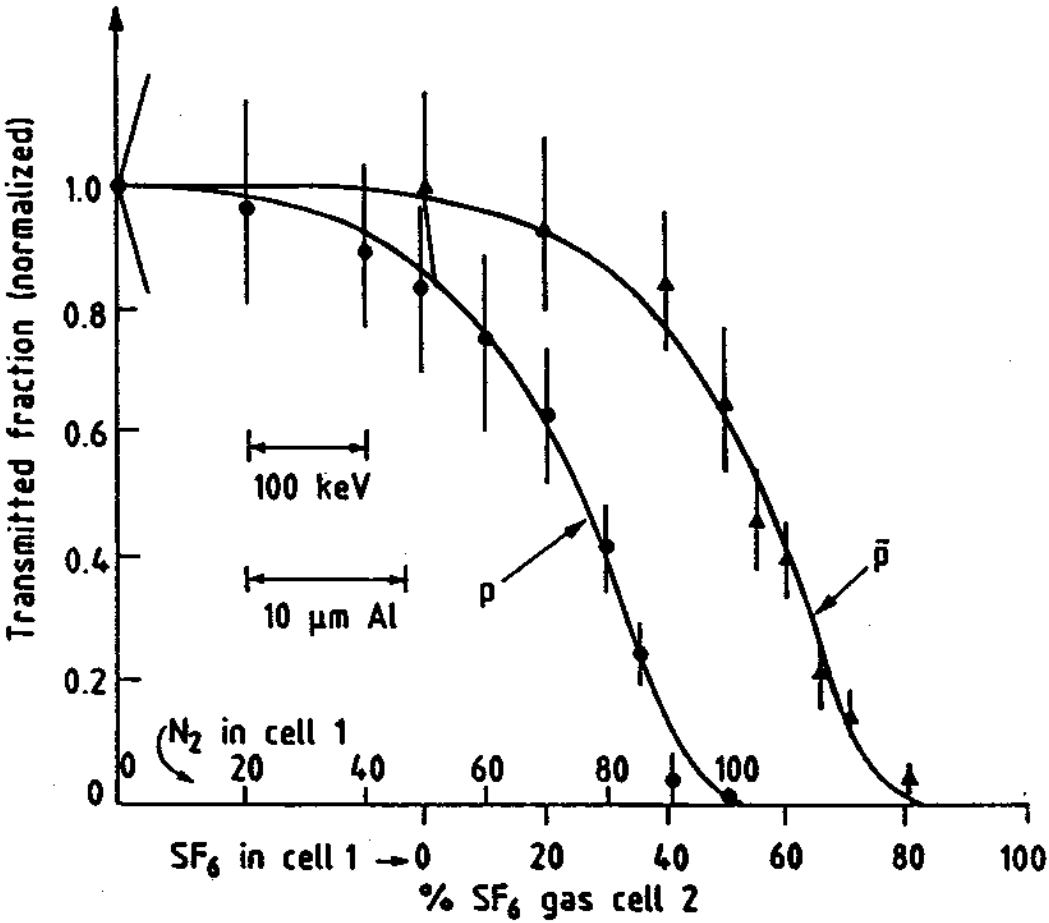

Figure 2.9: Normalized fraction of antiprotons detected after the degrader showing the difference in energy loss and range of protons (left) compared to antiprotons (right).

protons and antiprotons extracted from LEAR to be 13±12 keV. Temperature differences in the degraders between the proton and antiproton measurements contribute 31±12 keV. Uncertainties in the calibrations of the first and second gas cell contribute ±30 keV and ±20 keV, respectively. The net result is that the energy lost by 5.9 MeV protons is greater by

$$\Delta E = 194 \pm 45 \; keV \tag{2.14}$$

than the energy lost by 5.9 MeV antiprotons. The aluminum equivalent for this energy difference is $\Delta R = 14\mu$m and

$$\Delta R/R = 5.6 \pm 1.4\% \tag{2.15}$$

is the equivalent fractional range difference in aluminum, the range being larger for antiprotons.

To quote the above range difference for aluminum and to compare with theoretical values, we initially model the degrader as a piece of aluminum approximately 250-μm thick. This is the sum of the equivalent Al thicknesses from Table I. The formula given by the theory of Ashley, Ritchie, and Brandt (ABR) [48] gives a fractional range difference of 3.2%, which is somewhat lower than our measured value. However, Lindhard included the contributions from close collisions which are absent in ARB theory and estimated that the Barkas effect was approximately twice that of ARB theory [50]. To accommodate this effect, Ritchie and Brandt [51] adjusted their original choice of cutoff at small impact parameters to make the L_1 larger. Both the Lindhard theory and the adjusted ARB theory seem to agree with our measurement, though more precise theoretical predictions are clearly needed. To check the simplifying model above, we use the Lindhard theory to estimate that modeling the matter traversed by the beam as a single piece of aluminum could cause an error as large as ±20 keV, somewhat smaller than the uncertainty from other sources. Thus we can consider ΔE given earlier to be the measured

energy loss in Al, provided the quoted uncertainty is increased to ±50 keV. The reason that the Barkas effect occurs primarily in the aluminum is that until they enter the final aluminum degrader at approximately 4 MeV, both the antiprotons and the protons travel rapidly enough so that contributions to the Barkas effect are small.

In summary, the Barkas effect of about 6% difference in range is detected when 5.9 MeV protons and antiprotons are sent through the same aluminum degrader [10]. Another measurement of the Z^3 contribution to the stopping power using protons and antiprotons in silicon is reported in Ref. [52].

Chapter 3

Trapping antiprotons in an ion trap

A small number of keV protons (Fig. 3.1) and antiprotons (Fig. 3.2) were briefly trapped during feasibility tests [7,9]. With improved apparatus and technique (5.9 MeV LEAR beam instead of 21 MeV, vacuum improvement, energy ramp technique to avoid saturation in detection system), and more beam time to check the system routinely, we are able to trap antiprotons 100 times more efficiently and hold them indefinitely.

A simple diagram of the ion trap which consists a load endcap (the left cylinder), a ring (the central cylinder) and a dump endcap (the right cylinder) is shown in Fig. 3.1(a). Antiprotons approach from the left along the magnet field direction and are captured. They leave the trap toward the right and are detected. In a new mode of operation, the beam from LEAR is extracted in fast extraction which delivers a 300 ns pulse of antiprotons containing up to 3×10^8 particles. Because 3 keV particles transit the trap in less than 0.5 μs, only one particle would be present in the trap in slow extraction even if the beam is continuous with a rate of 2000 kHz. The fast extraction allows many more particles within the trap during the short pulse so that they can be trapped efficiently.

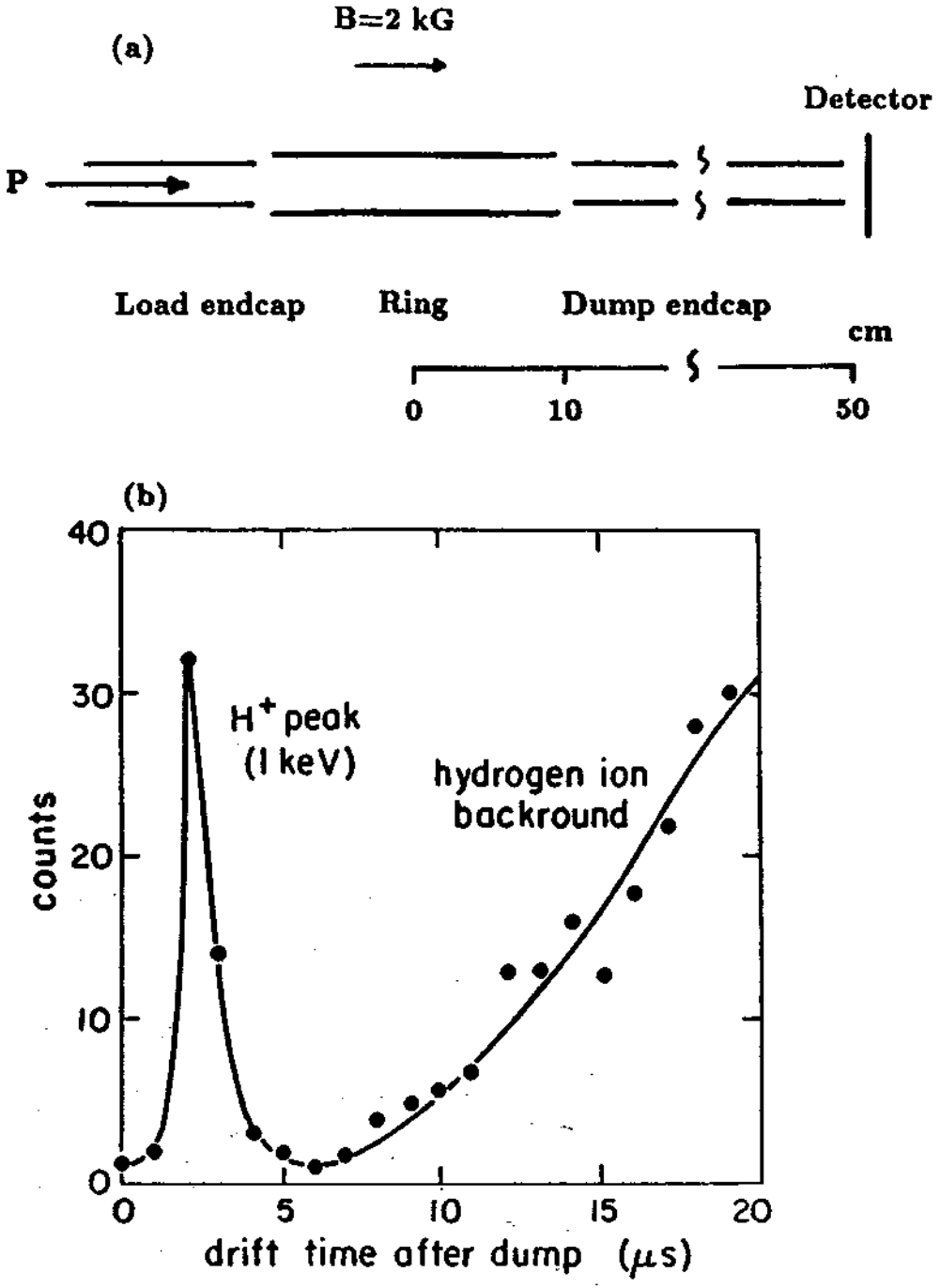

Figure 3.1: First direct trapping of keV protons.(a) Ion trap. (b) Particle counts.

We rely on the magnetic field to provide radial confinement. A 6 Tesla magnetic field is used to confine antiprotons radially when their radial energy $E_r = mv_r^2/2$ is not too large. From the formula $mv_r^2/r_c = ev_rB$, we have the radius of the cyclotron motion $r_c = mv_r/eB$, or,

$$r_c = (\sqrt{2mE_r})/eB. \tag{3.1}$$

The radius can also be written as

$$r_c(mm) = 2.4 \times 10^{-2}\sqrt{E(eV)}. \tag{3.2}$$

For example, the cyclotron radius for antiproton cyclotron energy of 25 eV (velocity is 7×10^4 m/sec) is 0.12 mm. It is 0.6 mm for radial energy of 0.63 keV (or velocity of 3.5×10^5m/sec). The trap radius is 6 mm which corresponds to a cyclotron energy of 63 keV.

We trap the keV particles directly, without slowing them, by applying kilovolt potentials to the trapping electrodes for axial confinement after the particles have entered the trap. The kilovolt potentials must be applied quickly compared to the transit time of the particles through the trap. We have been able to apply 3kV potentials in about 20 ns using krytrons as described in Chapter 4 [53]. We describe briefly the first trapping of protons and antiprotons in the next two sections. Then the greatly improved antiproton trapping experiment will be discussed.

3.1 First direct trapping of keV protons

To investigate the trapping process, we obtained a 1 keV proton beam from a Duo Plasmatron ion source. A water cooled Helmholtz coil provided a 2 kG field and cylindrical trap electrodes were made of conventional 2 3/4 inch conflats and

vacuum pipes. The trap was differentially pumped by an ion pump. The pressure was as good as 2×10^{-8} Torr when the beam was off. However, hydrogen atoms entering the trap with the beam make the pressure worse, partly because neutral atoms are knocked off the walls by the beam. Protons were trapped from a pulse with instantaneous intensity of approximately 4 nA sent through the trap by suddenly raising the potential of the upstream electrode [7]. We held the protons for several milliseconds during which protons oscillated for several thousands of periods, and then quickly lowered the kV potential of the down beam electrode so that trapped protons could escape from the trap towards the channel plate detector. A multiscaler, started when the potential was lowered accumulated a time-of-flight spectrum of pulses from the channel plate. As shown in Fig. 3.1(b), the 1 keV protons trapped from the beam arrive at the detector first and make a distinct peak. Soon after, a low energy proton background begins arriving, followed by heavier background ions. These are from background gas ionized by the incident proton beam.

For a single catch of protons from the beam, approximately 10^2 energetic protons were trapped. The incident beam of 4 nA means that about 10^4 protons were within the trap so that approximately 1% of the available particles were trapped. The low trapping efficiency is due in large part to the low magnetic field and to the large spatial spread in the incident proton beam. This was greatly improved later.

3.2 First capture of antiprotons in an ion trap

As an important step to demonstrate the feasibility of loading and storing antiprotons in the trap, we set up a simple system in LEAR and demonstrated capturing antiprotons in an ion trap [9]. The outline of the trap electrodes, the

scintillator and the magnetic field is Fig. 3.2(a). The slowest antiprotons leaving the degrader are confined in 2 dimensions to field lines of the 6 T superconducting magnet and are so guided through the series of 3 trap electrodes. As the antiprotons enter the trap, a first ring-shaped trap electrode (the entrance endcap) and a main ring electrode are both at 0 volts. A third cylindrical electrode (exit endcap) is at -3 kV so that negative particles with energy less than 3 keV turn around on their magnetic field lines and head back towards the entrance of the trap. Approximately 300 ns later, before the antiprotons can escape through the entrance, the potential of the entrance endcap is suddenly lowered to -3 kV, catching them within the trap. The potential is switched in 20 ns with a krytron circuit developed for this purpose and is applied to the trap electrodes via an unterminated coaxial transmission line [53].

After antiprotons are held for sometime between 1 ms and 10 minutes, the potential of the exit endcap is switched from -3 kV to 0 volts in 20 ns [53], releasing the antiprotons from the trap. The fast releasing of particles allows the most sensitive detection, but results in saturation of the detection system when too many particles are released from the trap. The antiprotons leave the trap along respective magnetic field lines and annihilate at a beam stop well beyond the trap. The high energy charged pions which are released are detected in a 1 cm thick scintillator outside the vacuum system. A multiscaler started when the potential is switched records the number of detected annihilations over the next 6 μs in time bins of 0.4 μs. Time-of-flight spectrum of detected pions from antiproton annihilation is shown in Fig. 3.2(b). The antiprotons were held 100 s in the trap and then released from the trap at time $t = 0$. The spectrum includes 31 events which corresponds to 41 trapped particles when the detector efficiency of 0.75 is included. A second multiscaler records the pion counts over a wider time range with less resolution to monitor backgrounds. These numbers are lower limits since the detection electronics was clearly saturated.

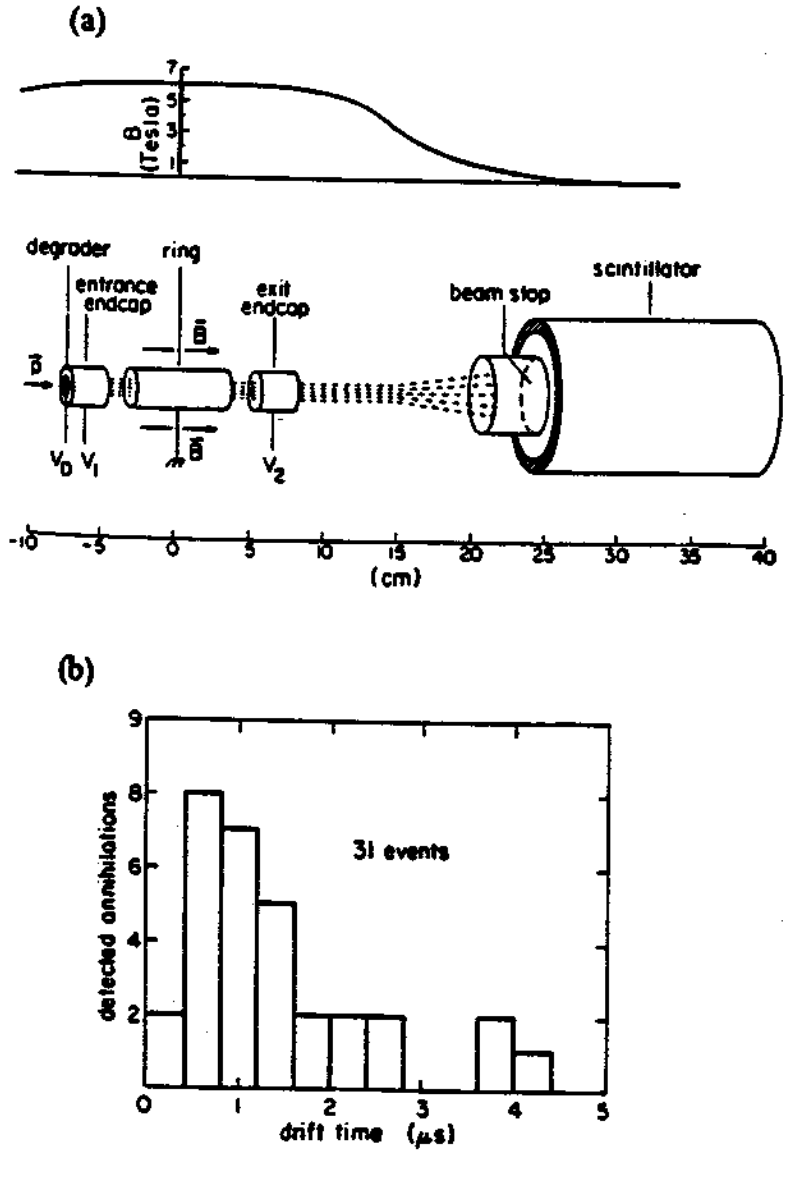

Figure 3.2: (a) Outline of the trap electrodes, the scintillator and the magnetic field. Magnetic field lines are indicated by dashed lines. (b)Time-of-flight spectrum of detected pions from antiproton annihilation.

3.3 Experimental layout for trapping antiprotons in the improved system with a 5.9 MeV antiproton beam

Fig. 3.3 shows the apparatus for trapping antiprotons from LEAR with 5.9 MeV incident energy. It consists of the degrader system described in Chapter 2, a 5.9 Tesla superconducting solenoid, scintillator counters for antiproton annihilation detection, a high vacuum enclosure for the open-end cylindrical trap [54], the cryogenic system for the solenoid, the trap, electronics control for performing experiment, and the data acquisition system.

The 5.9 Tesla **superconducting solenoid** with 10 cm (diameter) bore is made by Nalorac Cryogenics Corporation. The bore can be at room temperature or at 77 K. The solenoid is wound of single strand NbTi wire. Drift rate in the magnetic field is less than 1 part in 10^9/hr. The field homogeneity can be shimmed better than 1 part in 10^8 over a 1 cm diameter sphere. A special configuration of superconducting solenoid winding makes the superconducting system self-shielding against fluctuations in the ambient field [55]. The maximum shielding factor is 156 for a uniform perturbation [56]. There are two cooling reservoirs for the magnet cryostat. The liquid helium dewar volume is 47 liters with a hold time typically more than 3 months. That is a boil-off rate of order 20 ml/hr. The liquid nitrogen main reservoir has a volume of 92 liters. The boil-off rate is less than 200 ml/hr so that the hold time is more than two weeks. The 100 cm bore allows the access of the trap system and housing for detectors and degraders. An auxiliary dewar with a liquid nitrogen reservoir is under the magnet to allow the room temperature bore to be cooled to 77 K.

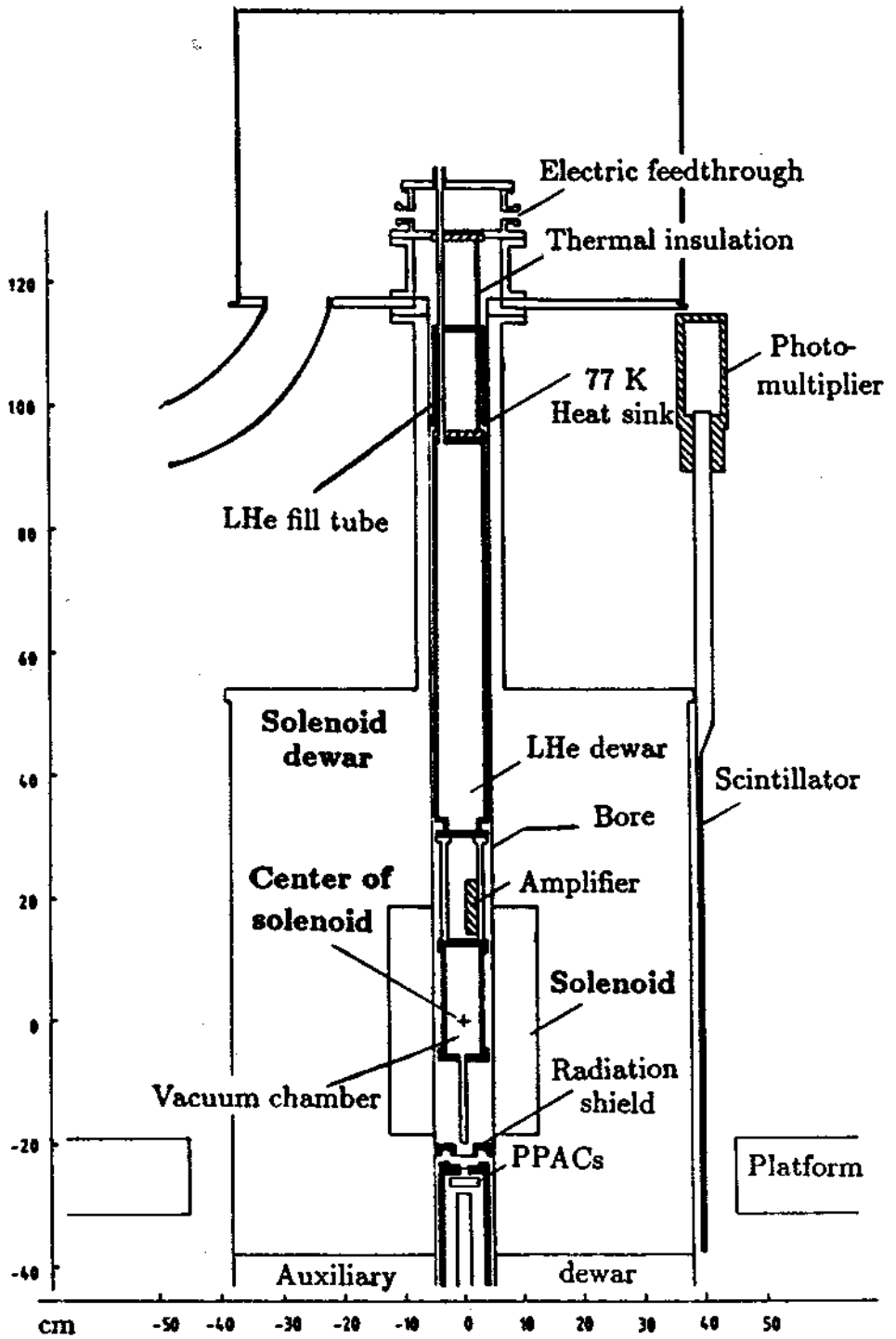

Figure 3.3: The apparatus for the antiproton trapping experiment.

A high vacuum enclosure (trap can) at the center of the solenoid houses the ion trap. A Ti window separates the magnet bore vacuum and the trap can vacuum. Up to 3 amplifiers have been mounted in the space between trap can and the LHe dewar. The amplifier will be described in Chapter 5. The liquid helium dewar has a volume of 4 litres and provides heat sink more than 5 days before a LHe refill is required. Electronic wires and cables exit the vacuum system via electrical feedthrough at the top of the magnet bore.

3.4 Scintillator detectors and the detection efficiency

There are six flat (1 cm thick) plastic scintillators (each with an active area of 0.76 m $\times$ 0.43 m) surrounding the solenoid dewar. The side view of a scintillator is shown in Fig. 3.3. The front view of one scintillator is shown in Fig. 3.4(a). The top view of the configuration of six scintillators is shown in Fig. 3.4(b). Antiproton-proton annihilation produces 2.9 charged pions in average [57]. Light generated by the charged pions go through light guides and hit the photo-cathodes of the photomultipliers (Hamamatsu phototube R2238). The gain is approximately 6×10^6 at a bias potential of +1300 V. The bias potential is off during the intense 300 ns antiproton pulses to protect photomultipliers which otherwise take many seconds to recover. A reed relay described in Chapter 4 turns the potential back on. It reaches 1.3 kV after 0.7 sec, due to the power supply current limit and RC constant in the phototube circuit. The quantity A, defined as the percentage of solid angle subtended to the position in trap axis by scintillators over 4π, as a function of height is shown in Fig. 3.4(c). The solid angle of scintillator coverage to the trap center is A = 70% of 4π and it varies very slow near the trap center. The solid

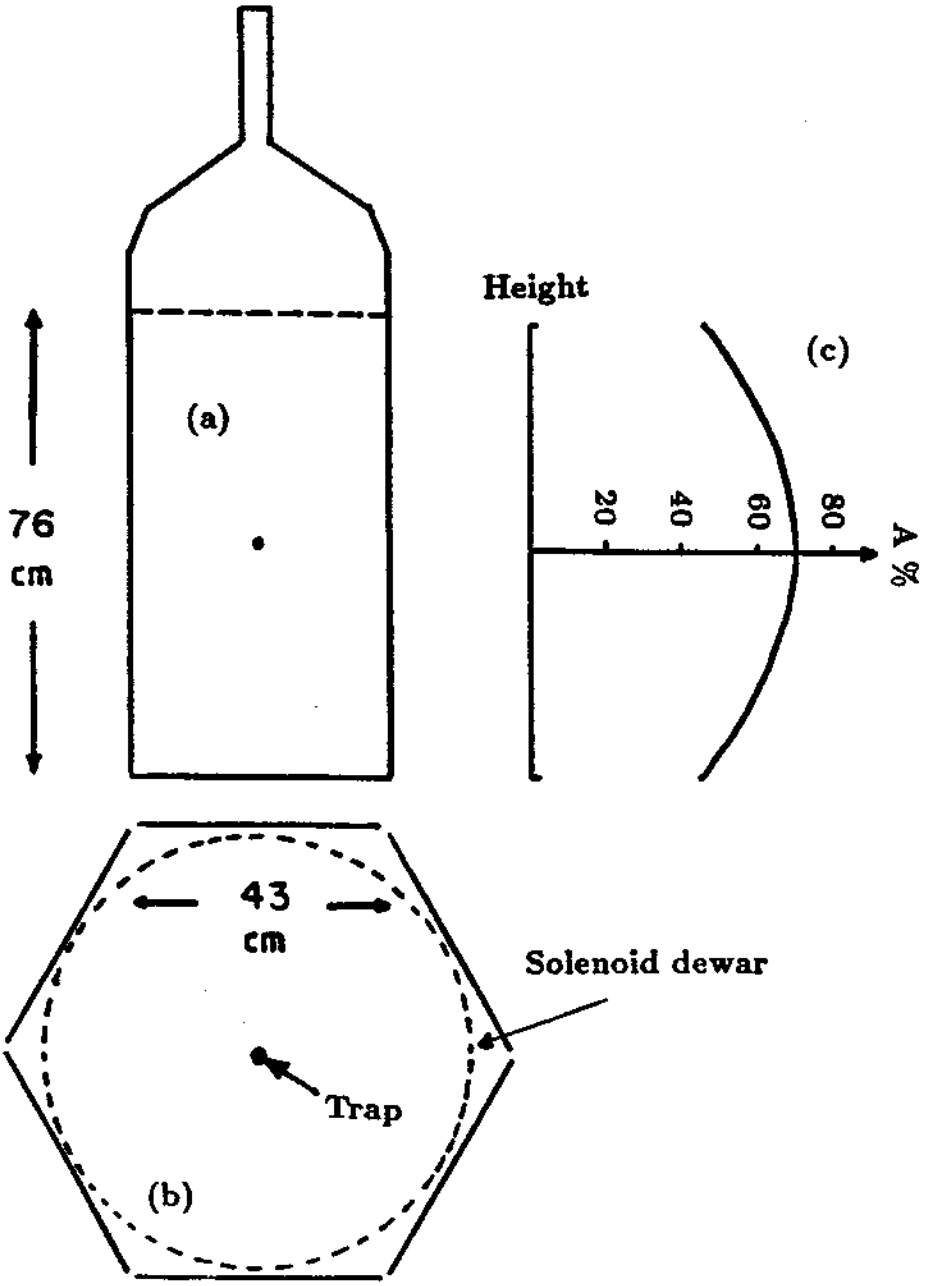

Figure 3.4: (a) Front view of a scintillator. (b) Top view of six scintillators configuration. (c) Solid angle coverage A as a function of height.

angle is only 1% smaller at the point 10 cm away from the trap center along the axial axis.

The detection efficiency of the scintillators is measured in slow extraction mode. For each antiproton coming from LEAR which is detected in the PPAC detectors, we measure the probability that the scintillators detect the annihilation. PPAC counters monitor the incident beam flux. The coincidence signals of PPAC and scintillators in 1 μs time window divided by the PPAC signals gives the efficiency. The efficiency of $70 \pm 2\%$ was measured when the 6 T magnetic field was absent. Correction due to 10% antiprotons struck on molybdenum grid which supports the mylar window in the PPAC detector is about +1.3%. Thus the efficiency is $71 \pm 2\%$ when the magnetic field is off. It is consistent to the pion multiplicity (average of 2.9 charged pions per antiproton annihilation [57]) and the solid angle subtended. Based on the pion decay channels, and the solid angle covered by scintillators, the detection efficiency is estimated to be below 88%. The energy loss of the pions decreases the efficiency to around 80%. The observed efficiency (71%) indicates the photomultipliers and the detection electronics have an average efficiency of 90%.

The magnetic field only has very small effect to relativistic pions. However, the presence of the magnetic field would decrease the gain of the photomultipliers and thus the detection efficiency. In the Fig. 3.5, the coincidence signals of PPAC and scintillators divided by the PPAC, C%, versus the scintillator counting rate are plotted when the 6 T magnetic field is on and off. The detection efficiency of the scintillators is obtained by extrapolating the counting rates to zero. The slopes are due to the antiproton annihilations detected by scitillators but undetected by PPAC since the PPAC has lower detection efficiency at the bias potential used in the experiment, and also due to the background signals from scintillator signals. The efficiency is $46 \pm 3\%$ when the 6 T is on. The correction due to the Mo grid is 0.9%. Therefore, the efficiency for the scintillators detection of an annihilation

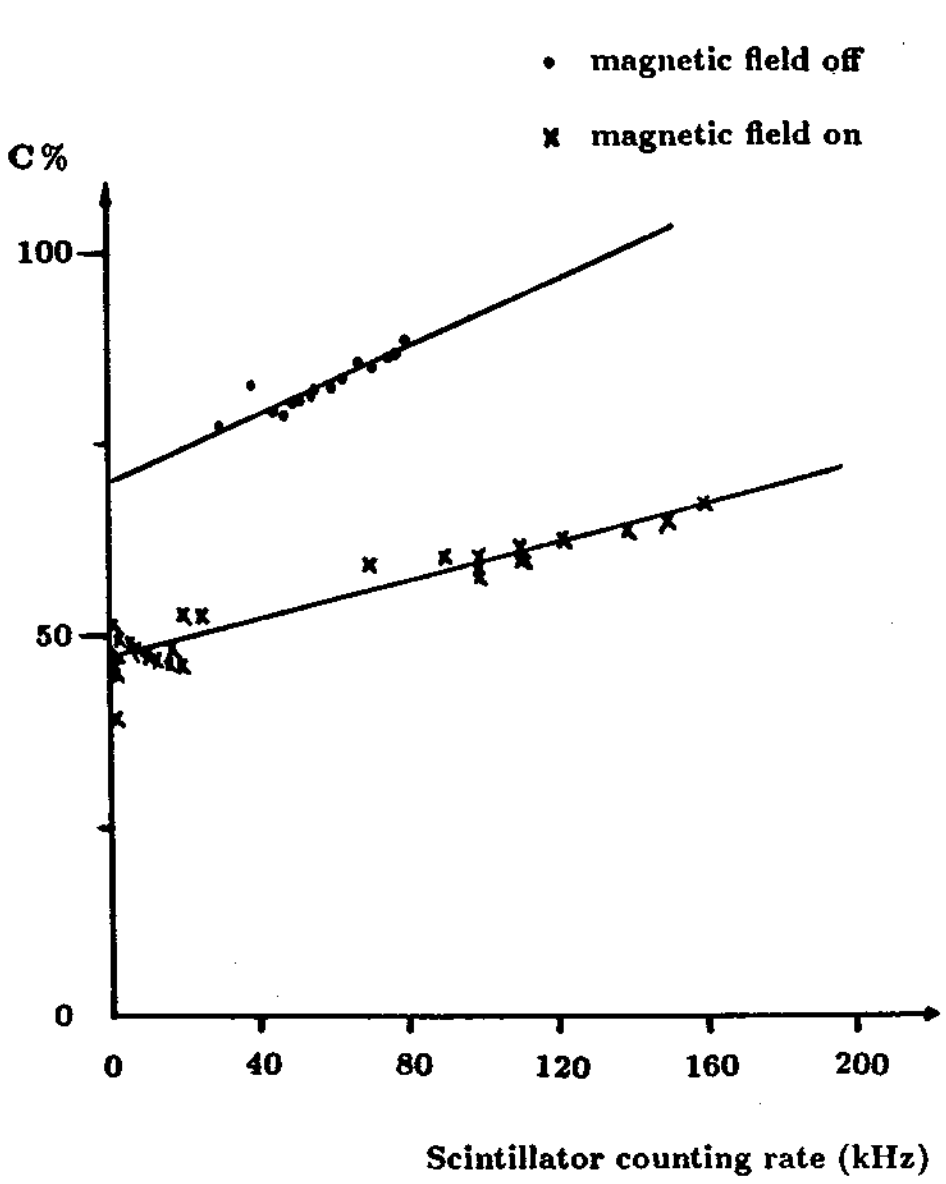

Figure 3.5: Coincidence signals of PPAC and scintillators divided by the PPAC, C%, versus the scintillator counting rate. The scintillator detection efficiency is obtained by extrapolating the counting rates to zero.

event in the trap is measured to be $47 \pm 3\%$.

3.5 Multiple scatterings

As antiprotons pass through a medium they are deflected by many small-angle nuclear elastic scatterings or multiple scatterings. A parallel beam of particles penetrating degrader spreads out into a cone by multiple Coulomb scattering. The distribution of deflection angle θ for particles passing through foils is approximately Gaussian [27]

$$F(\theta)d\Omega = (1/2\pi\theta_0^2)exp[-\theta^2/2\theta_0^2]d\Omega \tag{3.3}$$

with the characteristic angle θ_0. The relative number of particles entering a cone of half angle θ_0 is 39%. As shown in Fig. 3.6, the material that causes the multiple scattering in our trapping experiment is labeled and the angle θ_0 for each layer is indicated. The 5.9 MeV antiprotons penetrating a 10 μm thick Ti foil have $\theta_0 = 0.7°$. The θ_0 for the beam going through the material before the final Al foil (in the trapping experiment, the 117 μm Al foil is moved back about 20 cm) is approximately $2° = 0.035$ radians. The displacement ($L\theta_0$) after particles traveling L = 20 cm is 0.7 cm. Particles hitting the centre of the first Ti foil of the degrader will have a spot size with a diameter of 1.4 cm (which is slightly larger than the trap diameter) on the Al foil with 39% of the beam. This corresponds to a diameter of approximately 0.5 mm at PPAC detectors. In this configuration, the first Ti foil is located very close to the solenoid center so that the scattering due to this foil does not dominate the overall multiple scattering effect. However, if the first Ti foil is 1 m below the final degrader (Al), only about 12 % of particles from the beam could enter the trap without considering scattering effects from other degraders. To minimize the distance, we have our extension of LEAR beamline protrudes up into the bore of the superconducting solenoid as mentioned in Chapter 2.

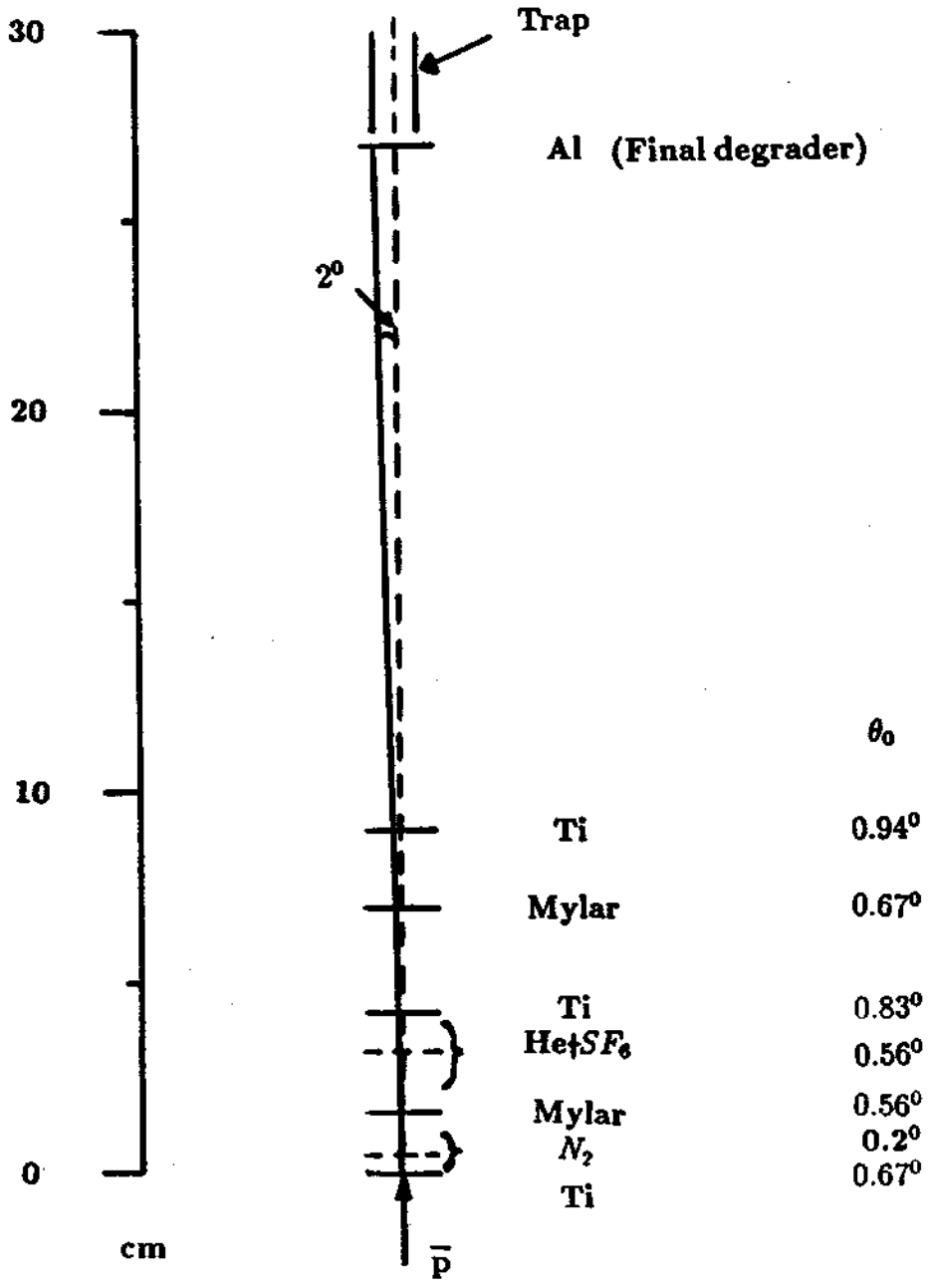

Figure 3.6: Multiple scattering. Each layer is listed in order in Table 2.1 (along with the equivalent thickness of aluminum and the energy loss).

3.6 Electronics

During fast extraction, up to 3×10^8 antiprotons are ejected from LEAR in one pulse with a duration of 300 ns. The potential bias on PPACs is reduced to much lower voltage, typically 100 V, to avoid secondary particles causing sparks. This potential corresponds to a reduced field strength of 13 V/cm/torr. The electrons (and ions) produced by antiprotons in the isobutane gas are proportional to the incident particle numbers, and are collected with the aid of the electric field. Similar to the detection scheme discussed in Chapter 2, signals from 10 channels are amplified by a factor of 10. They are attenuated by a factor of 2 or 20 and fed into an integrating ADC. In Fig. 3.7(a), electronics for one channel of PPACs is shown. A storage scope for one central PPAC channel is used to measure the beam time structure. It will be mentioned again in the timing system. The computer read out from the ADC channels shown in Fig. 3.7(b) shows the beam profile during fast extraction. The higher column in each channel corresponds to an attenuation of 2. The lower one is with 20. The spot size on the PPAC detectors is about 3 mm×3 mm which is mainly due to the beam size. The additional spread due to the multiple scattering is relatively small (0.5 mm) as discussed in Section 3.5.

The **high voltage (HV) ramp** is achieved by using low voltage ramp generator controlling a KEPCO (OPS 5000) high voltage power supply (Fig. 3.8). Resistors are chosen so that a low voltage ramp generator has a linear ramp output voltage from −5 V to 0 V produces a linear high voltage ramp from −3 kV to 0 V. Typically we used a 90 ms ramp for this experiment which is a rate of 31 V/ms. However, this rate can be (and was) easily adjusted to make it up to 100 times faster or 10 times slower. The high voltage ramp output is connected to the exit electrode of the long trap. A resistor divider is used to monitor the HV ramp with a scope. The divided signal is also sent to a waveform digitizer (Lecroy 2256A) and recorded in a computer together with a multiscaler spectrum of the

(a)

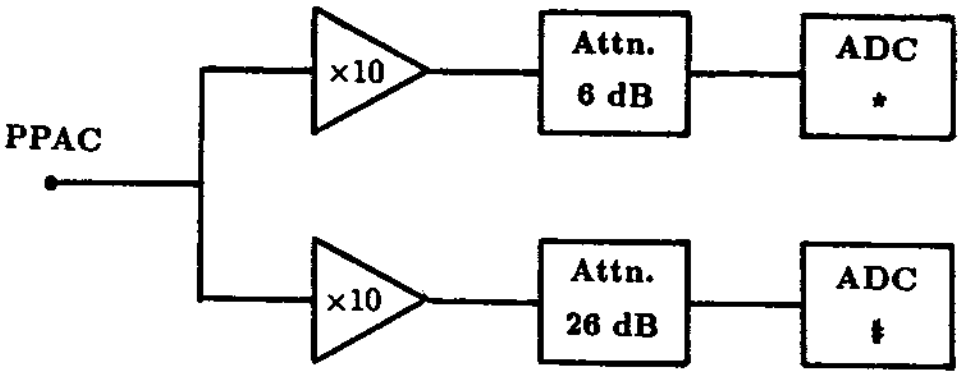

(b)

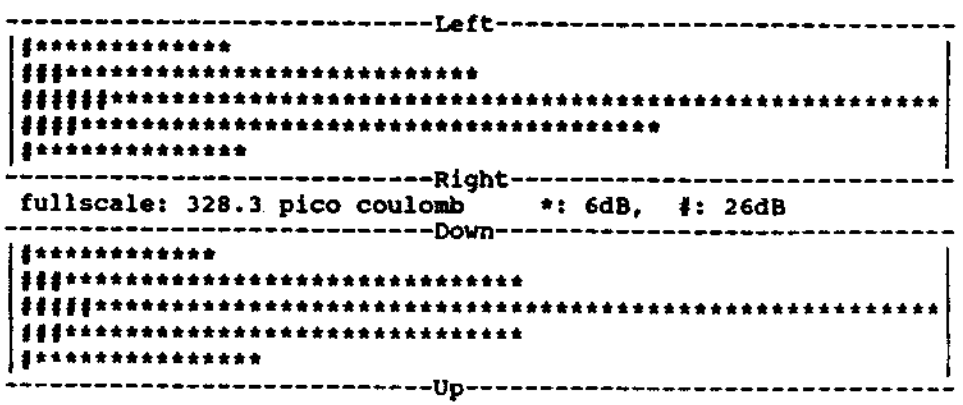

Figure 3.7: (a) Electronics for one channel of the PPACs. Other 9 are identical. (b) Beam profile during fast extraction.

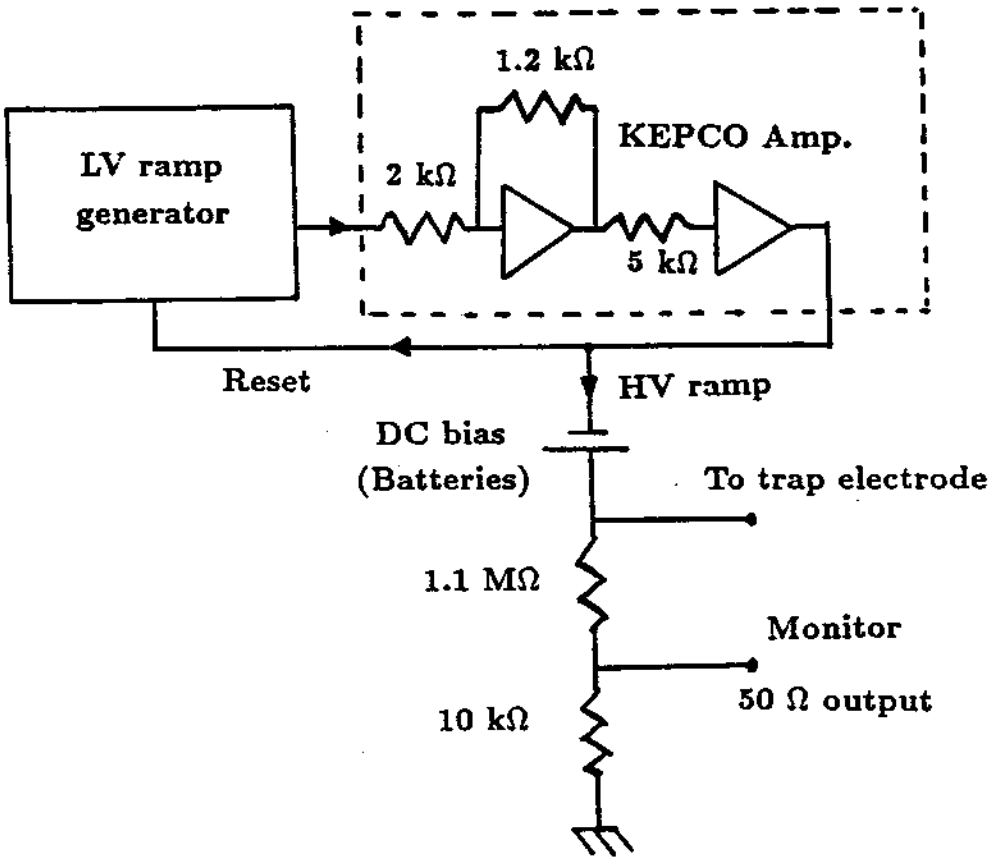

Figure 3.8: Block diagram of the high voltage ramp.

pions from antiprotons which escape the trap as the well depth is lowered.

The timing sequence and block diagram for the timing electronics are shown in Fig. 3.9 and Fig. 3.10. The timing sequence for trapping antiprotons is triggered by a LEAR warning pulse 2 μs before the beam arrives. This warning pulse starts a programmable digital delay/pulse generator (SRS Model DG 535) which has multiple outputs of TTL and NIM signals. One output signal triggers the antiproton load pulser to rapidly apply -3 keV to the degrader to trap particles at a selected time after antiprotons pass through the PPACs. The time difference t_L between the antiproton pulse and the leading edge of the load pulser is measured by a storage scope. The width of the beam pulse (typically 300 ns) reflecting the adjustable LEAR kicker length is also measured by the same scope. The beam profile is recorded by the ADC channels (Fig. 3.7). The exit electrode is at -3 kV potential initially. A potential well for negative particles is formed once the load electrode is switched on. After a preset time (the trapping time or hold time), the function generator sent out a pulse to trigger the HV ramp while at mean time another pulse starts the Joerger multiscaler for counting antiproton annihilations when particles leak out the trap because the well depth is reduced by the ramp.

3.7 Experimental results of trapping study of incident 5.9 MeV antiprotons

In the antiproton trapping experiment, pulses of 5.9 MeV antiprotons leave LEAR beam line upwards through various material (see Table 2.1 and Fig. 3.6) and finally pass through a Ti vacuum window into the trap can, a complete sealed vacuum enclosure which is cooled to 4.2 K. The trap electrodes and the potential

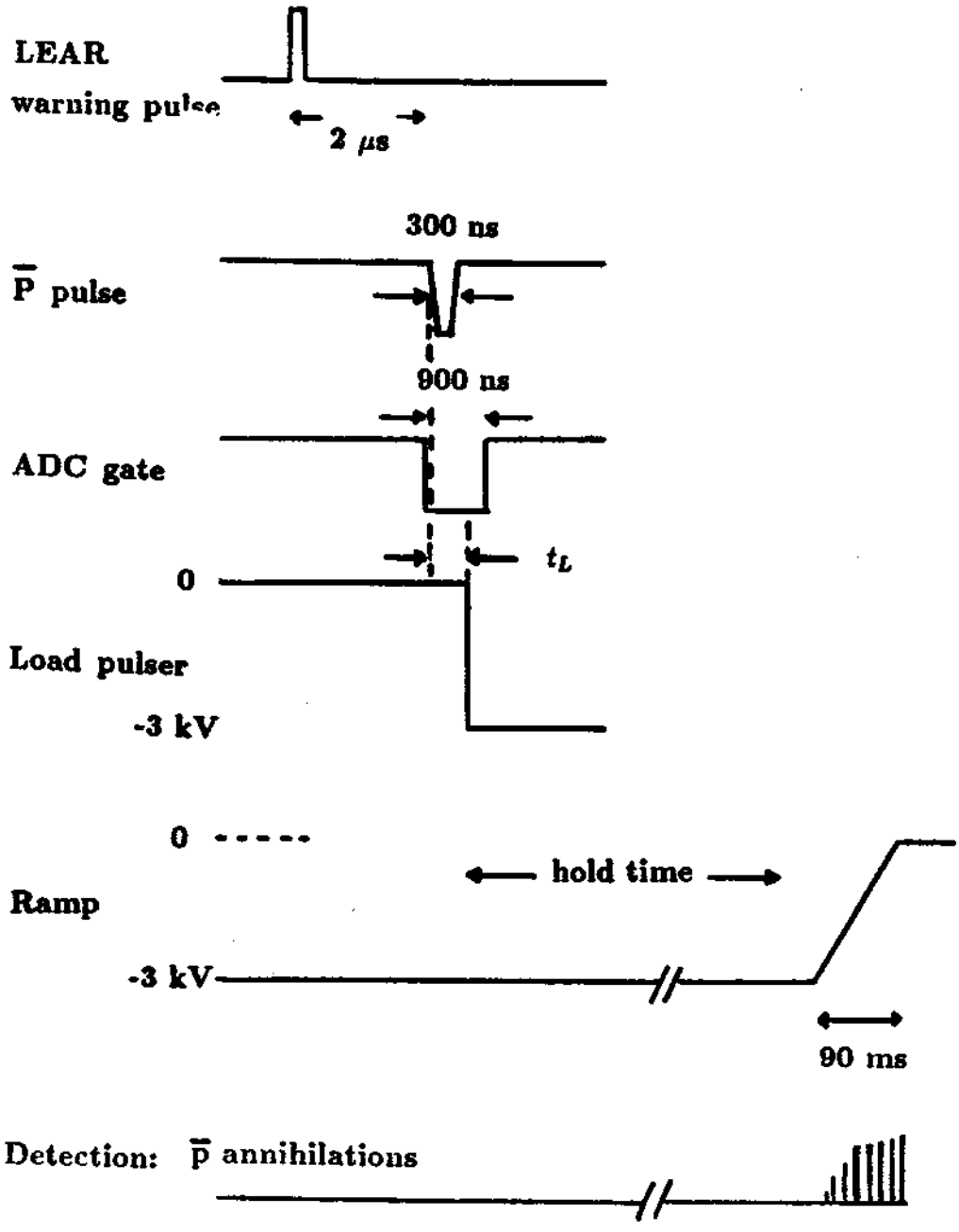

Figure 3.9: Timing sequence from LEAR warning pulse, to LEAR beam detection by PPAC, potential well switching for loading antiprotons, HV ramp to release trapped particles, and particles energy analysis.

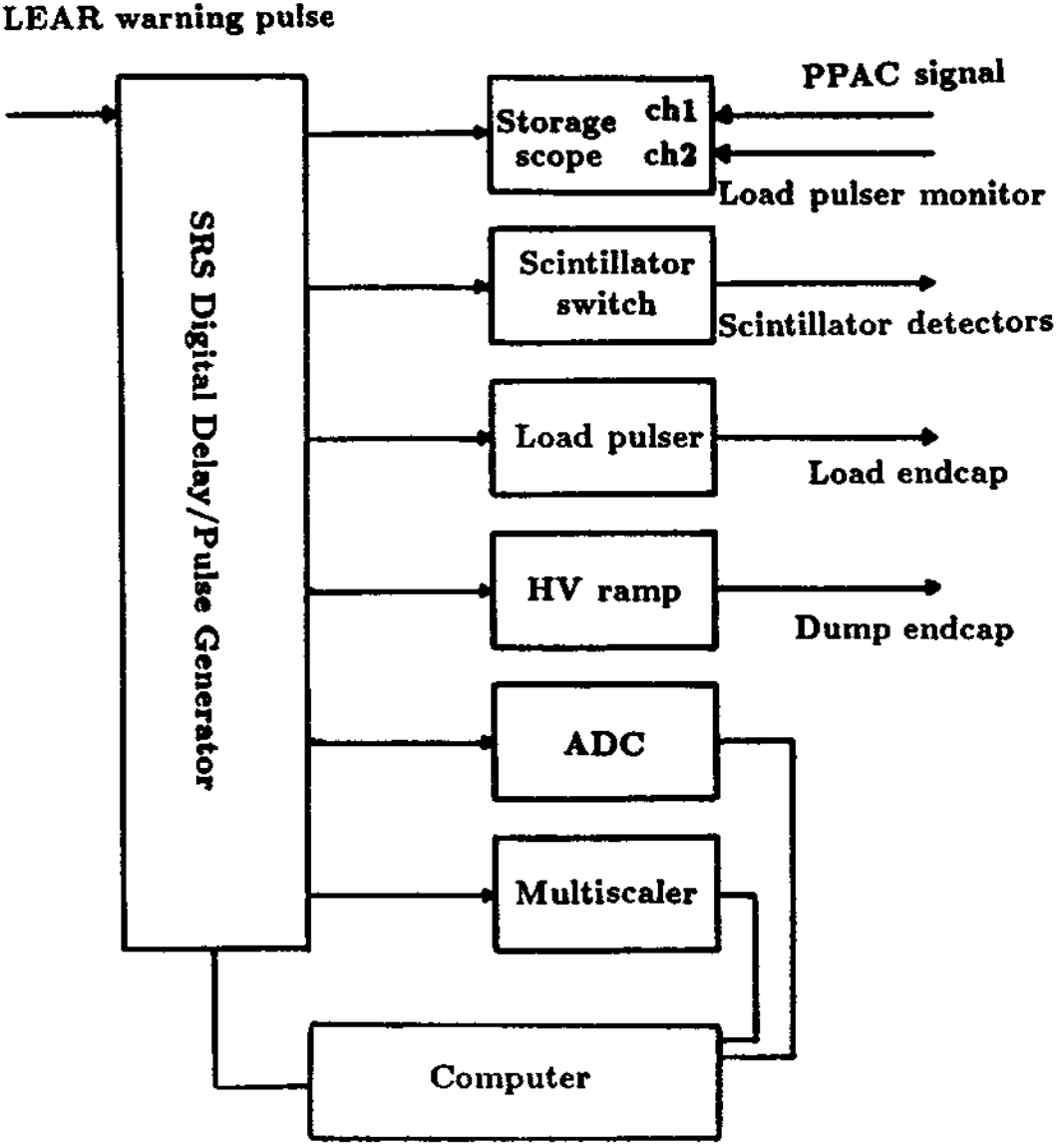

Figure 3.10: Timing block diagram

along the axis of the trap are shown in Fig. 3.11. The ion trap inside consists of an aluminum plate at the bottom which is our load electrode connected with the load pulser, a series of copper cylinders above which can be separately biased to shape the trapping well, and a copper cylinder (or a plate) at the top as our exit electrode attached to the HV ramp. The antiprotons are at approximately 3.7 MeV before they enter the trap by passing through the aluminum plate and their energy can be tuned slightly by adjusting the contents of the gas cells to maximize the number of antiprotons [10] which emerge from this degrader after being slowed below 3 keV, as described in Chapter 2.

Secondary electrons liberated from the degrader by antiprotons are eliminated by biasing the degrader at +5 V or higher with respect to the first cylinder at the bottom. If this is not done, we end up with a trap filled with electrons after the intense antiproton pulse arrives. Similar to the experiments of first capture of protons and antiprotons, the cylinders between load and exit electrodes are grounded (or at a potential much less compared with 3 kV). The upper exit electrode is biased at −3 kV to turn around antiprotons with kinetic energies (along the beam axis) below 3 keV. After the pulse of antiprotons is within the electrodes of the long trap, the potential of the Al degrader is quickly switched to −3 kV, completing the ion trap and confining the particles.

After a preset hold time, the potential of the upper electrode is ramped through 0 V. If the antiproton energy is not too low, the period of the axial oscillation along the magnetic field is very short compared to the 90 ms ramp. For example, oscillation period is about 20 μs for 1 eV antiprotons while the ramp time from −1 V to 0 V is 22 μs. Here the trap length L = 16 cm is used. The oscillation period in the long trap is approximately: $t(ns) = 44L(cm)/\sqrt{E(keV)}$. Therefore almost all the particles in the trap satisfy this condition. Antiprotons with energies exceeding the ramp voltage leak out the trap and their annihilation signals detected

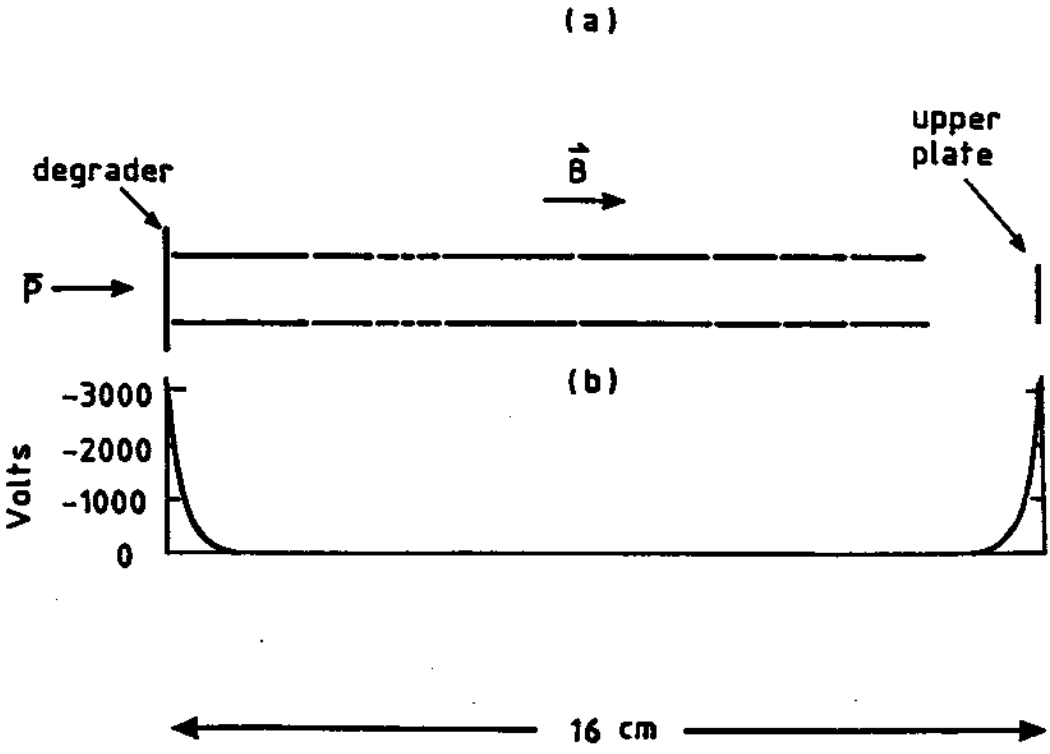

Figure 3.11: (a) Trap electrodes. (b) The potential along the axis of the trap.

by scintillators are recorded in a multiscaler which starts counting when the HV ramp starts. The multiscaler spectrum makes a direct measure of the axial energy.

Fig. 3.12, shows a spectrum of released antiprotons from the long cylindrical trap after being held for 100 sec. Antiproton annihilations are plotted as a function of the high-voltage endcap potential which ramps down with a rate of 31 V/ms. Approximately 6×10^4 counts are detected by scintillators which means about 1.3×10^5 antiprotons had been trapped for 100 sec. The average energy of those antiprotons is 854 eV. The spectrum peaks at low energies and falls off at higher kinetic energies as the antiproton energy approaches the 3 keV well depth. The low energy peak is only present for the most intense bursts of antiprotons from LEAR. It seems to be due to electron cooling by secondary electrons liberated from the degrader when the most intense pulses of antiprotons from LEAR hit it. Approximately 500 counts in one single channel at low energy peak which corresponds to an average energy distribution of 1 annihilation count for every 10 meV energy window. Here we used the energy resolution of 6.1 V/channel. Even when we just count the flat part of the spectrum, there are 200 counts or 400 antiprotons/channel. Then the average particle distribution is 1 antiproton per 15 meV.

The scintillator detection shows that the double hits (when two scintillators detecting the same antiproton annihilation event) to single hit ratio is 0.36 which was reproducibly measured. Using the number of antiprotons measured to leave LEAR (3×10^8), we trap antiprotons from LEAR with an efficiency of 4×10^{-4} or 1.4×10^{-4}/keV. It is very close to our degrader test result of 1.6×10^{-4}/keV which is a lower limit of the antiproton yield. Trapping efficiency can vary a lot depending on LEAR beam tuning (such as beam focusing and steering, pulse width, shape and timing), and our experimental setting (such as the amount of degrader and the quality of the degrader, and load timing). Less trapped antiprotons by a factor

of 10 is more typical when the LEAR beam is not optimally tuned.

The number of antiprotons with axial energies less than 3 keV captured in the long trap, normalized to the number of antiprotons in the pulse (PPAC signals) from which these were trapped, is plotted as a function of the gas mixture (Fig. 3.13). The hold time for each trial (represented by a point in the plot) was 10 sec. The width (FWHM) of the curve is equivalent to 33% of SF_6 change in gas cell 2. In energy it is 0.17 MeV (or 12 μm in Al thickness) which is 23% of the total degrader tuning range by gas cells. The gas mixture corresponding to maximum trapping efficiency is reproducible.

With the gas mixture optimized and an antiproton hold time of 10 sec, we plot the trapping efficiency versus the time between when the antiproton pulse enters the trap and the high-voltage potential is switched on by the load pulser Fig. 3.14. The time structure of the antiproton pulse is shown in Fig. 3.14(a). The flat top is 200 ns. The width is typically 300 ns with a 100 ns rise time. An arrow marks the beam entering trap. Relative trapping efficiency versus the load pulser timing t_L (see also Fig. 3.9) is plotted in Fig. 3.14(b). When the potential is switched on too early and most antiprotons are not in the trap yet, the trapping efficiency is very low. As we delay the load pulser trigger to allow more particles to enter the trap, trapping efficiency rises rapidly. As expected, a peak appears right after the whole pulse of beam entered the trap. If the high-voltage switching time is further delayed, particles with higher energy turned around by -3 kV at the upper electrode have time to hit the degrader, causing the drop of the efficiency to the right. For a 16 cm long trap, the period is 430 ns for 3 keV antiprotons, and it is 730 ns for 1 keV particles. Particles with lower energy will take longer time in the trap so that the trapping efficiency is not critically dependent upon the timing.

In one trial, antiprotons were captured and held in the long cylindrical trap for

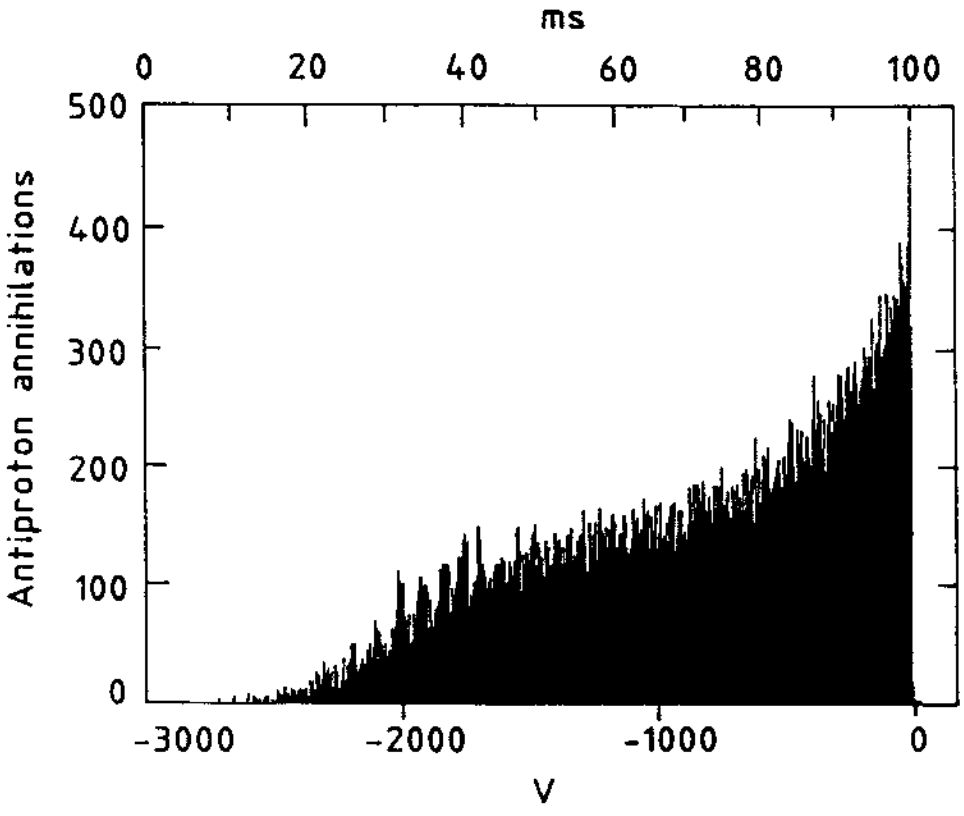

Figure 3.12: Spectrum of released antiprotons from long cylindrical trap after bei held for 100 sec.

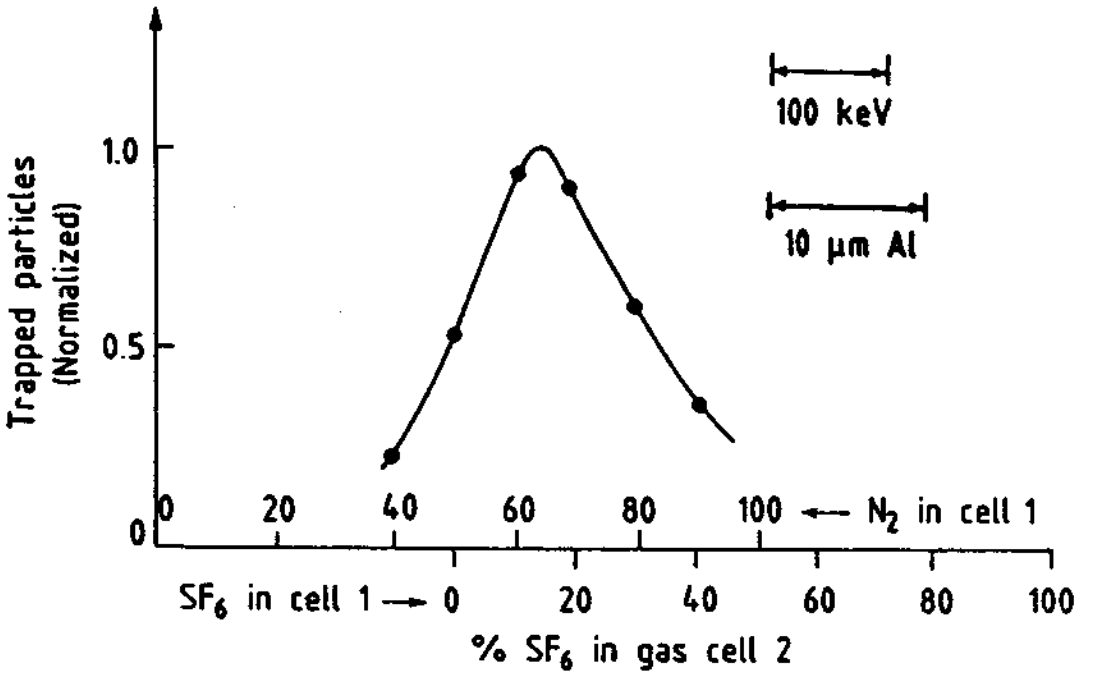

Figure 3.13: Trapping efficiency versus degrader thickness.

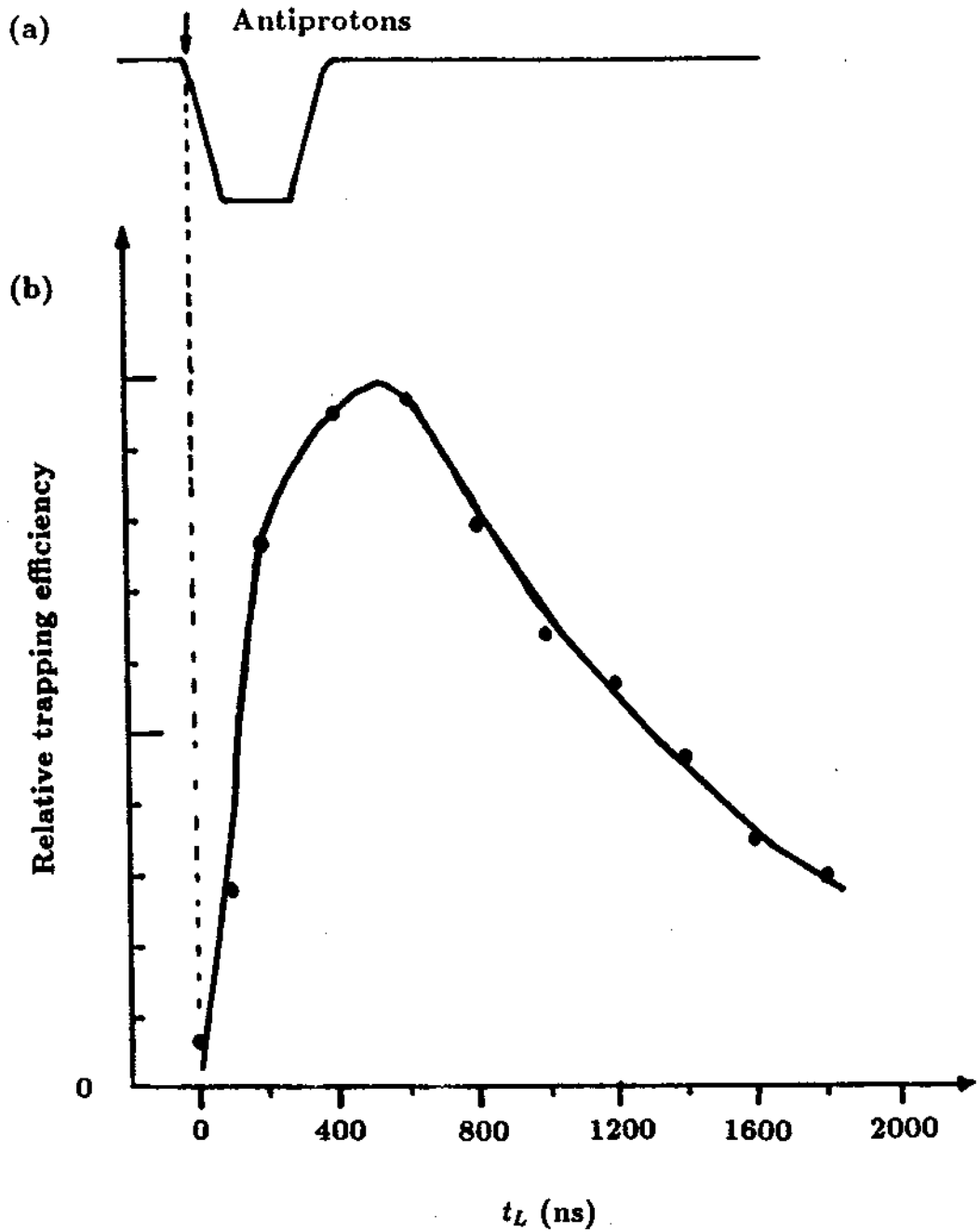

Figure 3.14: Trapping efficiency versus load pulser timing.

64 hours (2.7 days). There were 3933 annihilation counts (representing 8368 antiprotons) recorded in the spectrum (Fig. 3.15). Based on the PPAC signal for this trial and the calibration of trapped antiprotons per unit PPAC signal, we estimate the initial number of trapped particles are less than 2.8×10^4. Thus a lifetime in the long trap of greater than 54 hours is established if we assume that the particles decay exponentially. The average energy of the particles is 0.8 keV, similar to the energy spectrum after shorter hold time.

Although the energetic antiprotons initially loaded into the long trap remained for days, the containment time for low energy antiprotons was significantly shorter. Within several hundred seconds low energy antiprotons were already lost from the long trap. The lifetime for approximately 10^7 electrons in the long trap was measured to be only 5 to 10 seconds, though much longer storage times were observed for shorter sections. One might expect that a long cylindrical trap would be unstable for low energy particles as the potentials applied to the end plates are exponentially screened from the interior, leaving only a homogeneous magnetic field inside. Since no preferred axis is indicated, the particles can be moved across the field lines by stray potentials within the electrodes. An electron storage time inversely proportional to the length squared for similar traps has been observed in plasma physics experiments [58]. This functional dependence has not been explained, but the proportionality constant increased when stray potentials were minimized and axial symmetry was maximized. Our observed lifetime also decreases with trap length. The containment time for low energy particles are greatly improved when we use gold plated short electrodes to produce a high quality electric quadrupole potential (see Chapter 5 and Chapter 6).

We have demonstrated that up to 1.3×10^5 antiprotons from a single LEAR pulse were stored in the ion trap. The trapping efficiency is more than 4×10^{-4}. The kinetic energies of trapped antiprotons are between 0 eV to 3 keV. Further

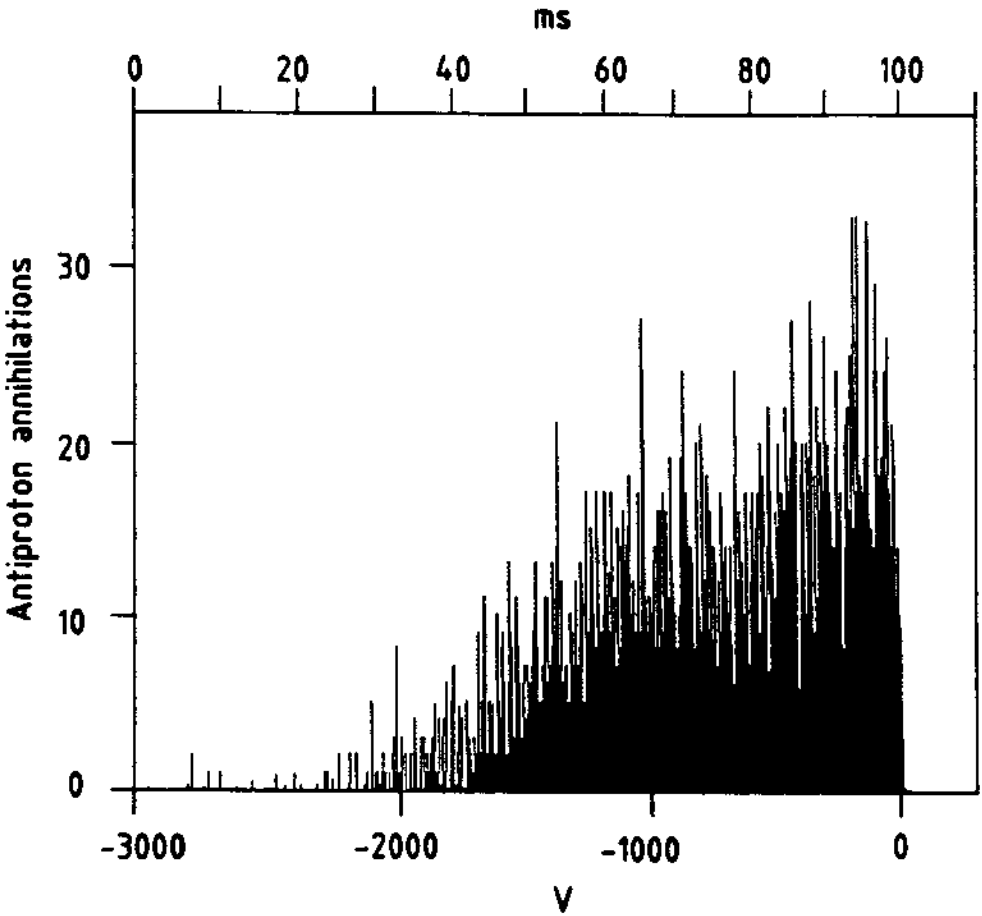

Figure 3.15: Spectrum after holding antiprotons for 64 hours in the long trap

slowing and cooling are realized by collisions between electrons and antiprotons within the ion trap. This will be discussed in Chapter 5 where the width of the energy spectrum is squeezed and narrowed drastically.

Chapter 4

High-voltage switching for in-flight capture of keV antiprotons in an ion trap

The in-flight capture of keV antiprotons in an ion trap requires that the -3kV potentials on electrodes of a trap near 4.2 K be switched on and off with switching times less than 20 ns. These rapidly switched potentials are applied via transmission lines which are not terminated at the trap, in order to avoid an unacceptable heat load on the helium Dewar. Simple high-voltage switching circuits are constructed using krytrons and reed relays [53]. A krytron provides the rapid switching and stays on just long enough for a reed relay to kick in and maintain the switched state indefinitely.

Fig. 4.1 is a simplified diagram of the trap electrodes and the idealized high-voltage switches which are used. In practice, the switch symbols S_1 and S_3 represent electronic circuits (discussed below) which are capable of switching times less than 20 ns. A pulse of antiprotons travels along the axis of the three cylinder electrodes from the left. A strong homogeneous magnetic field is directed along

this axis over the whole length of the electrodes. This magnetic field confines the charged particles in the two transverse dimensions to a field line. As the antiprotons approach, the high-voltage switches are set as shown in the figure. The left cylinder (load endcap) and the central cylinder (ring) are thus grounded while the right cylinder (dump endcap) is at -3kV. As antiprotons with kinetic energies below 3keV approach the negative dump endcap, they turn around on their magnetic field lines and head back toward the entrance of the trap. Approximately 300ns later, before the particles can escape through the entrance, the load switch S_1 is closed, lowering the potential of the entrance endcap suddenly to -3kV and trapping particles within the trap. The antiprotons are held as long as desired by opening switch S_2. Then, the dump switch is closed to quickly raise the potential on the exit endcap from -3kV to 0V, releasing the antiprotons from the trap. The antiprotons leave the trap toward the right and are detected.

A crucial feature of the high-voltage switching is the transmission lines which connect the switching circuits to the trap electrodes. One function of the transmission line is to thermally isolate the switching units at room temperature from the trap electrodes which are cooled to near 4.2 K. This is easily accomplished with a small diameter 50-Ω coaxial cable of adequate length, made of stainless steel and Teflon. Also, the Transmission lines are not resistively terminated at the trap end. Thus, there is no heat generated at the cold end of the transmission lines.

The capacitance to ground of each endcap electrode is very small, of the order of 20 pF or less. For the time scales we are interested in, switching times less than 20ns, the trap end of each transmission line is thus essentially open. The theory of open transmission lines is well known [59]. Consider the load switch first, operating at negative potential $-V_0 = -3$kV. With an open switch S_1 and a closed S_2, as in Fig. 4.1, the 470-kΩ resistor pulls the potential of the load endcap to ground potential. the 0.02-μF capacitor is, meanwhile, charged up to $-V_0$ through the 35-MΩ

isolation resistor. When the switch S_1 is closed, the switch end of the transmission line immediately goes to $-V_0/2$ because the voltage across the capacitor is divided across the 50-Ω resistor and the effective 50-Ω impedance of the transmission line. This line appears to be of infinite length until enough time has elapsed for the disturbance to travel to the trap, reflect off the essentially open end of the line, and return to the switch end of the transmission line. However, the potential $-V_0/2$ is doubled back to $-V_0$ at the trap in order that the boundary conditions for an open end transmission line be satisfied. One transmission line transit time τ after the switch S_1 is closed, the potential at the trap electrode thus suddenly changes from 0 to $-V_0$. At 2τ, the reflected wave returns to the switch end of the transmission line so that the potential at this switch end changes from $-V_0/2$ to $-V_0$. For a long cable, we clearly observe this step pattern. The 50-Ω resistor terminates the wave traveling back from the trap so that no further reflection occurs. On a much longer time scale, the 0.02-μF capacitor discharges through the 470-kΩ resistor with a time constant of 9 ms. This is adequate time for switch S_2, a reed relay in practice, to be opened in order to stop the decay in the potential. If this is done quickly enough, the load endcap potential will remain near $-V_0$ indefinitely.

Analogous arguments pertain to the more simple dump switch on the right of Fig. 4.1. When the switch is closed, the dump endcap potential changes from $-V_0$ to 0 at one cable transit time τ later. No second switch is needed. When the dump switch is opened, the dump endcap capacitance to ground and the cable capacitance is slowly charged up through the 27-MΩ isolation resistor. For the cable we used, this time constant was typically 7 ms. A slow linear ramp used for dumping was discussed in Chapter 3.

The fast high-voltage switching is done with KN22 krytron tubes. These small and versatile tubes are well known for other applications, see EG&G Data Sheets K5500C-2 (1984), K5503B-3 (1981), K5502B-3 (1984), and Ref.[60]. A krytron is

filled with hydrogen gas and normally offers a very large resistance between the anode and cathode. A small discharge is maintained continuously between the extra keep alive electrode and the cathode to prepare the tube for firing. When a voltage spike of greater than 750 V, with a rise time less than 1 μs, is applied between the grid and cathode, the tube discharges and the resistance between the anode and cathode becomes very low. When the discharge current falls below 10 mA for longer than 100 μs, the discharge stops.

The actual high-voltage switching circuits used to capture antiprotons in flight are shown in Fig. 4.2. Analogous circuits for proton capture are shown in Fig. 4.3. The krytron in Fig. 4.2(a) is the switch S_1 of Fig. 4.1. The reed relay is switch S_2. The reed relay we used opened with a switching time and jitter of order 1 μs. The closing time delay and jitter was much worse but was not important for these circuits. The measured waveform shown to the right of each circuit indicates the ideal behavior of the potential at the essentially open end of the transmission line at a trap endcap. The measured waveforms closely approximate these waveforms in each case. The dashed waveform in Fig. 4.2(a) and 4.3(a) indicate the consequence of leaving the reed relay closed. Several extra resistors are added to the antiproton load switch to ensure that the anode remains more positive than the grid and cathode to keep the anode remains more positive than the grid and cathode to keep the krytron from back firing. This slightly changes the potentials applied to the load endcap from $-V_0$ and 0, but not a significant amount with the values chosen.

Each switched potential is monitored at the switching units with identical capacitive monitors, as shown. The properties of such a monitor are well known[59], even though at first glance it may seem strange that the oscilloscope input impedance must be high. This is done so that the scope end of the monitor cable is virtually an open circuit. The capacitive divider divides the high voltage $-V_0$

down to a reasonable level which can be handled on most scopes

$$V_m = -V_0 C_1/(C_1 + C_2) \approx -V_0/200, \tag{4.1}$$

where C_1 =5 pF and C_2 = 1000 pF. On time scales short compared to the transit time in the monitor cable τ, the potential at the switch end of the monitor cable is $V_m/2$. When the disturbance gets to the open end of the transmission line at time τ , the open circuit boundary condition forces the doubling of the potential so that V_m is actually measured at the scope. For times larger than 2τ, both ends of the monitor cable are at V_m. The 50-Ω resistor terminates the reflected wave so that there are no further reflections. We have verified that the monitor works reliably out to the very large times at which the 1000-pF capacitor is discharged through the scope input resistance, at a time of approximately 1 ms in our case.

Figure 4.4 shows the reed relay control circuit used for load circuits. This is not at all critical but works very well with the relay (DRVT-10-658 reed relay ordered from Newark Electronics) and solenoid (The Guardian Electronic Series 200 relay solenoid). The reed relay circuit is located far enough (approximately 1.5 m above) from the center of the superconducting solenoid so that the magnetic field from the superconducting solenoid does not interfere with the solenoid operation. Figure 4.4 also shows the krytron trigger circuit which is used in each of the four switching circuits. The diode driver on the left converts the rising edge of TTL pulse into a light pulse sent into an optical fiber, which isolates the control circuit from the floating trigger circuit. The infrared emitting diode MFOE71, detector MFOD72, and low-loss micron plastic fiber optics cable (such as Arthur Cat. No.276-228) for high voltage isolation are used. The MFOE71 diode has a peak wavelength of 820 nm at a forward current of 100 mA. The optical rise and fall time are 25 ns. The MFOD72 detector has a turn-on time of 0.01 ms as specified in Archer Cat. No.276-225. The battery powered trigger circuit uses a fast 1:40 transformer to generate the high voltage spike needed to trigger the krytron. The delay time from

TTL input to the high-voltage switching is approximately 500 ns at $V_0 = 3$ kV. For the load circuits shown, a TTL falling edge was applied to the input of the reed relay driver at the same time as a rising TTL edge was applied to the diode driver. The high voltage was then applied to the load endcap with a switching time of less than 20 ns and yet remained applied as long as the input to the reed relay driver remained low.

A possible improvement is to use a krytron KN22B which is rated at 8 kV or to use two KN22 krytrons in series to double the switching potential. Similar circuits could also be constructed with a thyratron.

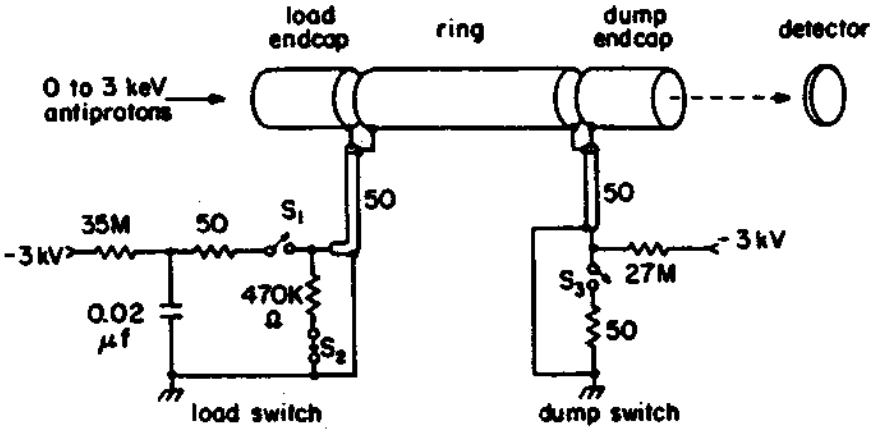

Figure 4.1: Simplified outline of the Penning trap electrodes and the idealized high-voltage switches used to capture antiprotons in flight.

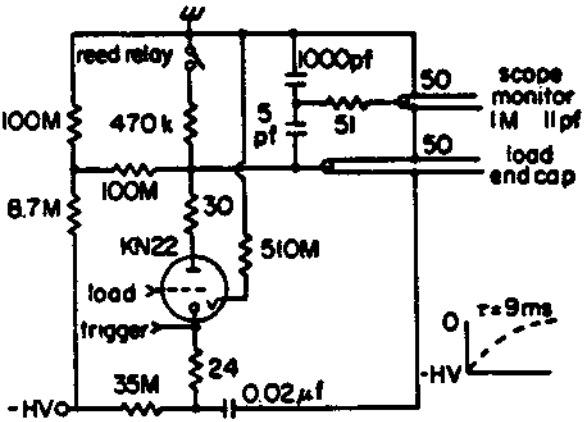

(a) Antiproton load switch

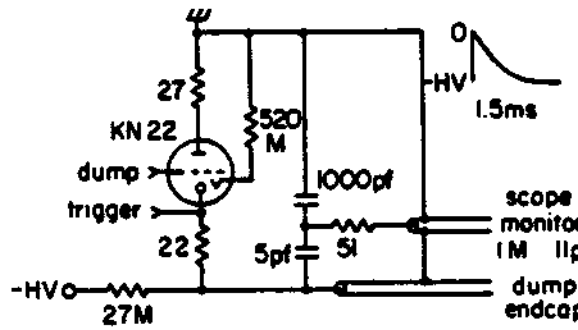

(b) Antiproton dump pulser

Figure 4.2: Circuit used to capture antiprotons in flight.

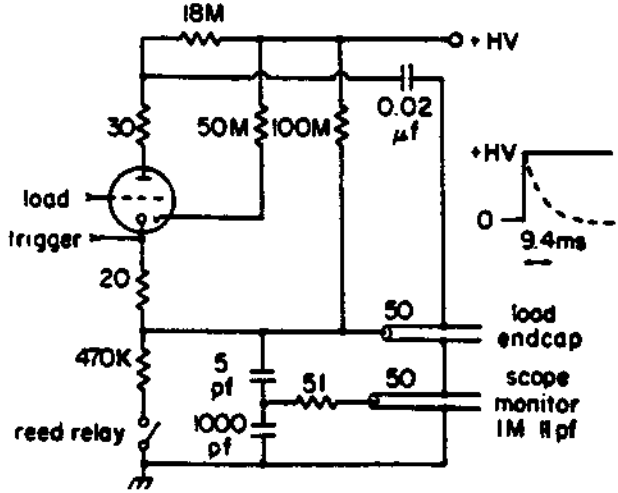

(a) Proton load switch

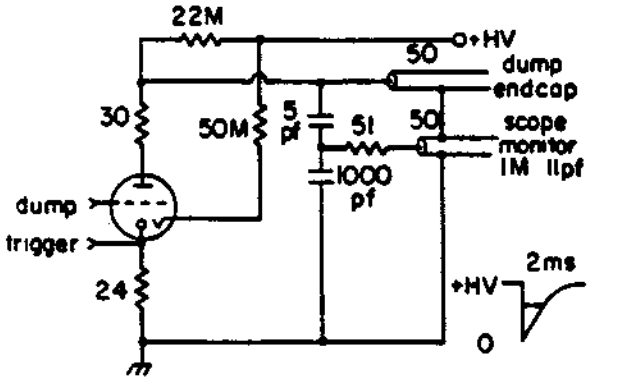

(b) Proton dump pulser

Figure 4.3: Circuit used to capture protons in flight.

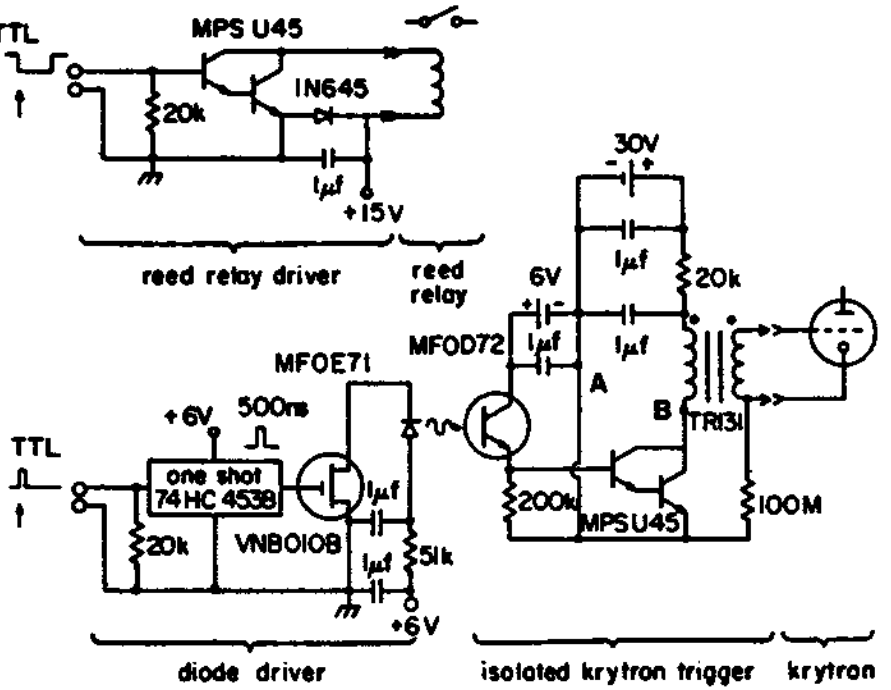

Figure 4.4: Driver circuit for the reed relay and the isolated krytron trigger circuit. The optical coupling is actually through an optical fiber. There is a misprint in Fig. 4 of the Ref.[53]. The 1 μf capacitor between points A and B does not exist.

Chapter 5

Slowing and cooling of stored antiprotons in an ion trap

The task of slowing and cooling antiprotons 6 orders of magnitude in energy within an ion trap, from keV to meV, is accomplished by electron cooling which was first proposed in Ref. [4,61]. Electrons preloaded in a harmonic potential well cool via synchrotron radiation with a time constant 0.1 sec to thermal equilibrium at 4.2 K (corresponding kT = 0.36 meV). Antiprotons repeatedly pass through the electron cloud and collide with electrons until they fall into the harmonic potential well where the electrons reside. Within the well, antiprotons continue dissipating energies to electrons until thermal equilibrium is achieved between the antiproton and the electron clouds. Since the difference in the centrifugal barriers for antiprotons and electrons is approximately 2 K which is less than the thermal temperature 4.2 K, the centrifugal separation should not be a problem. This is the first demonstration of electron cooling in an ion trap. Since electron cooling is a nonresonant process, it can cool and slow antiprotons in a wide energy range without bandwidth limitation in contrast to resistor cooling and stochastic cooling. The cooling time of the order of seconds is much faster than any other technique [62]. Electron-antiproton collisions in the ion trap do not cause annihilations. Once antiprotons are confined in the harmonic potential well, resistor damping can be

also effective but slower than electron cooling. General discussions on the other antiproton cooling mechanisms can be found in Ref.[62].

5.1 Theory of electron cooling

In the degrader, antiprotons colliding with bound electrons cause dramatic energy loss as demonstrated in Chapter 2 where most of the 5.9 MeV antiproton kinetic energy is quickly transferred to the excitation and ionization energy of the initially bound electrons. In a metal target such as Al, the electron density is as high as $7.8\times10^{23}/cm^3$. A 5.9 MeV antiproton stops in Al in less than 20 ps at depth of about 0.25 mm. Collisions with a dense electron cloud confined in an ion trap would similarly slow antiprotons, but less rapidly.

A study of two species plasma (for example, an electron-proton gas) approaching thermodynamic equilibrium via collisions [63] was applied to an ion trap [62]. It is similar in some respects to the cooling of energetic particle beams using a collinear electron beam matched in velocity [64] and to the sympathetic cooling of one ion species by another in an ion trap [65]. If we assume electrons and protons both have Maxwellian velocity distributions, but with different kinetic temperatures T_e and T_p, the proton temperature will evolve with the following rate equation:

$$dT_p/dt = -(T_p - T_e)/t_c \tag{5.1}$$

where t_c, the time constant for equilibration of the temperatures, is given by

$$t_c = [3m_p mc^3/8(2\pi)^{1/2}n_e e^4 L][(kT_p/m_p c^2) + (kT_e/mc^2)]^{3/2}. \tag{5.2}$$

Values of L for an electron-proton gas are given in Ref.[63]. However, there are only a finite number of electrons in the trap and T_e is not a constant. An additional

rate equation for T_e is given [62]

$$dT_e/dt = [N_p(T_p - T_e)/N_e t_c] - (T_e - 4.2)/t_e \qquad (5.3)$$

where N_p and N_e are the total number of protons and electrons sharing the same volume, and t_e is the time constant for electrons energy loss due to synchrotron radiation and resistor damping. The rate equations were solved numerically for an electron density of $10^7/cm^3$, $t_e = 0.1$ sec, and an initial proton energy of 1 keV. The electron cooling times are of order 1 sec for different ratios of electrons and protons, $N_e/N_p = 10^2, 10^3, 10^4$ (Ref. [62]). (Note that we use E = kT/2 while E = kT was used in Ref. [62]).

The experimental conditions differed in several respects. The electron density is approximately $10^8/cm^3$. For the duty cycle D = 1, Fig. 5.1(a) shows the electron cooling processes for different ratios (10, 10^2, 10^3) of electrons to protons. The duty cycle that antiprotons interact with the electron cloud is about 3%, which causes the electron cooling time much longer. The t_c in Eqs. (5.1) and (5.3) should be replaced by t_c/D to include the duty cycle factor. Fig. 5.1(b) shows the electron cooling processes for D = 3%. The cooling time is approximately 11 sec for $D = 3\%$ and $N_e/N_p = 150$ (compared to 2 sec for D = 1). It is obvious that cooling times can not be linearly scaled. This is due to the large increase in the electron temperature, 10 times higher for D = 1 than for D = 0.03, which makes the cooling time longer. The time required to cool antiprotons from 1 keV to 100 K is plotted (Fig. 5.2) versus the electron density. There is an obvious inverse dependence on electron density for D = 0.03. This is less obvious for D = 1 due to the large increase in the electron temperature.

The calculation here and in Ref. [62] do not include the strong magnetic field used in the experiments. The calculation of electron cooling seems also valid for the presence of a strong magnetic field under the assumption that the axial and

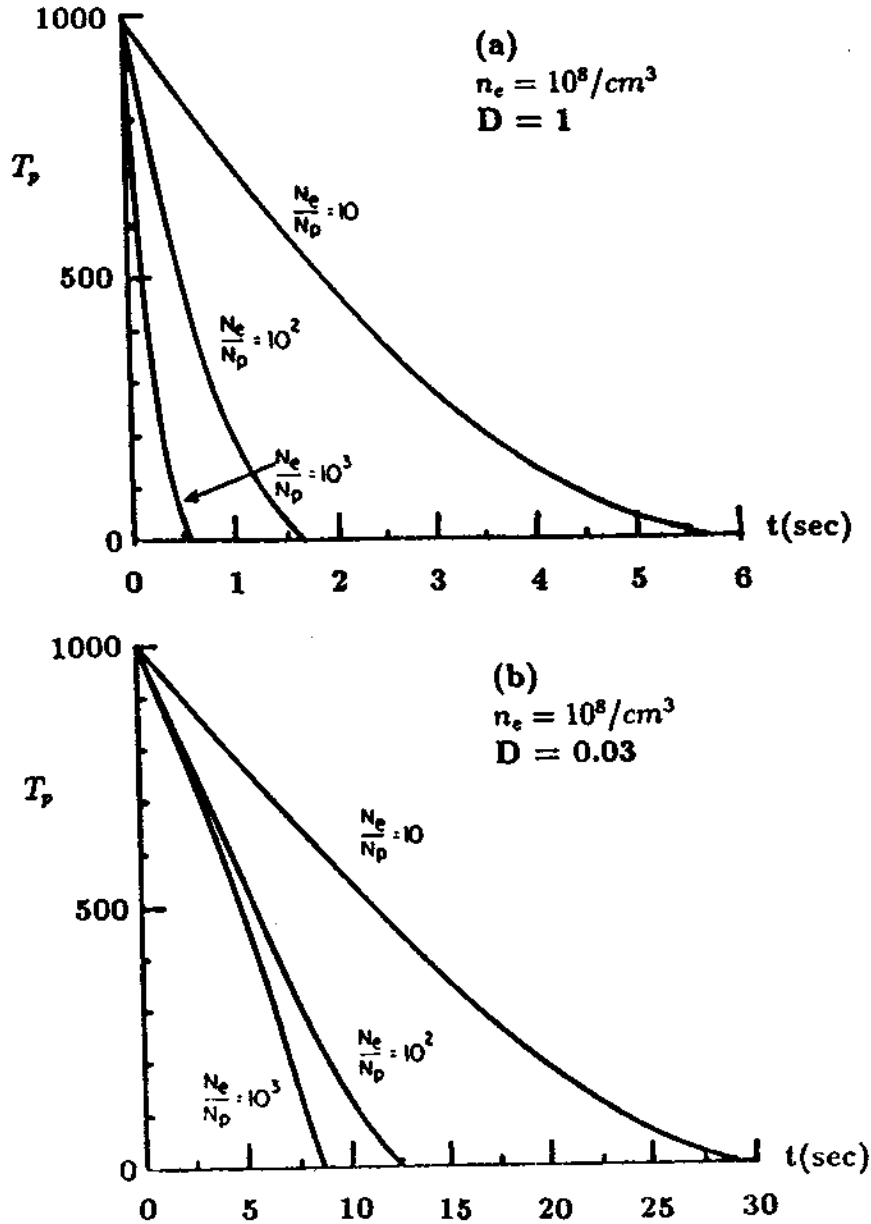

Figure 5.1: Calculation of the electron cooling processes for duty factor D = 1 (a) and 0.03 (b). The curves are calculated for different ratios of electrons to protons, as labeled.

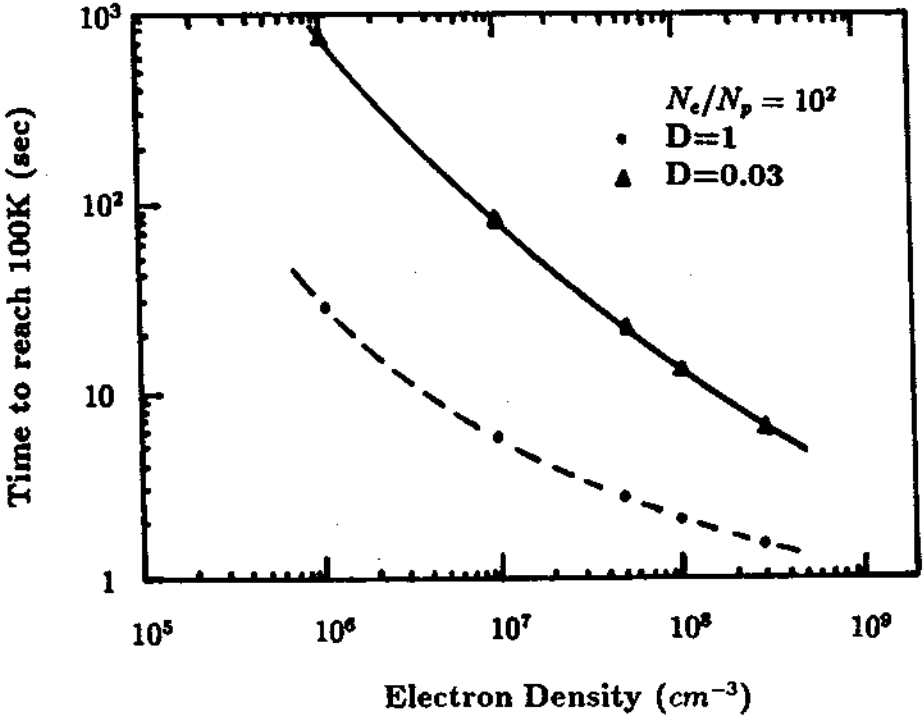

Figure 5.2: Electron cooling time versus electron density. The curves are included to aid the eye.

radial electron temperatures are equilibrated in the trap.

5.2 Experimental setup for antiproton slowing and cooling studies

The experimental setup for antiproton slowing and cooling studies is in Fig. 5.3. A field emission point (FEP) providing a primary electron beam in the trap is mounted above the upper cylinder. A series of rings form a long (13 cm) cylindrical trap which is shorter than the trap used in the antiproton trapping experiment (see Fig. 3.10) due to the relocation of the field emission point. Endcap electrodes can be at high negative potential for holding antiprotons within or at low positive potential so that antiprotons may escape and annihilate. The RCL circuit and FET amplifier on the upper compensation electrode detect a signal which is related to the number of electrons [66] when electrons are loaded in the harmonic potential well. To vary the well depth in the harmonic potential region or change its sign, we can expel the antiprotons and the electrons out. An antiproton annihilation detection system similar to the measurement of HV ramp antiproton energy spectrum (Chapter 3) is used.

5.2.1 Cylindrical open-endcap ion trap and ion motions

The cylindrical open-endcap ion trap is used for trapping electrons which are counted and monitored by RF techniques. It consists of a ring, two compensation and two open-ended endcap electrodes as shown in Fig. 5.4. The detailed calculation of its electrostatics is in Ref. [54]. The radius of the cylinder is $\rho_0 = 0.600$ cm. The length of the compensation electrode is $z_c = 0.489$ cm. The length from center of the ring to the edge of the endcap is $z_0 = 0.586$ cm. Gaps between the electrodes

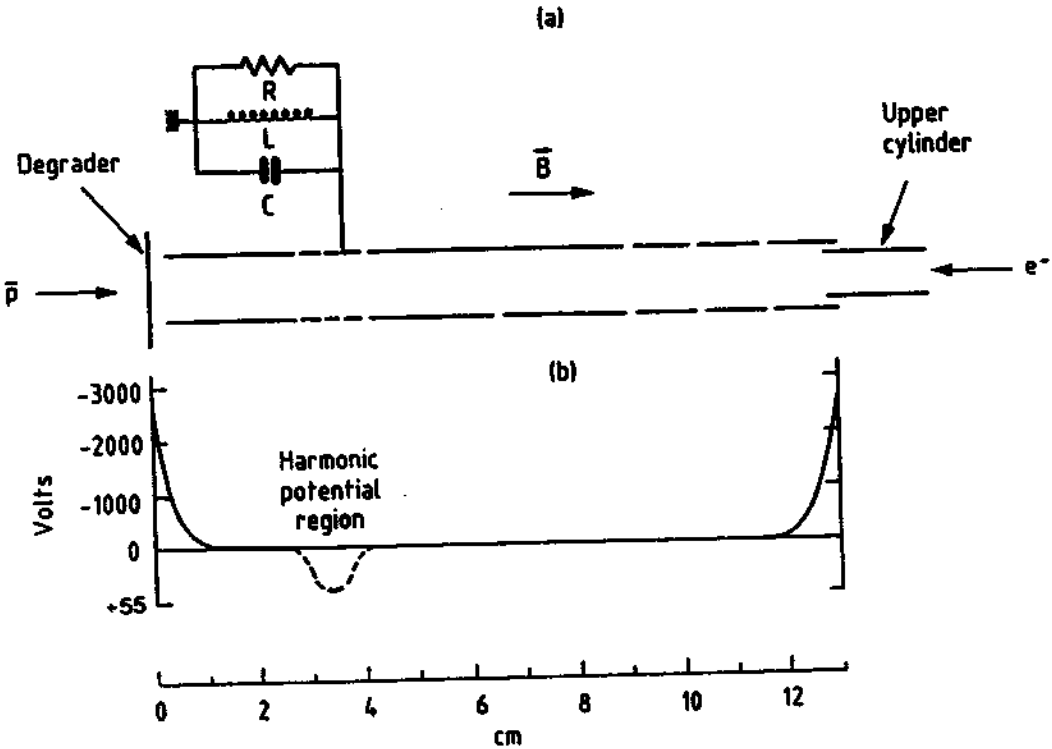

Figure 5.3: Experimental setup for antiproton slowing and cooling studies.

are 0.018 cm. The ring is at V_0 potential and the compensation potential V_c =0.88 V_0. The endcaps are grounded.

The electric potential V near the center of an ion trap can be expanded in Legendre polynomials,

$$V = (-V_0/2)\sum_{k=0}^{\infty} C_k(r/d)^k P_k(cos\theta) \tag{5.4}$$

where d is the characteristic length defined as $d^2 = (z_0^2 + \rho_0^2/2)/2$. All $C_{k=odd} = 0$ due to reflection symmetry across the z = 0 plane. Terms with $C_{k=even}$ depend on compensation potential V_c and trap geometry. C_0 represents the trap DC potential. The next lowest-order term, C_2 term, gives the needed harmonic quadrupole potential for axial confinement,

$$V_{C2} = -V_0 C_2 r^2 P_2(cos\theta)/(2d^2) = -V_0 C_2(z^2 - \rho^2/2)/(2d^2) \tag{5.5}$$

The trap used for precision mass measurement has $C_2 = 0.5449$, and d = 0.512 cm. The potential energy for an antiproton of charge q = −e is

$$U(z,\rho) = qV = eV_0 C_2(z^2 - \rho^2/2)/2d^2 = (1.04z^2 - 0.52\rho^2) \times 10^{-2} eV_0 \tag{5.6}$$

where z and ρ are in mm. For a single particle, its axial energy depends on axial position in a simple form $E = z^2 eV_0 \times 10^{-2}$. For example, the particle axial energy is 0.7 eV if its amplitude is 1 mm when the potential on the ring is 70 V. A particle will experience a harmonic well in axial direction while sitting on a potential hill in the radial direction. The corresponding axial frequency is given by

$$\omega_z^2 = C_2 eV_0/(md^2). \tag{5.7}$$

Existing higher order terms represent anharmonicity and they should be eliminated. As long as the particles are not far from the center of the trap, higher order terms diminish as k becomes larger. By adjusting the compensation potential, the anharmonic C_4 term can be tuned out to zero. A special choice of trap radius

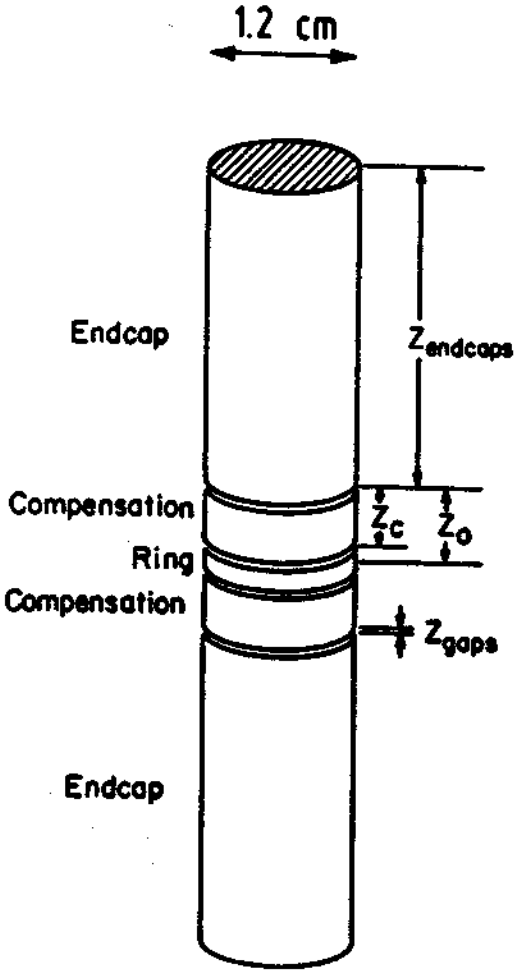

Figure 5.4: The cylindrical open-endcap ion trap (From Ref. [54]).

ρ_0/z_0 can minimize the axial frequency (or C_2) dependency on the compensation adjustment. In the ideal case, C_2 is independent of V_c and the trap with this feature is called an orthogonalized trap [67]. The higher order anharmonic C_6 term can also be eliminated in principle at $z_c/z_0 \approx 0.835$. In practice, a nonzero C_6 is expected due to the machining imperfections. Consequently, a harmonic potential can be realized in the center of the cylindrical compensated orthogonalized ion trap with open-ended endcap electrodes. The deviations from a harmonic potential due to trap machining and construction are unavoidable and their effects upon our precision measurement must be taken into account. The real trap used here is more complicated. The ring electrode is split into 4 identical segments and each compensation electrode is cut into 2 pieces along the z axis allowing various RF drives and detections to control and monitor the particles.

A particle of charge e and mass m is confined in a harmonic ion trap (i.e. a Penning trap) by applying a uniform magnetostatic field B parallel to the z axis for radial confinement and an electrostatic quadrapole potential for axial confinement. The electric potential that is a function of the cylindrical coordinates z and ρ is given by the Equation (5.5). The particle will harmonically oscillate along the z axis due to the axial electric field and travels in a circular cyclotron motion with frequency ω_c = eB/mc. However, this cyclotron motion is slightly modified by the repulsive radial component of the electric field. The modification results in an additional magnetron motion characterized by frequency ω_m (see Fig. 5.5). The particle motion is described by the relation:

$$z(t) = A_z cos(\omega_z t + \theta_z), \tag{5.8}$$

and

$$x(t) + iy(t) = |\mathbf{r}_m| e^{-i(\omega_m t + \theta_m)} + |\mathbf{r}_c| e^{-i(\omega_c' t + \theta_c)}, \tag{5.9}$$

where $\omega_z = \sqrt{C_2 e V_0 / m d^2}$, is the axial frequency, and

$$\omega_m = \omega_c/2 - \sqrt{(\omega_c^2/4) - (\omega_z^2/2)} \tag{5.10}$$

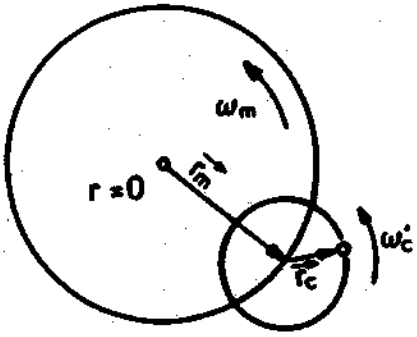

Figure 5.5: An antiproton radial motions in an ion trap (from Ref. [68]).

is the magnetron frequency, and

$$\omega_c' = \omega_c/2 + \sqrt{(\omega_c^2/4) - (\omega_z^2/2)} \tag{5.11}$$

is the modified cyclotron frequency. Then the cyclotron frequency is given as

$$\omega_c = \omega_c' + \omega_m, \tag{5.12}$$

where $\omega_m = \omega_z^2/2\omega_c'$. The center-of-mass motions for a cloud of ions are characterized by the same three frequencies and they are directly detected by our detection system discussed in the next section.

5.2.2 Preamplifier for the detection of ions and resistor damping

RF preamplifiers for particle resonant detection at a frequency range from 1 to 90 MHz, working at LHe temperature in 6 T field, are constructed. A GaAs field effect transistor (FET) MGF1100 (Mitsubichi Electronic) dual-gate n-channel Schottky gate type, is used. The dual gate configuration minimizes the Miller effect, an undesirable feedback between input and output of the FET that can degrade the high frequency performance of the device [69]. The electronic circuit is shown in Fig. 5.6. The first gate (G1) and the second gate (G2) of the FET are DC biased with RC filters. The source (S) is grounded and the drain (D) is biased at V_d. The signal from the RCL circuit goes to G1, then is amplified and goes through an impedance matching π-network to the next stage which has an input impedance of 50 Ω. The power gain is approximately 10^3 while the voltage gain is around one. The FET drain current is operated around 1 mA to keep the LHe boil-off low. Heat transferred to the liquid helium bath is 3 mW for $V_d = 3$ volts.

The amplifier is enclosed in a cylindrical copper cavity, 3.6 cm in diameter and 8.6 cm tall. A copper plate and a PC board with copper cladding on both sides

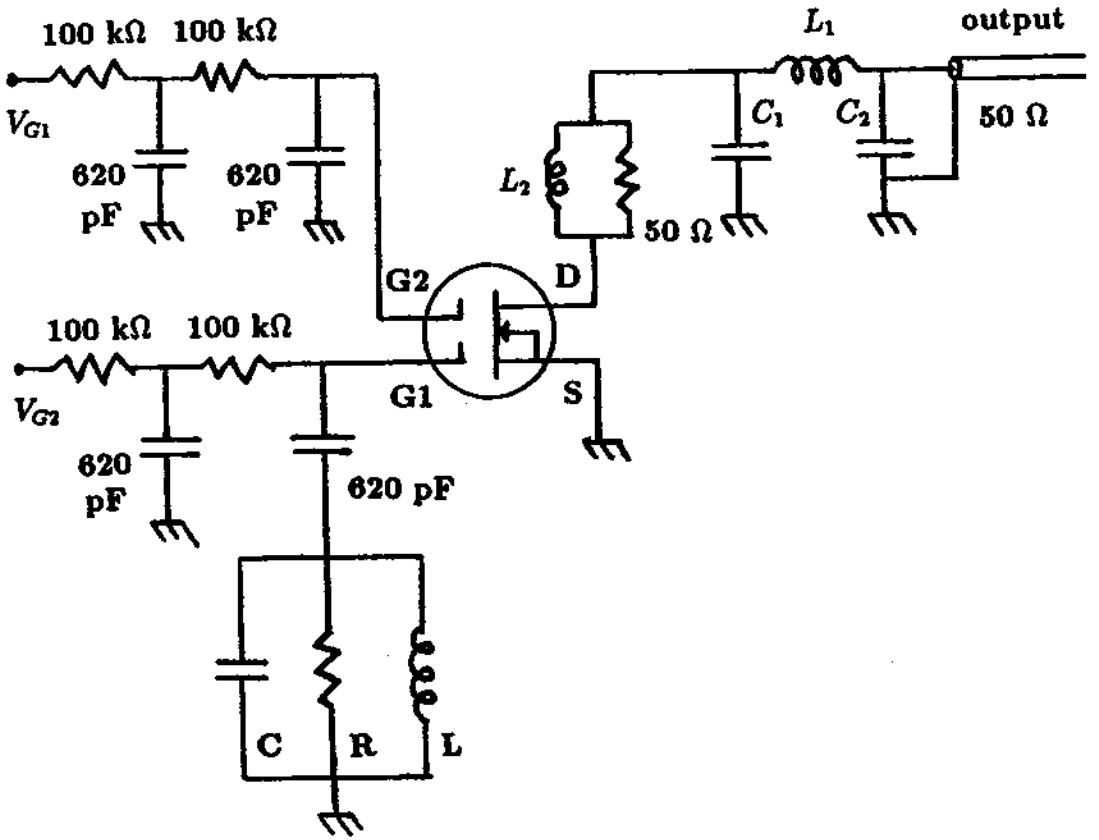

Figure 5.6: Dual-gate GaAs FET amplifier circuit.

separates it into two parts. The upper section (3.3 cm high) has the FET circuit in a vertical square PC board (3 cm× 3 cm). The cylindrical cavity below is 5 cm high with a diameter of 3.6 cm. It forms a resonator when it contains an inductor which can tune away the trap capacitance at the desired resonance frequency to achieve a pure resistive impedance. Helical resonators are discussed in Ref. [70,71]. A helical resonator for frequency at 30 to 90 MHz consists of 6 to 3 turns of silver plated copper wire with diameter of about 2 mm. For low frequencies, 1 to 3 MHz, the inductor wires are enamelled wire with more than 100 turns. The capacitance C in Fig. 5.6 includes the effective distributed capacitance, the capacitance of the feedthrough, and the contribution from the trap electrodes. The resistive loss in the LC circuit is inversely proportional to an effective resistance R in parallel with the LC at the resonant frequency. It is desirable to keep the distributed capacitance to a minimum and to keep the inductance high for best performance.

The Johnson noise RMS voltage for a resistor R at temperature T is, $V_{RMS} = \sqrt{4kRTB}$, where B is the bandwidth, and k is the Boltzmann constant. We use Q, the quality factor of the parallel-resonant circuit, as a measure of resistive loss. Q value is

$$Q = f/\Delta f, \tag{5.13}$$

where f is the center frequency of the noise resonance, and Δf is the FWHM of noise signal in power, or half-power bandwidth, which corresponds to a width at 70% of the amplitude in RMS voltage scale. The peak of RMS voltage across the LCR circuit corresponds to the Johnson noise. A noise resonance at 68 MHz, for a FET preamplifier at LHe temperature, is shown in Fig. 5.7(a). It has a Q value of 500. The relations of Q with R, C, and L can be expressed as:

$$Q = R/\omega L = RC\omega \tag{5.14}$$

The higher the Q of the circuit, the higher the parallel impedance R at the resonant frequency.

As the particle oscillates in the trap axially and radially the image current I_{ind} flows and dissipate energy through a resistor R between an electrode and ground. The potential signal $V_s = I_{ind}R$ can be detected by a preamplifier. The induced current by axial motion, observable in the compensation electrode, is $I_z = k_z e\omega_z z/2z_0$, where k_z is a constant of order one related to the trap geometry,z is the amplitude of the particle axial oscillation. For the trap we are using, k_z is calculated to be 0.8994 [54]. It is smaller (0.3346) when the detection is the from the endcap electrode.

Since the circular motion can be viewed as two superimposed harmonic oscillators, an induced current on one segment of the ring electrode is in similar form $I_c = k_c e\omega_c \rho_c/2\rho_0$. For a fixed geometry and motion frequencies, it is understandable that a large amplitude of oscillation would bring a large signal. In reality, because capacitance exists between each pair of electrodes, a pure resistance can only be achieved when an inductor tunes away the capacitance at a certain resonant frequency. The kinetic energy of the particle coupled to the resistor decreases until the particle is in thermal equilibrium. The power is dissipated in the resistor generating heat. As an example for axial motion, energy loss in the effective resistance R damps the particle motion with a damping time constant given by [72]

$$\tau = (m/R)(2z_0/ek_z)^2 \tag{5.15}$$

where e and m are the charge and mass of the particle. Because the time constant is proportional to the mass, resistor damping is 3 orders of magnitude more effective for an electron than for a antiproton when other conditions are equal. For a typical value of R = $10^5\Omega$, the time constant for an electron is approximately 0.1 sec while it is 100 sec for an antiproton. The cooling of a cloud of particles can not be faster than a single one due to internal degrees of freedom of the axial and cyclotron motion [62].

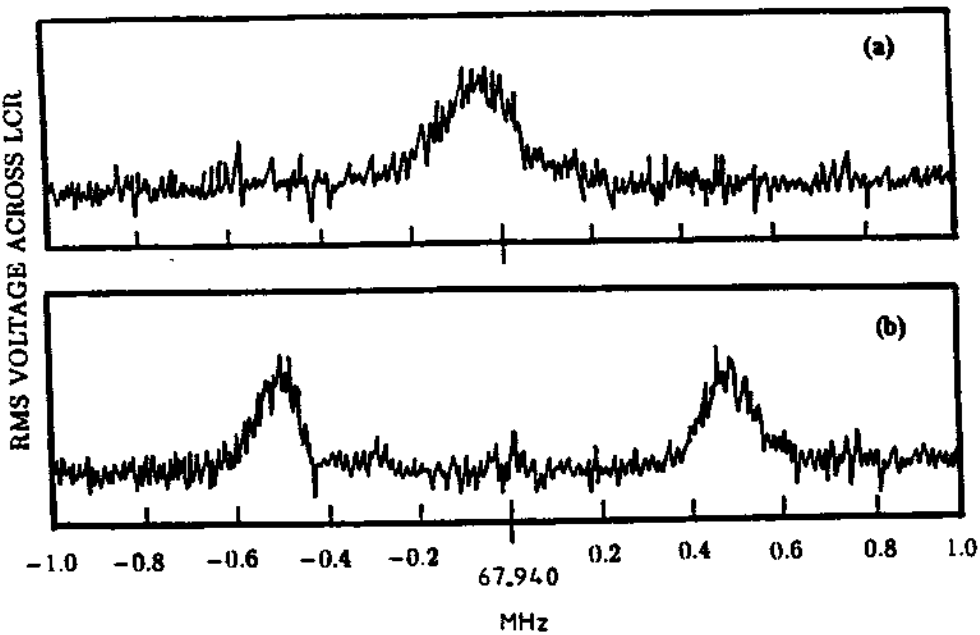

Figure 5.7: (a) Typical noise resonance for the LCR circuit at LHe temperature. (b) Modified signal when large electron cloud is present. The spacing of the two peaks of 1 MHz indicates that 6×10^6 electrons are in the trap.

The effective radio-frequency circuit used to damp and detect the ion motion can be represented as shown [73] in Fig. 5.8. An oscillating particle with charge e induces a current I through the resistor R when an inductor is used to tune out the trap capacitance. V_n is the Johnson noise from the resistor which is proportional to the square root of R, $\sqrt{R}$. V_s is the input voltage signal detected by a preamplifier. The particle motion can be driven by the oscillatory potential V_D continuously or just for a short period then switched off. The Johnson noise is "shorted out" on resonance [66].

The number of electrons can be counted from axial detection [66]. The linewidth of a single particle is given by $\Delta f_1 = 1/(2\pi\tau)$. The noise from the center of the spectrum is shorted for particles oscillating at the frequency $f = 1/2\pi\sqrt{LC}$ in the trap. Two resonant peaks are formed as in Fig. 5.7(b) for large numbers of electrons when the width between two peaks $\Delta f_N >> \Delta f$, the width of the noise resonance. The position of the peaks corresponds to the parallel resonances formed when the reactive impedance of the electrons is equal and opposite to the reactive impedance of the external tank circuit [66]. In this case the numbers of electrons is given by

$$N = (\Delta f_N)^2/(\Delta f_1)(\Delta f). \tag{5.16}$$

In Fig. 5.7(b), the numbers of electrons N is approximately 6×10^6 for $\Delta f_N \approx 1$ MHz, $\Delta f_1 \approx 1.2$ Hz, and $\Delta f \approx 135$ kHz. The electron density will be discussed in section 5.3.

5.2.3 Selectively ejecting electrons and antiprotons

The trapping potential is switched from V_0 to a low voltage between 0 to 4 V in approximately 5 ms and stays there for approximately 0.6 sec, then goes

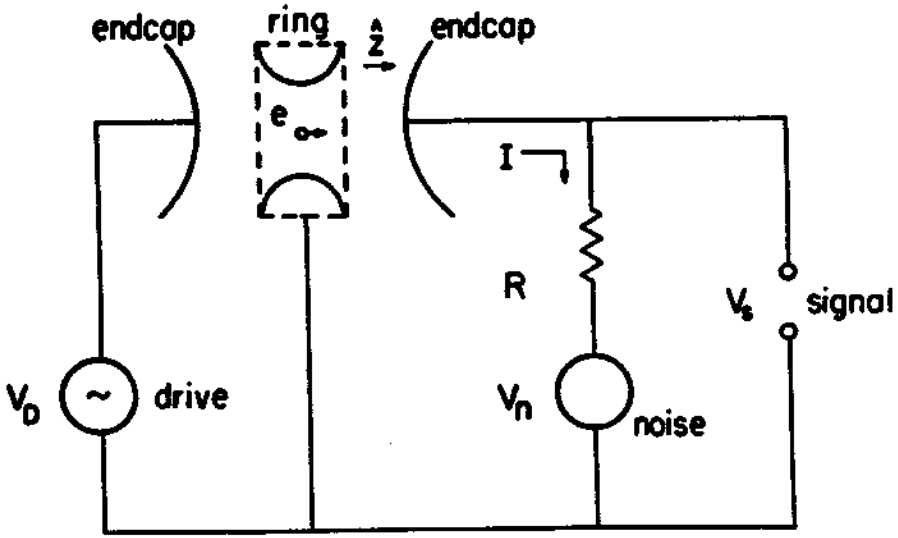

Figure 5.8: Detection and resistor damping of ion motion (from Ref. [73]).

back to the initial potential. This is a called potential dip. The ratio of electron number to antiproton number can be changed by the dip process combined with RF drive on the electron frequencies ν_z and $\nu_z + \nu_m$. The low voltage linear ramp can eject the trapped particles and the antiproton number can be measured by this destructive method. The low voltage dip/ramp circuit is shown in Fig. 5.9(a). When the TTL signal controlled relay switch S_1 is at position A and C, the normal ring potential V_0 and the compensation potential V_c are applied to the trap. The TTL signal controlled relay switch S_2 can be chosen to connect the dip potential V_{dip} or the ramp potential V_{ramp}. When S_1 is switched to position B and D, the V_{dip} is applied to the trap electrodes. If S_2 is also switched from position F to E when S_1 is switching, the low voltage ramp is applied to the trap electrodes. After 0.6 sec, the trap potentials are back to V_0 and V_c when S_1 is reset to position A and C. The resistors are used to keep $V_c = 0.88V_0$ for the harmonic potential well. A typical potential dip waveform on the ring electrode is shown in Fig. 5.9(b). A typical potential ramp waveform on the ring electrode is shown in Fig. 5.9(c). The ring potential V_0 first drops to 10 V, then ramps down to below -5 V in 560 ms with a linear ramp rate of 30.3 mV/ms. The potential well depth (at the center of the trap) has a ramp rate of 23.5 meV/ms.

Just like the detection system for the HV ramp in the long trap described in Chapter 3, another identical multiscaler is triggered and starts counting the antiproton annihilations when the harmonic potential well changes. Particles with energies exceeding the well leak out and their annihilations are detected as an energy spectrum. As an example, Fig. 5.10 shows the energy spectrum of antiprotons released from the harmonic trap with a linear ramp. It has 190 counts of antiproton annihilations (representing 400 antiprotons) and a width of 5 meV. Actually the width is approximately equal to the time resolution of 1 channel per 0.2 ms in the Joerger multiscaler.

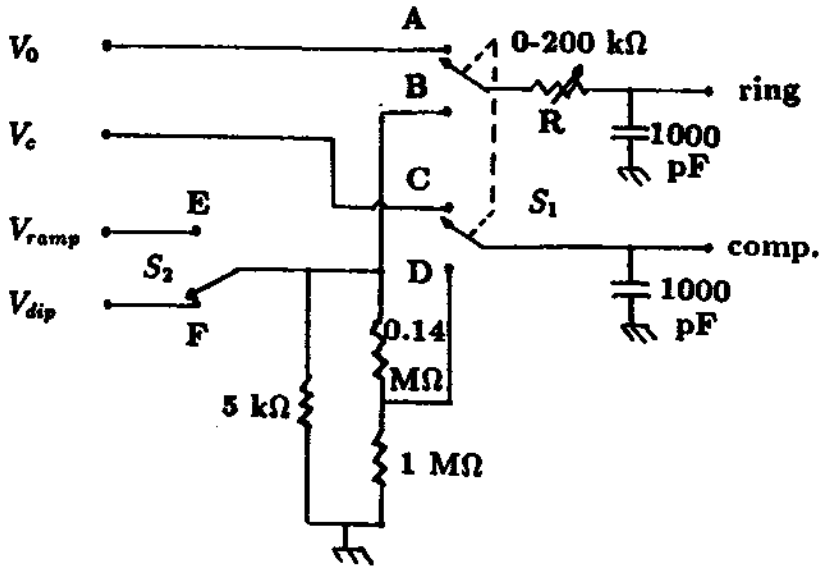

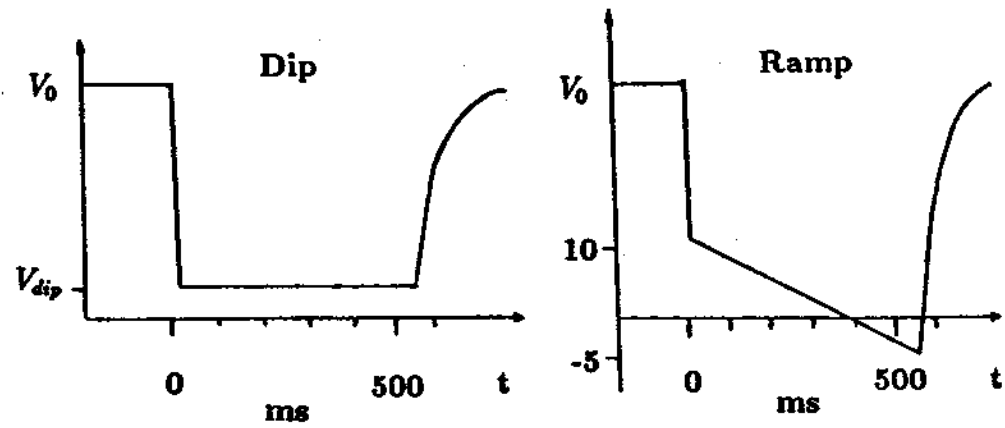

Figure 5.9: Low voltage dip/ramp circuit and its waveforms.

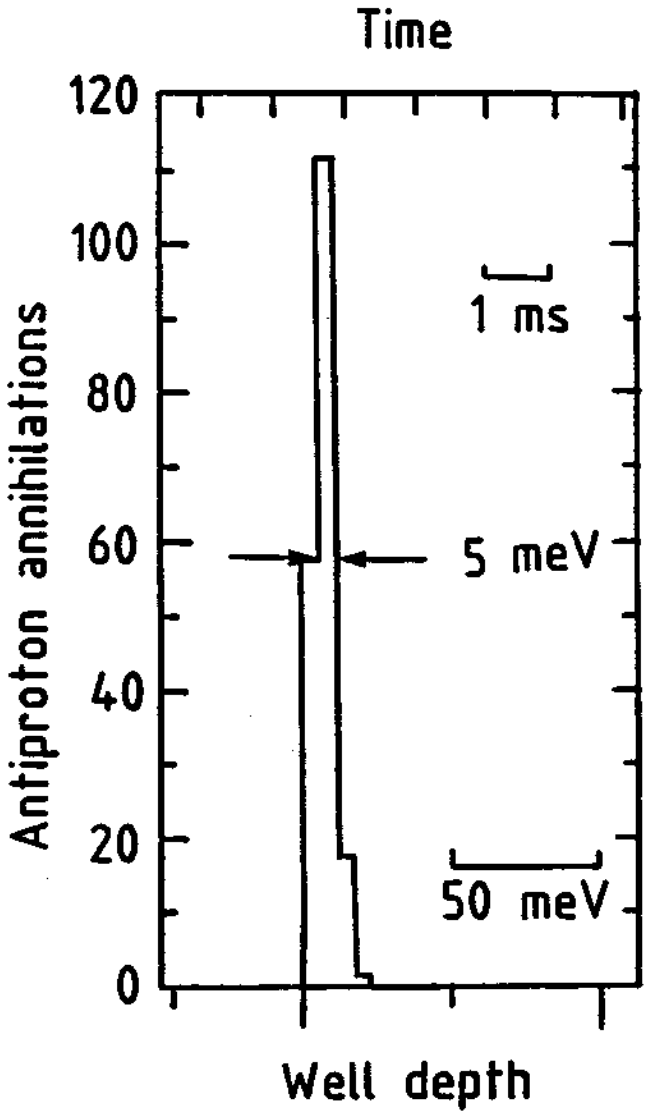

Figure 5.10: Antiproton energy spectrum after particles are ramped out from harmonic well.

5.3 Electron cooling studies

A large and dense electron cloud is needed for rapid cooling and slowing of the antiprotons. A beam of energetic electrons from the field-emission point strikes the degrader and causes the release and later the ionization of neutral atoms. The stripped electrons as well as the secondary electrons emitted directly from the degrader surface are confined in the harmonic potential well. The electron density can be estimated in a simple model where the electron cloud forms a sphere and the Coulomb repulsion balances the axial electrostatic field. In the harmonic trap used here, this gives an electron density $n_e \approx 3.5 \times 10^6 V_0/cm^3$. It is $10^8/cm^3$ for the applied potential $V_0 = 30$ V. The diameter for a cloud of 6×10^6 electrons given by this simple model is approximately 0.5 cm.

The electron cloud is an unneutralized electron plasma. Its Debye length is 1.4×10^{-3} cm which is much smaller than the cloud size. The electron plasma frequency is 92 MHz for $V_0 = 30$ V (it is 140 MHz at 70 V). The parameter $\Gamma = e^2/akT = 0.2$ (a = 2×10^{-3} cm is the particle spacing) is much smaller than 2 which is required to form a liquid plasma [74].

5.3.1 Antiproton-electron collisions and energy loss

Antiprotons moving through the cold electron cloud lose energy by antiproton-electron collisions. Eventually, the antiprotons fall into the harmonic potential well and form a new bound state after their initial kinetic energies are transferred to the electrons. We denote N_h as the number of hot antiprotons remaining in the long trap. The number of cooled antiprotons N_c which fall into the harmonic well by electron cooling is measured by decreasing the potential of the harmonic well crossing 0 V as shown in Fig. 5.9. The total number of trapped antiprotons is $N = N_h + N_c$ (on the order of 10^4). Fig. 5.11 shows the fraction of hot antiprotons

(N_h/N) and cold antiprotons (N_c/N) versus the cooling time. The time allowing hot antiprotons colliding with cold electrons is increasing, the hot fraction is getting smaller while the cold fraction larger. There are 4×10^6 electrons (the width of the clouds is 0.8 MHz) in the center of the harmonic trap covering a large fraction of the diameter of the trap so that nearly 100% of the antiprotons are cooled into the harmonic well for cooling times exceeding 100 seconds. Generally, the scattering of the points are small. The observed fluctuations are larger if we normalize to the initial PPAC signals which are proportional to the number of antiprotons delivered by LEAR. This is due to the missteering of the beam since the PPAC signals are not exactly proportional to the total numbers of trapped antiprotons under such condition.

The fraction of antiprotons cooling into the harmonic potential well for various numbers of electrons in the trap versus cooling time is shown in Fig. 5.12. The curves are included to aid the eye. Up to 95% of the antiprotons trapped in the long trap fall into the harmonic well after 100 sec. The time constant for the cooling process is about 10 sec when 4×10^6 electrons are preloaded in the ion trap, which is in good agreement with our estimate in Sec. 5.1. Thus a rapid cooling and slowing of antiprotons are achieved. As the number of electrons is reduced, electron cooling is less effective because the interaction region with antiprotons are smaller. Many factors limit a more quantitative comparison with Spitzer's theory. Beside the magnetic field mentioned in Sec. 5.1, there may be a difference between electron-proton collisions and electron-antiproton collisions since we have observed such difference in the proton and antiproton range measurements (see Section 2.5). Energies in radial motion are not measured here. Electrons heated by antiprotons with axial energy above 3 keV (antiprotons which are not trapped) contribute a larger electron temperature and a longer cooling time. The particle distribution for both electrons and antiprotons is not a Maxwell-Boltzmann distribution.

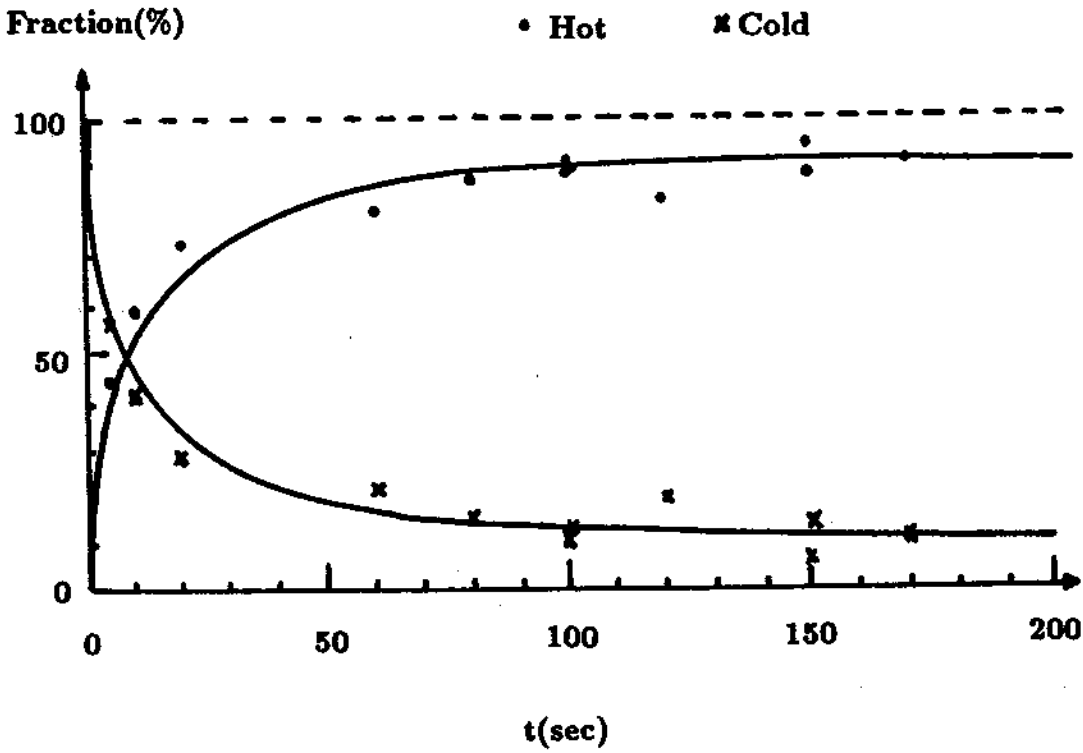

Figure 5.11: Fraction of hot antiprotons and cold antiprotons versus the cooling time. The curves are included to aid the eye.

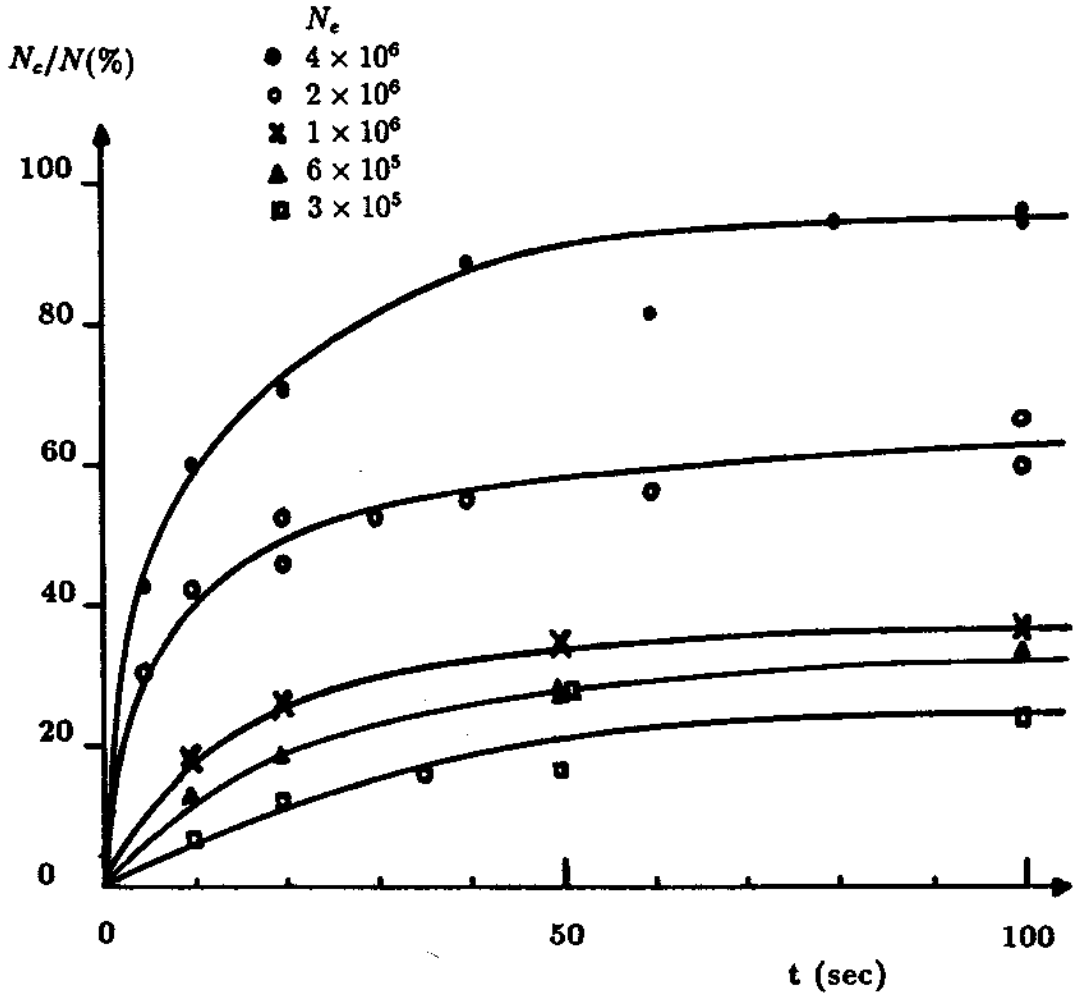

Figure 5.12: Fraction of antiprotons falling into the harmonic potential well for different numbers of electrons in the trap versus cooling time. The curves are included to aid the eye.

5.3.2 Low energy antiproton ramp spectrum

The width of the low energy antiproton ramp spectrum is due to the space charge of the antiproton cloud. In the trap we use, a crude estimate approximately given by

$$E = 0.069N^{2/3}\ meV. \tag{5.17}$$

In Fig. 5.13, we have three examples of the number of antiprotons detected escaping the harmonic well as a function of the well depth. The well depth is reduced linearly in time at the rates indicated in the insets. Electrons used for cooling are still in the trap (a) and most have been removed for (b). In (c), the number of antiprotons has been reduced as well. It is not surprising to see low energy tails in all the energy spectra because some particles can be very cold. The high energy tail only becomes obvious when large number (millions) of particles are present as seen in (a). In the example (a) where 14,000 antiprotons annihilation counts (or 3×10^4 antiprotons) are detected, the depth of the harmonic well is decreased from 23 eV to below 0 eV at a rate of 23.5 meV/ms, with each channel 1 ms. The zero crossing is hard to locate precisely since stray potentials within the electrodes are expected to shift the well depth by as much as 30 meV. The observed width is 84 meV (the energy width of 66 meV is estimated using Eq. (5.17)). In the example (b), the width is 37 meV for 1.6×10^4 antiprotons (the width of 44 meV is estimated), with each channel 0.2 ms, after most of the electrons are resonantly ejected from the trap. If in addition we reduce the number of antiprotons in the trap to approximately 850 (6 meV is estimated) or 400 (4 meV is expected), the observed width decreases to only 9 meV (Fig. 5.13(c)) or 5 meV (Fig. 5.10). The observed energy width agrees with the Eq. (5.17) very well. Because there is a broad shoulder at left side of the peak in (a), the width can not be compared directly with the spectra without this shoulder. The electron spectrum is not measured.

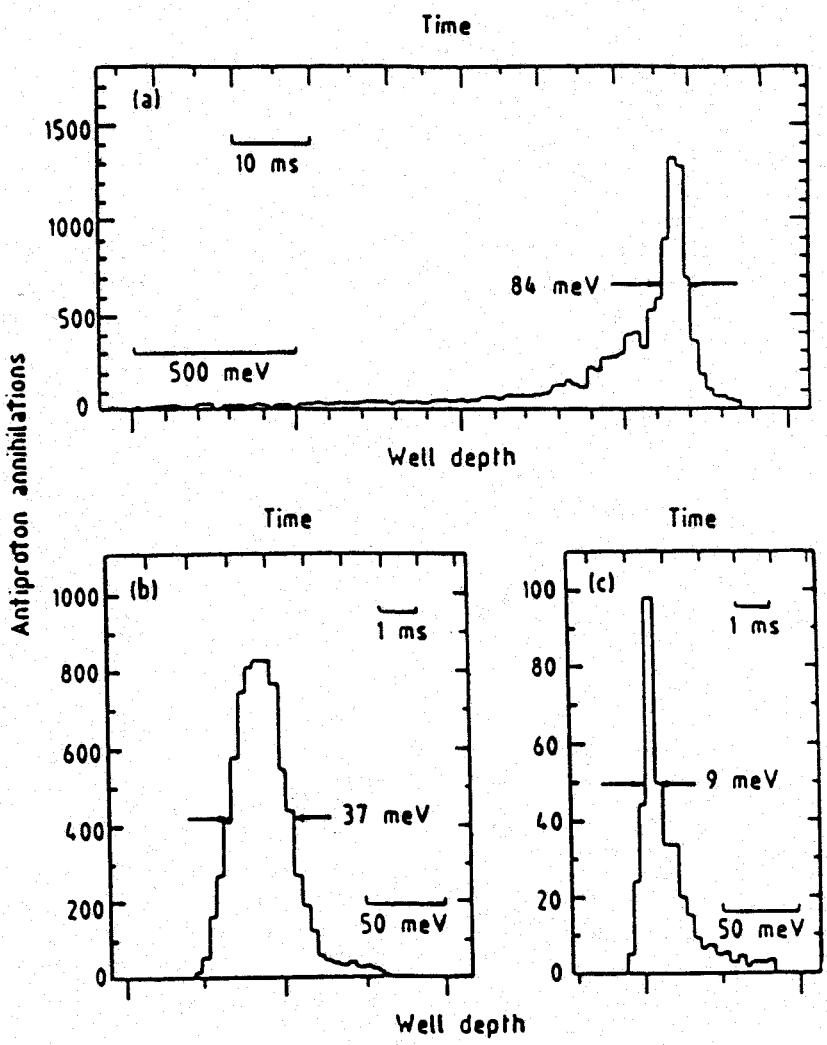

Figure 5.13: Low voltage dump spectrums.

The energy spectrum can change depending on the RF drive strength and frequency (how close it is to resonance) just before antiprotons are dumped. A strong RF drive can make the high energy tail in Fig. 5.13(a) much larger and the particle distribution is also shifted to higher energy. The energy spectrum of a heated antiproton cloud (8500 antiprotons) is shown in Fig. 5.14. Before the antiproton dump, axial and cyclotron signals (the nondestructive resonant method will be discussed in Chapter 7) stay hot for more than 30 minutes after the cyclotron drive was turned off, which is an indication that there are not many electrons in the trap. Comparing Fig. 5.14 and Fig. 5.13(b) shows the effect of the heated antiproton cloud. The dump energy spectrum in Fig. 5.14 shows a large number of hot particles are between 0.1 and 1 eV, that are absent in Fig. 5.13(b). There was no strong drive during the low voltage dump. The particle energy distribution with large high energy tail is due to the heated antiproton cloud in the trap with a large spacial distribution.

5.3.3 Cryogenic antiprotons at 4.2 K

We have discussed that antiprotons could dissipate energy by resistor cooling. As shown in Fig. 5.15, the detected power signal for cyclotron motion which is proportional to the cyclotron motion center-of-mass energy versus time by resistor damping is given. The time constant is about 20 minutes which is much longer than the calculated cyclotron damping time (τ_1) for single particle of 3 minutes, because of the additional time needed for energy transfer from internal motions to the center-of-mass motion for a cloud of antiprotons. If the internal motions are absent, the damping time constant for the center of mass motion for N particles is τ_1/N. When there are some electrons in the trap with antiprotons, the damping time can be much faster ranging from seconds to minutes. The dash line in the figure represents an electron damping curve with a time constant of 1 minute. The

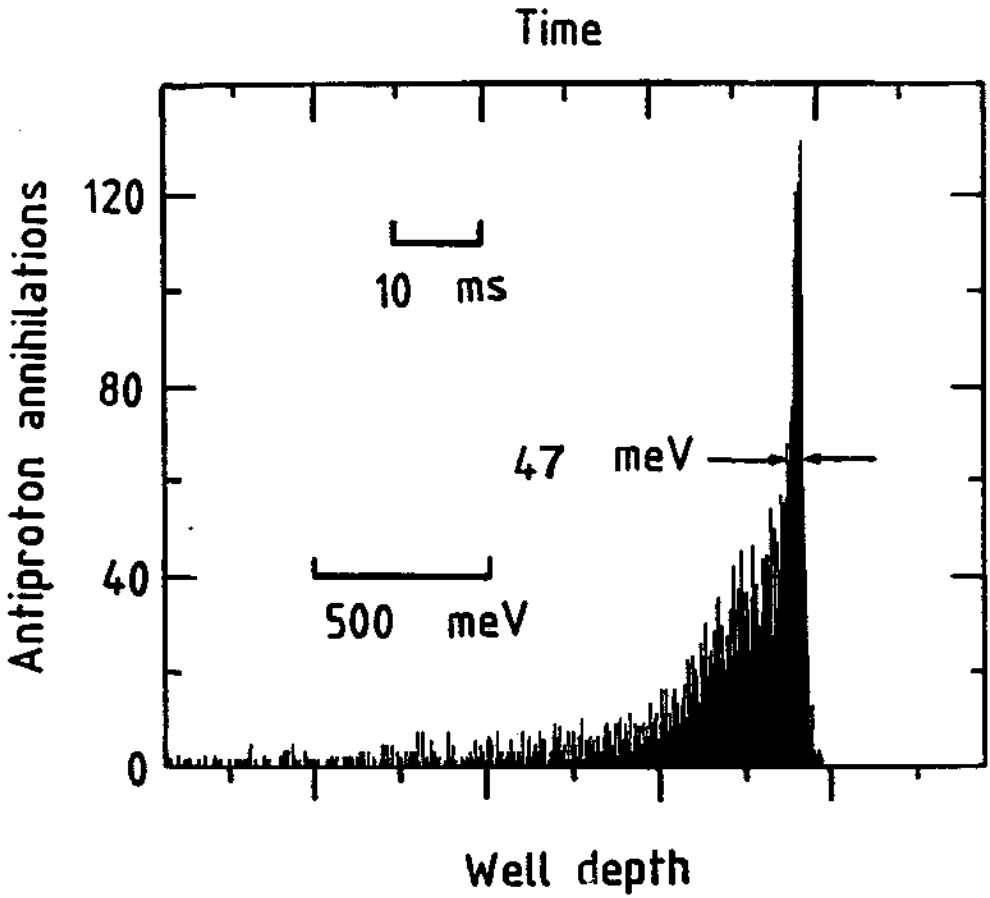

Figure 5.14: The energy spectrum of a heated antiproton cloud.

trap and its vacuum enclosure are cooled down to LHe temperature. The thermal equilibrium temperature is presumably achieved when there is no external heating source. Both damping mechanisms can make antiproton axial motion reach thermal equilibrium. For trapped antiprotons in thermal equilibrium with their surroundings, their thermal energy 3kT/2 is 0.54 meV for T = 4.2 K. Trapping and cooling low energy antiprotons in an ion trap have been demonstrated here. Important applications will be discussed in Chapter 6 and 7.

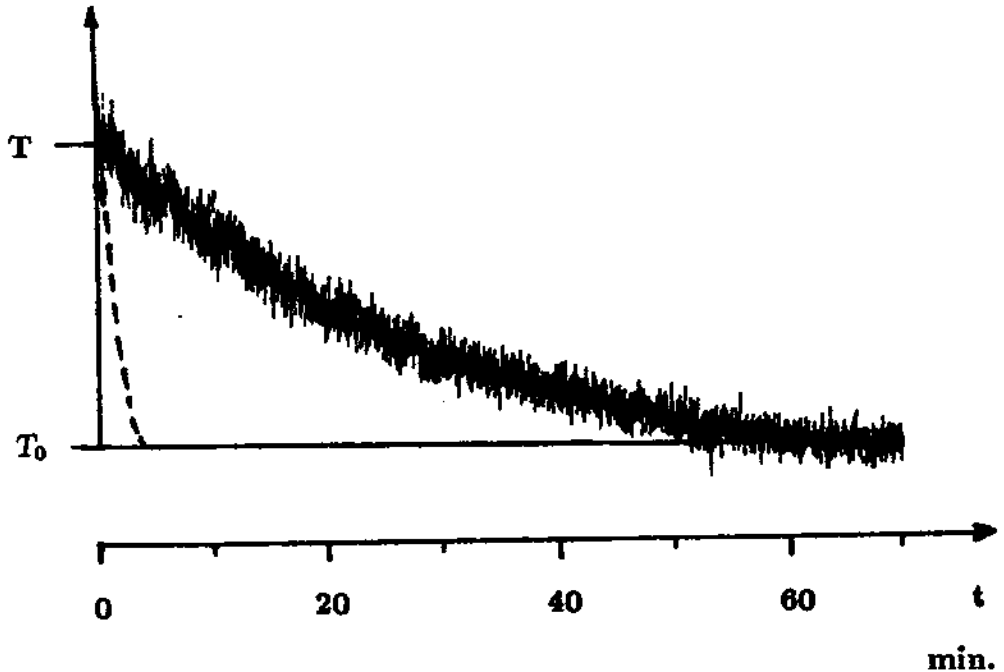

Figure 5.15: Resistor damping the antiproton cyclotron motion. Electron damping is many times faster (dash line).

Chapter 6

Antiproton lifetime and vacuum

6.1 Antiproton lifetime measurement in an ion trap

Our direct antiproton lifetime measurement in an ion trap sets a more stringent antiproton mean life limit than any other direct measurements or any measurements searching for a specific decay mode. It also has important applications in antiproton-gas interaction and as an extreme high vacuum measuring technique. Antiprotons were first trapped in a long trap and then electron-cooled into the harmonic potential well for long time storage after most electrons were ejected as described in Chapter 5. The presence of the antiprotons in the trap was checked daily by non-destructive resonant techniques to see the cyclotron frequency and axial frequency signals so that the magnetic field drift during the 2 months hold time was also monitored. The magnet is persistent when liquid helium in its dewar is sufficient. Batteries were used to hold particles so that the occasional power failures in the experimental area did not result in loss of antiprotons. The battery produced a ring potential of 71.64 V. The battery for compensation electrodes had a potential near 88% V(ring) to keep a harmonic potential well. Actually, the cyclotron frequency was measured when the compensation electrodes were switched

to the power supply capable of fine tuning. Then it was switched back to the battery a few minutes later after the measurement was done.

The initial antiproton number is based on the PPAC signal which gives a very conservative upper limit of $N_0 < 1559$ from the load-dump calibration. After a hold time of 58.75 days, a final particle number $N_f = 924$ (of these 42 could be background counts) was measured by ejecting the antiprotons from the trap and detecting annihilation signals in a scintillator detector. Particle loss is caused by annihilations with residual gases in the trap, collision interactions and unexpected heating of the magnetron motion. Thus we have $N_f/N_0 = 882/1559$. This immediately gives the antiproton lifetime in the trap of more than 103 days. The measurement is the best directly measured limit.

An extremely high vacuum limit can be established by the antiproton annihilation vacuum gauge. Based on the existing theories on low energy ion-atom (molecule) interactions and studies of antimatter-matter interactions, we can establish (Sec. 6.3) that the number density of atoms is less than $100/cm^3$ which is independent of the relative velocity. For an ideal gas at 4.2 K this would correspond to a pressure less than 5×10^{-17} Torr.

The long trapping time also demonstrates the stability of the trap for an antiproton cloud. Strictly speaking, the magnetron motion is unstable. However, the estimated time constant of this motion due to the radiation damping is 5×10^{14} years. Imperfections in the trap, the sideband heating drive for the magnetron motion and collisions with residual gas may cause instability and antiproton loss with significantly shorter time constant. This test indicates the possibility of a portable antiproton trap. The long lifetime of the antiprotons in an ion trap demonstrated here shows that particle loss could be insignificant during long shipping and waiting periods of several months.

6.2 Other antiproton lifetime measurements

6.2.1 Proton lifetime measurements

The law of baryon number conservation forbids proton and antiproton decay while CPT theorem requires that the proton and antiproton have the same lifetime. The proton lifetime has been measured to $> 1.6\times10^{25}$ years and this result is independent of decay mode [26]. It was done by analyzing geochemical data on xenon isotopes in a telluride ore and investigating all the possible decay products due to nucleon decay. A much higher limit of $> 3.1\times10^{32}$ years [27] was given for the partial lifetime of the assumed predominant proton decay mode (to positron and neutral pion). This partial lifetime is a factor of 40 longer than the predicted proton decay lower limit by the simplest grand unified theory, minimal SU(5) [28,29].

6.2.2 Direct and indirect antiproton lifetime measurements

The available antiproton lifetime measurements were made by investigating antiprotons in a storage ring, or by measuring the branching ratio for a particular decay mode. In a direct antiproton lifetime measurement, 240 antiprotons were stored in the ICE storage ring at CERN for 85 hours in 1978 [30]. A lower limit of 32 hours (3.7×10^{-3} years) was given. Because this experiment was limited by the beam-gas interactions, a new experiment was set up for looking at an antiproton decaying into an electron and a neutral pion for a partial lifetime measurement at the same storage ring in 1979 [31]. A lower limit was given

$$\tau > BR \times 1700\ h \tag{6.1}$$

at 90% confidence level after antiprotons were stored for 10 days. Here, the branching ratio (BR) can only be given by theories (31 to 46 %) [27]. Usually the limit of 0.08 years (one month) is cited from this experiment. Recently antiprotons were held 11 days at the CERN Antiproton Accumulator, with a particle loss rate corresponding to a storage lifetime of 1.4 months in the rest frame of the energetic antiprotons [32].

Based on the cosmic-ray propagation theories, the production of secondary antiprotons through collisions of high-energy cosmic rays with the interstellar medium and a $\overline{p}$/p ratio is predicted to be of the order 10^{-4} for GeV particles. Consistency between theory and the observed cosmic-ray antiprotons and the $\overline{p}$/p ratio measurement by using a balloon-borne superconducting-magnet spectrometer inferred that the antiproton lifetime is at least comparable to the cosmic-ray storage time [33] ($\approx 10^7$ years). However, this indirect argument has not been studied carefully in any detail. Moreover, the cosmic ray storage time for antiprotons has not been measured to our knowledge.

6.3 Stored antiprotons as a vacuum gauge

Any residual gas in the trap would cause annihilation of trapped antiprotons. The antiproton decay rate gives not only a lower limit on the antiproton lifetime, but also an upper limit of the neutral atom number density and the pressure. The antiproton cloud is a sensor to probe the density of the gas molecules and atoms in the vacuum chamber.

We expect the pressure in our vacuum container, kept at 4.2 K, to be extremely low. The great advantage of using a cryopump is discussed in Ref. [75]. Properties of cryogenic liquids and vapor pressure data can be found in Ref. [38]. For H_2,

the vapor pressure is 10^{-7} Torr at 4.03 K and 10^{-6} Torr at 4.40 K. For helium the vapor pressure is 0.1 Torr even at 1 K. However, we are not limited by these vapor pressures as long as those atoms and molecules do not form more than one monolayer on the metal surface [75].

Since the predominant gases are helium and hydrogen [75] at LHe temperature, we will first discuss the annihilation cross section of hydrogen according to the available literature, then study the antiproton- helium interaction process from a more general principle. The number density of the residual gas is obtained for a given antiproton annihilation rate. The relations between the partial pressure of He and H based on the ideal gas law and antiproton lifetime are derived.

6.3.1 Antiproton-hydrogen interaction

Proton-antihydrogen atom and proton-antihydrogen molecule annihilation cross sections at very low energy in collisions

$$p + \overline{H} \longrightarrow Pn + e^{+}, \tag{6.2}$$

and

$$p + \overline{H}_2 \longrightarrow Pn + e^{+} + (\overline{H} \ or \ \overline{p} + e^{+}) \tag{6.3}$$

were studied by Morgan and Hughes [76]. Here, Pn is protonium. The cross sections are the same for their charge-conjugate reactions

$$\overline{p} + H \longrightarrow Pn + e^{-}, \tag{6.4}$$

and

$$\overline{p} + H_2 \longrightarrow Pn + e^{-} + (H \ or \ p + e^{-}) \tag{6.5}$$

The analytic form of the cross section for antiproton-hydrogen atom reaction is given by

$$\sigma(H) = 3.60 \times 10^{5} (c/v_{rel}) \pi r_0^2 \tag{6.6}$$

or

$$\sigma(H) = 1.80 \times 10^5(\sqrt{mc^2/E})\pi r_0^2 \tag{6.7}$$

where v_{rel} is the p-H relative velocity, and $r_0 = 2.82\times10^{-15}$ m is electron classical radius, E = $mv_{rel}^2/4$ is the energy in the center-of-mass system. It is valid when E is between 10^{-5} and 0.1 eV.

In terms of the Bohr radius a_0 instead of the electron classical radius, the same result for the cross section $\sigma(H)$ was rederived by [77] in the form

$$\sigma = 3\pi a_0^2\sqrt{E_0/E} \tag{6.8}$$

where a_0 is the Bohr radius, $E_0 = 27.2$ eV is twice the hydrogen binding energy, and E is the kinetic energy of the antiproton in the center-of-mass system. This is valid for E less than 1 eV. A similar form can also be found in Ref. [78,79]. For E << 1 eV, the cross section is much larger than the geometrical size of the hydrogen atom (about a_0^2) due to the atomic polarization.

The antiproton annihilation rate is R = $n\sigma v_{rel}$, where n is the number density of the gas. Since the lifetime $\tau = 1/R$, we have

$$n(/cm^3) = 1/(6\pi a_0^2\tau\sqrt{E_0/m}) = 3.72 \times 10^8/\tau(sec), \tag{6.9}$$

or

$$n(/cm^3) = 4.3 \times 10^3/\tau(day). \tag{6.10}$$

The number density of the gas is independent of the collision energy. For $\tau = 103$ days, the hydrogen number density is $42/cm^3$. Using the ideal gas law, the number density at temperature T corresponds to the equilibrium hydrogen partial pressure

$$P_H(Torr) = nkT = 4.45 \times 10^{-16}T(K)/\tau(day). \tag{6.11}$$

The hydrogen pressure is 1.2×10^{-15} Torr at 273 K and is 1.8×10^{-17} Torr for thermal equilibrium at 4.2 K. The distribution of the residual gas is not measured

in this experiment. It is likely that the atoms (molecules) are not in Boltzmann distribution.

6.3.2 Antiproton interaction with other gases

Antiproton- helium capture cross section can be understood from general principles. When an antiproton approaches a neutral atom, the electric field of the antiproton $\mathrm{E}(\overline{p}) = -e/r^2$ produces an induced electric dipole moment $\alpha \mathrm{E}(\overline{p})$ at distance r. Here, α is the electric dipole polarizability of an atom describing the response of the electron cloud to an external electric field. The long-range ion-atom interaction energy is simply given as

$$U(r) = -\alpha E^2(\overline{p})/2 = -e^2\alpha/2r^4 \tag{6.12}$$

The ion-atom capture cross section for this interaction is known as the Langevin cross section:

$$\sigma = 2\pi e\sqrt{\alpha/m_r v_{rel}^2} = 2\pi e\sqrt{\alpha/2E} \tag{6.13}$$

where m_r is the reduced mass of the ion-atom pair, v_{rel} is the relative velocity, and E is the collision energy in center-of-mass system. The number density $\mathrm{n} = 1/(\tau\sigma v_{rel})$ is proportional to $\sqrt{m_r/\alpha}$ for a given τ. From Ref. [80], we have $\alpha(H) = 0.667 \times 10^{-24} cm^3$, $\alpha(He) = 0.205 \times 10^{-24} cm^3$, and $\alpha(H_2) = 0.802 \times 10^{-24} cm^3$. The reduced mass of the antiproton-atom (or molecule) pairs are m/2 for H, 2m/3 for H_2, and 4m/5 for He, respectively. Therefore $\mathrm{n(He)} = 2.28\mathrm{n(H)}$, and $\mathrm{n}(H_2) = 1.05\mathrm{n(H)}$. The He atom number density is $95/cm^3$ for a lifetime of 103 days. If we use the ideal gas law,

$$P_{He}(Torr) = 1.01 \times 10^{-15} T(K)/\tau(day). \tag{6.14}$$

The He pressure is 2.7×10^{-15} Torr for the density of 95 He atoms per cm^3 at 273 K and is 4.1×10^{-17} Torr at 4.2 K.

We have discussed the antiproton-gas interactions without considering the presence of the electric field from the trap electrodes. The collisions in the discussion is only for one antiproton interacting with one atom. Here, we can show that those effects are negligible. The particle kinetic energy is 0.54 meV at 4.2 K. The antiproton velocity at this energy is 3.2×10^2 m/sec. The annihilation cross section for hydrogen is $\pi(26a_0)^2$ and for helium is $\pi(19a_0)^2$. The electric field due to the antiproton point charge at distance $26a_0$ is $7.8{\times}10^8$ volt/m. It is much larger than the typical field strength at the center of the trap of 10^3 volt/m. Therefore the effect of the electric field from the trap electrodes is negligible. The effect of an atom interacting with more than one antiproton at the same time is also negligible due to the low antiproton density. The average distance between antiprotons is about 0.02 mm while the interaction distance with an atom is $26a_0 = 10^{-6}$ mm.

Because the Langevin capture cross section is valid for ion-atom interaction, one can also use stripped ions as a vacuum gauge. The capture cross section is proportional to the electric charge number Z and $\sqrt{\alpha/m_r}$. For example, when fully stripped carbon ion interacts with a He atom with Z = 6 and the reduced mass $m_r = 3$ atomic mass unit (amu), the interaction rate is approximately 3.1 times more than the antiproton-He reaction where Z = 1 and $m_r = 0.8$ amu. Trapping fully stripped carbon ions are much easier than trapping antiprotons which rely on the complex accelerators. Thus it is better than using antiprotons as a vacuum gauge.

6.3.3 Vacuum system and cryopump

The vacuum chamber that houses the ion trap is in the bore at the center of the magnet as shown in Chapter 3. The bore has a vacuum of 10^{-5} Torr when cooled to liquid nitrogen temperature. The pressure is below 10^{-6} Torr when the liquid

helium dewar attached to the trap enclosure is cooled to liquid helium temperature. Since gas diffusion through cold material is eliminated, only the joints for different parts are potential leaking locations. There are several types of seals to separate the extreme high vacuum from the bore pressure. They are a glass-metal seal, silver hard solder to seal feedthroughs with the copper, electron beam welding to join Ti foil to Ti rings which is then to copper, and an indium-squeezing seal. All of them worked and ensured the long lifetime of antiprotons in ion trap.

Thompson and Hanrahan [75] used a quadrapole mass analyzer to measure the partial pressures from 300 to 30 K and found that hydrogen and helium pressures are below 10^{-14} Torr at 30 K while other gases are frozen out near 77 K. A completely pre-pumped sealed-off vacuum chamber cooled at 4.2 K provides an extreme high vacuum environment by cryopumping because the outgassing within the vacuum chamber can be eliminated by cooling the gases below the desorption activation energy if the gases form less than one monolayer on the inner surface of the chamber.

We can estimate the pressure at room temperature corresponding to a monolayer coverage when the apparatus is cooled to 4.2 K. The cold surface within the vacuum chamber is about 0.1 m^2. We assume each particle occupies 3Å×3Å= $9\times10^{-20}m^2$. That means approximately 10^{18} particles are needed to form a monolayer. At room temperature for a volume of 1 litre in the chamber, 10^{18} particles correspond to a vacuum pressure of 10^{-5} atm (0.01 Torr). The density of 6×10^{23} particles in 22.4 litres is used here. Based on this estimate, we need to obtain 0.01 Torr before sealing at room temperature by rough pumping the chamber to reduce the amount of hydrogen and helium so that there is no more than a monolayer coverage of the surfaces at low temperature. This pressure is very easy to achieve. We should note that there is only a small fraction of helium (5×10^{-6}) and hydrogen (5×10^{-7}) gas in the air at 1 atm. Even without rough pumping, helium or hydro-

gen from the air would not be able to form a monolayer. In reality, there is much more helium gas in the trap can before rough pumping since liquid helium and helium gas are used in the laboratory. Therefore in practice, the vacuum chamber is carefully pumped and leak checked, then baked to 120^{0}C with a typical pressure of 10^{-6} Torr or less. After the system cools down to room temperature, the partial pressure reaches about 2×10^{-7} Torr for hydrogen measured by a mass analyzer before sealing. The helium pressure is on the order of 10^{-9} Torr as measured by a mass analyzer. Thus, the residual atoms and molecules are far less than the numbers needed to form a monolayer.

The He mean path length $(1/n\sigma)$ at 4.2 K is around 3×10^6 km which is much larger than the size of the apparatus, an indication of ultrahigh vacuum. The vacuum pressure reported here ($< 5 \times 10^{-17}$ Torr at 4.2 K when the ideal gas law is applied) is the best reported value. It is consistent with the previous vacuum pressure measurement ($< 10^{-14}$ Torr at 30 K) using a quadrapole mass analyzer [75].

Chapter 7

Antiproton mass measurement and other experiments in an ion trap

7.1 Antiproton mass measurement

7.1.1 Antiproton cyclotron frequency measurement

Comparison of antiproton and proton cyclotron frequencies yields the ratio of inertial masses [12,25]

$$m(\overline{p})/m(p) = 0.999\ 999\ 977(42). \tag{7.1}$$

Antiprotons are cooled into the harmonic potential well by a cloud of electrons. Then most electrons are removed from the trap by suddenly reducing the trapping potential to 4 V or less while applying a strong axial drive ν_z(e) and axial cooling sideband drive ν_z(e)+ν_m(e). When the antiprotons are driven very close to their cyclotron sideband frequency $\nu_c' + \nu_m$ for a short period and enough energy is pumped into their axial motion and cyclotron motion, the heating signals are detected from the axial preamplifier and cyclotron preamplifier simultaneously.

These signals are directly shown on two spectrum analyzers after further amplification.

If too much energy is put into the system, signals are broadened. Especially the cyclotron signal is asymmetric. While antiprotons dissipate energy via electron cooling and resistor damping, the linewidth becomes narrower and the cyclotron ν_c' signal becomes more symmetric. The damping time ranges from a few seconds to hours. We can deduce the cyclotron frequency ν_c from the invariance theorem [81]

$$(\nu_c)^2 = (\nu_c')^2 + (\nu_z)^2 + (\nu_m)^2 \tag{7.2}$$

which has been shown to be invariant under the leading perturbations of an imperfect Penning trap. The magnetron frequency can be eliminated from the invariance theorem to obtain the approximation

$$\nu_c \approx \nu_c' + \nu_z^2/2\nu_c'. \tag{7.3}$$

The higher order terms are negligible, and will be discussed later. Antiprotons are confined in the center of the ring which is split into 4 segments. The cyclotron frequency drive line is connected to two ring segments. The third segment is used for cyclotron frequency detection and the other provides an RF ground. The amplified cyclotron signal is mixed down below 100 kHz and can be observed on a spectrum analyzer (HP 3561A Dynamic Signal Analyzer). The amplified axial signal from the lower compensation electrode can be seen from an HP 8562A spectrum analyzer with a lower resolution (minimum resolution bandwidth 100 Hz). The schematic diagram for antiproton (proton) cyclotron frequency measurement is shown in Fig. 7.1. In our system, a 50 Hz shift in axial frequency corresponds to 1 Hz modification to the cyclotron frequency. Typical resonant signals for the antiproton cyclotron frequency measurement are shown in Fig. 7.2. In Fig. 7.2(a), the antiproton cyclotron frequency ν_c' = 89 133 083±1 Hz with a width of 2 Hz is plotted. Fig. 7.2(b) shows the antiproton axial resonance. The axial frequency is

ν_z = 1 907 550±100 Hz and hence the magnetron frequency ν_m=20 412±2 Hz is obtained. Therefore we have $\nu_c = \nu_c' + \nu_m$ = 89 153 495±2 Hz.

Proton cyclotron measurements are carried out in the same way except the polarity of the trapping potential is opposite. The electron cyclotron frequency is obtained when a microwave drive is swept through the cyclotron which shifts the electron axial. Thereby the mass ratios of antiproton to proton, antiproton to electron, and proton to electron are measured. Averaging over 5 comparisons [12], we obtain $m(\overline{p})/m(p) = 0.999\ 999\ 977$. Antiproton and proton masses are in agreement within an uncertainty of 4×10^{-8}. The mass ratio of proton to electron [12] is in good agreement with a slightly more accurate m_p/m_e value [23].

7.1.2 Systematic analysis and results

Even though the linewidth of the observed signals can be very narrow with a resolution of 10^{-8}, systematic effects may cause much larger shifts due to trap imperfections, field inhomogeneity, and particle interactions. The long term drift of the superconducting magnet must be accounted for. Small magnetic field fluctuations are shielded [55] while large magnetic field shifts need special corrections.

It is necessary to examine the validity of the simple formula we have used in the equation $\nu_c = \nu_c' + \nu_z^2/2\nu_c'$. Considering the effects of misalignments of the magnetic field to the axis of the electric quadrupole following Ref. [73]:

$$\mathbf{B} = B(cos\theta\mathbf{i} + sin\theta cos\phi\mathbf{j} + sin\theta sin\phi\mathbf{k}) \tag{7.4}$$

and internal misalignments of the trap electrodes causing departure of the quadratic terms in the electrostatic potential:

$$U = (1/2)m\omega_z^2[z^2 - (1/2)(x^2 + y^2) - (1/2)\varepsilon(x^2 - y^2)] \tag{7.5}$$

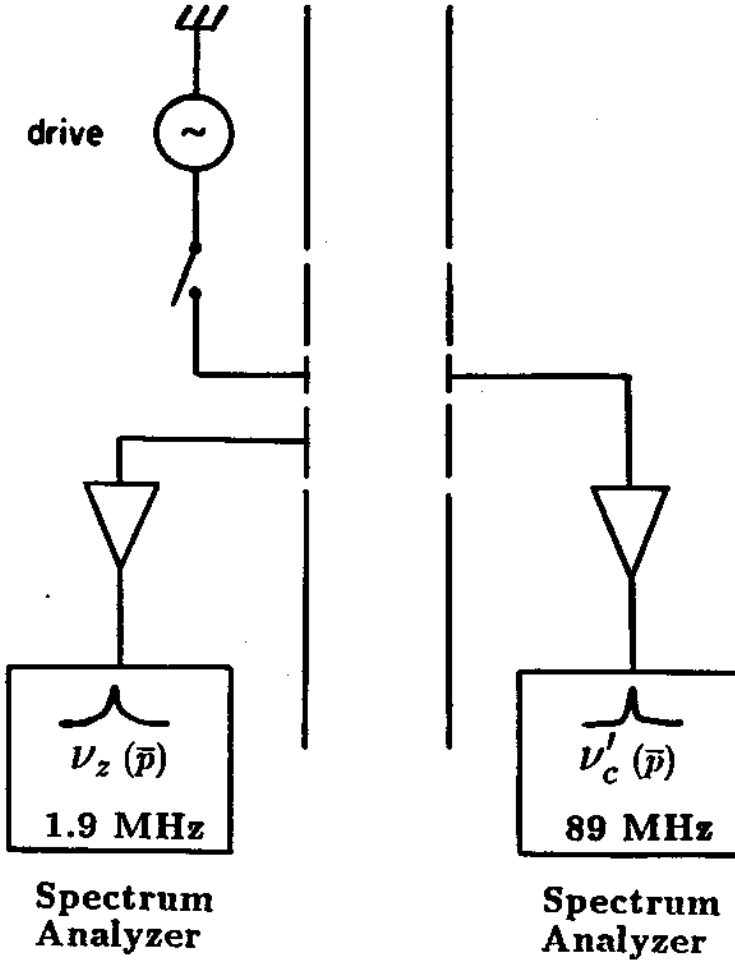

Figure 7.1: Schematic diagram for antiproton (proton) cyclotron frequency measurement.

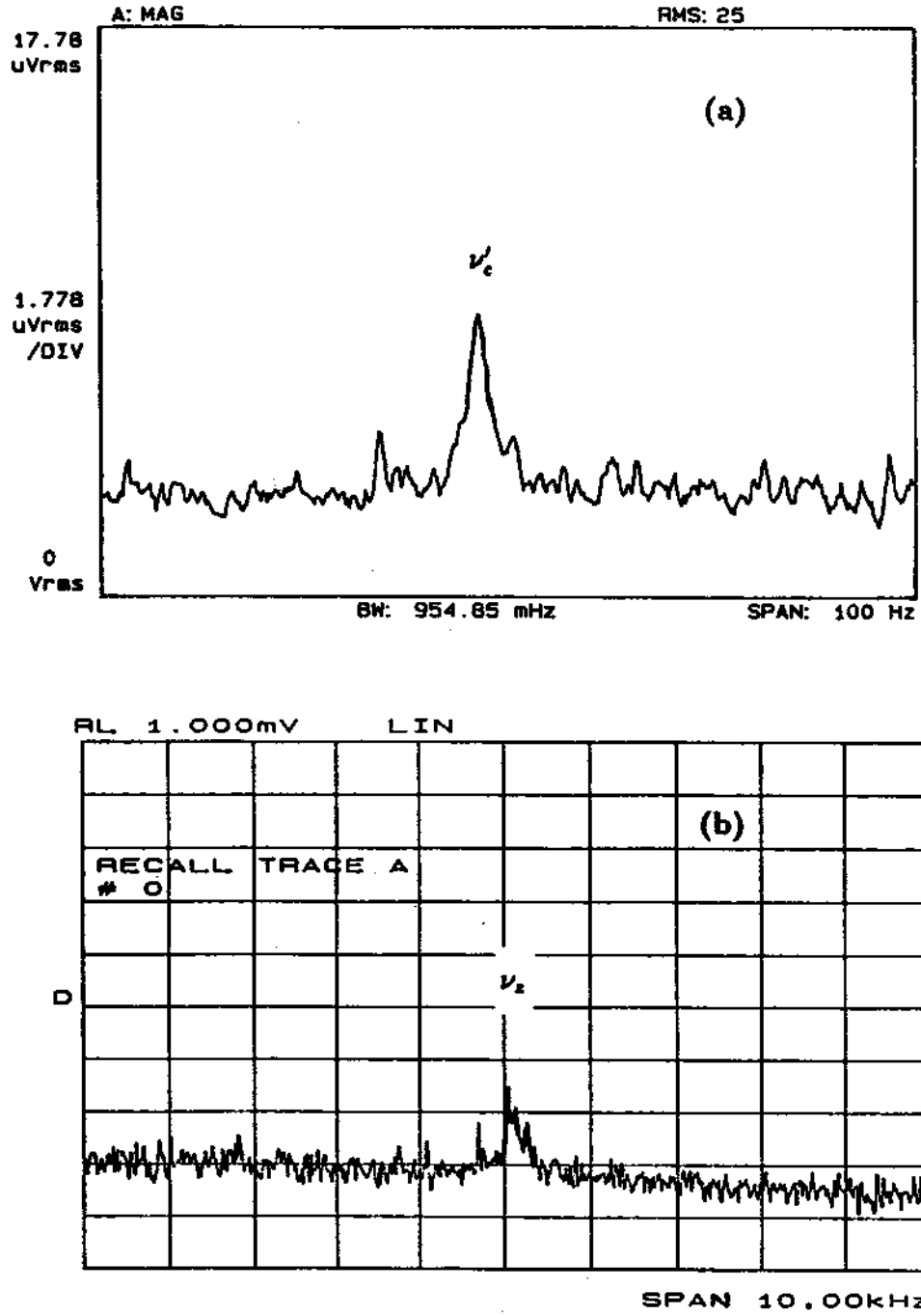

Figure 7.2: (a) Antiproton cyclotron resonance. (b) Antiproton axial resonance.

where ϵ is the asymmetry parameter representing the harmonic imperfections. The fractional correction to the above electromagnetic static fields is given by

$$\Delta\nu_c/\nu_c \approx (9/16)(\nu_z^4/\nu_c'^4)(\theta^2 - 2\epsilon^2/9) \tag{7.6}$$

For electrons with an axial frequency of 54 MHz and a cyclotron frequency of 164 GHz, we have

$$\Delta\nu_c/\nu_c(\theta = 1^o, \epsilon = 0) = 2 \times 10^{-18}, \tag{7.7}$$

and

$$\Delta\nu_c/\nu_c(\theta = 0, \epsilon = 0.01) = -1.5 \times 10^{-19}. \tag{7.8}$$

For proton (antiproton) frequencies of $\nu_z = 1.91$ MHz and $\nu_c' = 89.3$ MHz, the corrections from Eqs. (7.7) and (7.8) are 3.6×10^{-11} and -2.6×10^{-12}, respectively.

There are many sources such as gaps in the electrodes, machining error in electrode dimensions, and misaligned trap which can introduce trap anharmonicity. The most significant anharmonicity is from the C_4 term which was introduced in Chapter 5. The shift in the cyclotron frequency measurement is given as [73]

$$\Delta\nu_c/\nu_c \approx (3/4)C_4(\nu_z/\nu_c)^2(\rho_m/z_0)^2. \tag{7.9}$$

It depends on the location of the particles. A large magnetron orbit will make a big shift. For example, we have $(\nu_z/\nu_c)^2 = 1.1 \times 10^{-7}$ for electron and 4.6×10^{-4} for proton (antiproton) in our system. We take $\rho_m/z_0 = 0.1$, that is, $\rho_m \approx 0.6$ mm, then the effects are

$$\Delta\nu_c/\nu_c = 3.5 \times 10^{-6} C_4 \ for\ antiproton, \tag{7.10}$$

and

$$\Delta\nu_c/\nu_c \approx 10^{-8} C_4 \ for\ electron. \tag{7.11}$$

Since $C_4 < 10^{-3}$ (it can be tuned away by adjusting the compensation potential V_c. The C_4 given here corresponds $\Delta V_c = 0.1$ V), this effect only contributes a small

shift for antiprotons which is less than 10^{-8}, and is negligible for an electron. This has been tested experimentally by searching for frequency shifts while changing the compensation potential.

A magnetic field homogeneity of $10^{-8}/cm^3$ can be achieved in our magnet as measured with NMR techniques without the presence of the trap. Once the center of the magnet is surrounded by trap electrodes, the field is distorted by the paramagnetism and diamagnetism of the trap material. The magnetizations for Cu is -0.05 and for MACOR is $+0.78$ (see Ref. [73]). The lowest order axial component of the magnetic field can be expressed as

$$\Delta B_z = B_z(z^2 - \rho^2/2). \tag{7.12}$$

This magnetic bottle causes a cyclotron frequency shift of

$$\Delta\nu_c/\nu_c = B_2(z^2 - \rho_m^2). \tag{7.13}$$

The coefficient B_2 is calculated to be less than $10^{-7}/mm^2$. The effect is less than 2×10^{-8} for z = 0 and $\rho_m = 0.4$ mm.

For a cloud of charged particles of a single species, no frequency shifts should be observed since only center-of-mass motions of the cloud are detected by the preamplifiers [66]. There is no number dependency observed at the 10^{-8} level. The possible effect from the contaminant particles are studied. For typical cloud densities and compositions used, we conclude that the effect of contaminant particles are less than 2×10^{-8}.

Using half the observed cyclotron linewidth as the uncertainty, the fractional standard deviation of the five measured ratios is 3.4×10^{-8}, while the scatter in the five independent sets of comparisons is only 1.4×10^{-8}. We obtained the error quoted by adding the standard deviation for the point, the scatter, and the

systematic limit in quadrature, to obtain a standard deviation which is 4.2×10^{-8} of the mass ratio. The new mass ratio of antiproton and proton

$$m(\overline{p})/m(p) = 0.999\ 999\ 977(42) \tag{7.14}$$

is shown in Fig. 7.3, comparing with previous measurements. The error bar for our measurement is 50 times smaller than the diameter of the point. The fractional uncertainty of 4×10^{-8} is 1000 times more accurate than previous antiproton mass measurements using exotic atoms and is the most precise test of CPT invariance with baryons.

7.2 The gravitational mass of antimatter

The gravitational mass of the antimatter has not yet been directly measured. So far, there is no successful quantum field theory for gravitational fields to anticipate it and to explicitly establish CPT invariance. To measure the gravitational acceleration of the antiproton by launching ultracold antiprotons up through a 1 meter long (L) vertical drift tube from a Penning trap has been proposed [82]. The plan is to use the time of flight technique similar to the reported measurement of the electron gravitational force by Witteborn and Fairbank [83]. A cutoff time ($t_c = \sqrt{2L/g}$) will be measured for the lowest energy antiprotons reaching a detector at the top of the drift tube, hence the gravitational acceleration g is obtained. The cutoff time would be 0.45 sec for an initial kinetic energy of 0.1 μV which is required to overcome the 1 m height difference if we assume $g(\overline{p}) = g(p)$. This is a direct test of the equality of particle and antiparticle gravitational masses with protons and antiprotons. They propose to achieve a 1% accuracy measurement of the gravitational acceleration of antiprotons relative to the H^- ion by launching of a total of 10^6 to 10^7 particles. However, the major difficulties arise from the extreme weakness of the gravitational interaction. Even a single charged particle

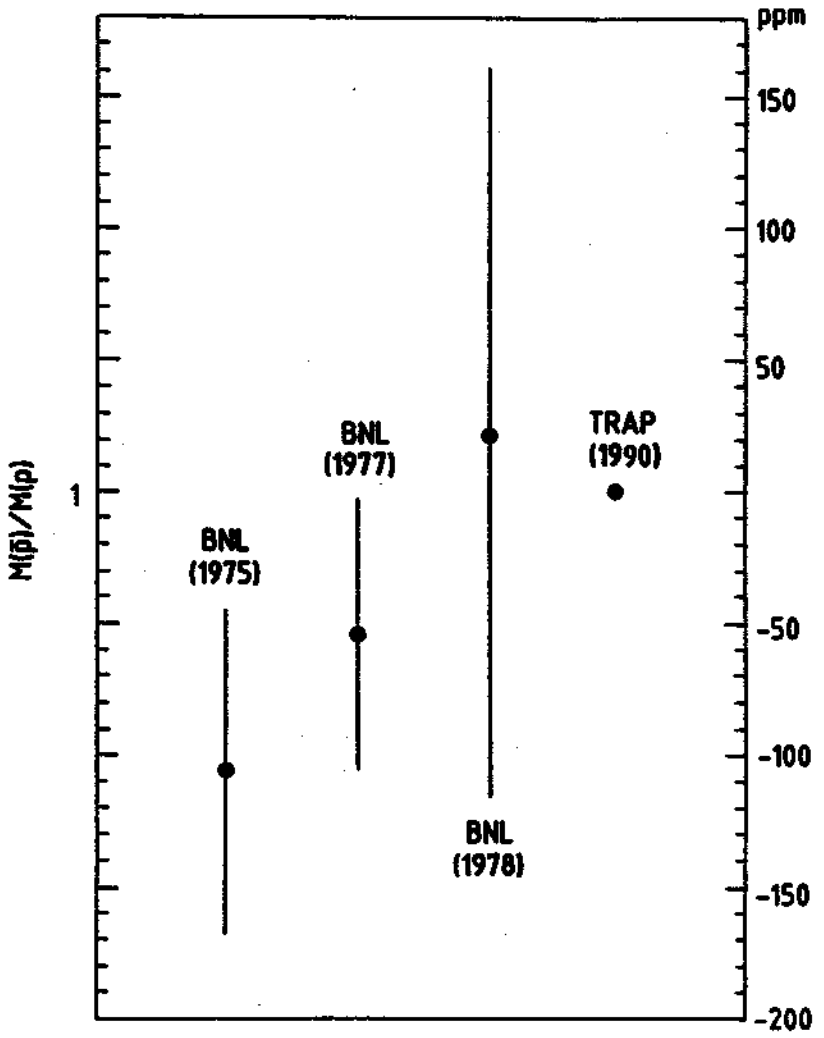

Figure 7.3: The new mass ratio of antiproton and proton is shown here, comparing with previous measurements. The error bar for our measurement is 50 times smaller than the diameter of the point.

within 12 cm would be able to balance the gravitational force of the earth acting on an antiproton if we assume that an antiproton has the same gravitational mass as the proton. Since antihydrogen is less sensitive to stray electric fields, a gravitational measurement of antihydrogen seems more promising once it is available [6]. The strong Coulomb repulsion between the particles as they are launched also can cause large problems. Such Coulomb explosions and stray fields in our apparatus have limited our energy resolution to 5 meV, while the gravitational potential energy for a proton over one meter is 10^{-4} meV.

7.3 Antihydrogen production and antihydrogen physics

A positron and an antiproton together will form an antihydrogen atom. If low energy positrons and antiprotons can interact with each other in a nested trap as discussed in Ref. [7] which consists a series of electrodes, antihydrogen would be produced [7]. In this scheme, preloaded positrons from a positron moderator are confined in a harmonic potential well with negative potentials on the ring and compensation electrodes. By positron cooling which is analogous to the electron cooling described in Chapter 5, antiprotons trapped in the long trap lose energy while colliding with positrons. Since the potential well for positrons is a potential barrier for antiprotons, only antiprotons with a kinetic energy larger than the effective barrier potential energy can interact with positrons and have a chance of forming antihydrogen. During the antiproton slowing process the recombination rate is enhanced greatly since the reaction rate is higher when the relative velocity between positron and antiproton is lower. Two processes would happen naturally: radiative recombination $\overline{p} + e^+ \longrightarrow \overline{H} + h\nu$, and 3-body recombination $\overline{p} + e^+ + e^+ \longrightarrow \overline{H} + e^+$. The 3 body recombination process could give very high production rate at low temperature (about 600 per second per antiproton for a

positron density of $10^7/cm^3$ at 4.2 K) [5] since the rate-temperature dependence is $T^{-9/2}$ while radiative recombination is $T^{-1/2}$.

Other proposed methods are merging a positron beam or positronium beam with antiprotons $Ps + \overline{p} \longrightarrow \overline{H} + e^-$ [3]. Antihydrogen physics may include precision antihydrogen spectroscopy, antihydrogen gravitational mass measurement [6], and the formation of antihydrogen molecules. Other ideas can be found in Ref.[3].

7.4 Antideuteron

Trapping antiprotons and related studies can be naturally applied in trapping heavier charged antinuclei such as an antideuteron. Conservation of baryon number requires that antiprotons and antideuterons can only be produced along with their particle counterparts:

$$p + p \longrightarrow p + p + \overline{p} + p, \tag{7.15}$$

and

$$p + p \longrightarrow p + p + \overline{d} + d. \tag{7.16}$$

The initial proton energy needed to produce one antinucleus must have a net center of mass energy of twice the nucleus mass. For antiprotons produced when fast protons collide with protons at rest, the laboratory energy of the incident protons must be above 5.6 GeV. Actually the Berkeley Bevatron was designed at 6 GeV to exceed this threshold energy for antiproton production. However, if the target proton is in a Cu-nucleus, it is a moving target because it undergoes Fermi motion. Antiprotons can thus be produced with 3 GeV protons incident on targets containing heavy elements, but with much lower production rates since only a small fraction of collisions are head on collisions with the moving target protons. The higher the incident proton energy, the more the antiparticle yield per proton. Due to the proton beam energy requirement, it is much more difficult to make heavier

antiparticles. Antideuteron was discovered in 30 GeV proton-beryllium collisions at BNL [84]. With 30 GeV protons incident upon protons at rest, the net energy available is 5.74 GeV which is larger than $2m_{\overline{d}} \approx 4$ GeV. Production of fairly large amounts of antideuteron is feasible. The possibility of building an antideuteron ring similar to LEAR has been discussed [85]. Many fewer antideuterons would be accumulated compared with antiprotons since heavier particles are more difficult to produce. Koch estimated the $\overline{d}/\overline{p}$ ratio for a 26 GeV/c primary, 3.5 GeV/c secondary, in the forward direction to be 4×10^{-6} $\overline{d}/\overline{p}$. This gives 200 $\overline{d}$ per pulse (10^{13} p) in a storage ring. With small modifications to the present antiproton production facility at CERN more than 10^6 antideuterons per day could be stored and used for experiments [86]. If those stored antideuterons could be decelerated to the order of 10 MeV, it seems possible to trap and cool a few antideuterons in an ion trap. The antideuteron energy loss (dE/dx) in matter is the same as for antiprotons of same velocity. Their energy stragglings in matter are very similar. For example, the 12 MeV antideuteron straggling parameter in Al is 1.4 times that of 6 MeV antiprotons [37]. The low energy antideuteron yield should be more than 10^{-4}/keV for the 12 MeV beam based on the antiproton test. Therefore, 10^2 antideuterons per day could be confined in an ion trap if we assume the slowing and trapping efficiency is 10^{-4} which has been achieved in our antiproton experiment. The particles in the trap are suitable for the high precision antideuteron mass measurement, and thus the antineutron mass and the binding energy in antideuteron (the binding energy for deuteron is 2.225 MeV).

7.5 Portable antiproton source

The movable source of antiprotons could make antiprotons available to a new research community normally unrelated to the accelerator physics. Portable antiprotons stored in an ion trap and transferred between laboratories has been

suggested [87]. One big concern is that a very good vacuum is needed to eliminate antiproton loss by collisions with neutral gases. The long lifetime of the antiprotons in an ion trap demonstrated in this experiment shows that the particle loss could be insignificant during long shipping and waiting periods of several months.

7.6 Summary

Summarizing, energetic antiprotons are slowed down in matter and captured indefinitely in an ion trap. They reach thermal equilibrium with their surroundings at 4.2 K via electron cooling or resistor damping. High precision mass comparisons for antiproton and proton (or electron) in the trap are carried out with a fractional accuracy of 4×10^{-8} which is a 1000-fold improvement in the measured antiproton mass. Another factor of 100 improvement is sought. Trapped cryogenic antiprotons are also suited for antiproton-atom interaction studies, antihydrogen production, antimatter gravitational mass measurements, long time storage and transfer. The great success of trapping low energy antiprotons in an ion trap marks the completion of the task of confining all the stable charged elementary particles (electrons, positrons, protons and antiprotons) and opens the way to other intriguing experiments.

Bibliography

[1] **Physics at LEAR with Low-Energy Cooled Antiprotons**, edited by U. Gastaldi and R. Klapisch (Plenum, New York, 1982).

[2] **Physics with Antiprotons at LEAR in the ACOL Era**, edited by U. Gastaldi, R. Klapisch, J.M. Richard, and J. Tran Thanh Van (Editions Frontières, Gif-Sur-Yvette, 1985).

[3] Hyperfine Interaction, Vol.44 (1988).

[4] G. Gabrielse, H. Kalinowsky, and W. Kells, in Ref. [2].

[5] G. Gabrielse, S.L. Rolston, L. Haarsma, and W. Kells, Phys. Lett. A **129**, 38 (1988).

[6] G. Garielse, Hyperfine Interact. **44**, 349 (1988).

[7] G. Gabrielse, K. Helmerson, R. Tjoelker, X. Fei, T.A. Trainor, W. Kells, and H. Kalinowsky, in Proceedings of the first workshop on antimatter physics at low energy, edited by B.E. Bonner, L.S. Pinsky (Fermilab, Batavia, 1986), p.211.

[8] G. Gabrielse, X. Fei, L. Haarsma, S.L. Rolston, R. Tjoelker, T.A. Trainor, H. Kalinowsky, J. Haas, and W. Kells, Physica Scripta, **T22**, 36 (1988).

[9] G. Gabrielse, X. Fei, K. Helmerson, S.L. Rolston, R. Tjoelker, T.A. Trainor, H. Kalinowsky, J. Haas, and W. Kells, Phys. Rev. Lett. **57**, 2504 (1986).

[10] G. Gabrielse, X. Fei, L.A. Orozco, S.L. Rolston, R.L. Tjoelker, T.A. Trainor, J. Haas, H. Kalinowsky, and W. Kells, Phys. Rev. A**40**, 481 (1989).

[11] G. Gabrielse, X. Fei, L.A. Orozco, R.L. Tjoelker, J. Haas, H. Kalinowsky, T.A. Trainor, and W. Kells, Phys. Rev. Lett. **63**, 1360 (1989).

[12] G. Gabrielse, X. Fei, L.A. Orozco, R.L. Tjoelker, J. Haas, H. Kalinowsky, T.A. Trainor, and W. Kells, Phys. Rev. Lett. **65**, 1317 (1990).

[13] G. Lüders, Annals of Physics, **2**, 1 (1957).

[14] O. Chamberlain, E. Segrè, C. Wiegand, and T. Ypsilantis, Phys. Rev. **100**, 947 (1955).

[15] A. Bamberger, U. Lynen, H. Piekarz, J. Piekarz, B. Povh, H.G. Ritter, G. Backenstoss, T. Bunaciu, J. Egger, W.D. Hamilton and H. Koch, Phys. Lett. **33B**, 233 (1970).

[16] E. Hu, Y. Asano, M. Y. Chen, S.C. Cheng, G. Dugan, L. Lidofsky, W. Patton, C. S. Wu, V. Hughes and D. Lu, Nucl. Phys. A**254**, 403 (1975).

[17] P. Roberson, T. King, R. Kunselman, J. Miller, R.J. Powers, P.D. Barnes, R.A. Eisenstein, R.B. Sutton, W.C. Lam, C.R. Cox, M. Eckhause, J.R. Kane, A.M. Rushton, W.F. Vulcan, R.E. Welsh, Phys. Rev. C**16**, 1945 (1977).

[18] B.L. Roberts, Phys. Rev. D**17**, 358 (1978).

[19] F.L. Moore, D.L. Farnham, P.B. Schwinberg, and R. S. Van Dyck Jr. Nucl. Instrum. Methods Phys. Res. **B43**, 425 (1989).

[20] E.A. Cornell, R.M. Weisskoff, K.R. Boyce, R. W. Flanagan,Jr. G.P. Lafyatis, and D.E. Prichard, Phys. Rev. Lett. **63**, 1674 (1989).

[21] R.S. Van Dyck,Jr., P.B. Schwinberg, and H.G. Dehmelt, Phys. Rev. Lett. **59**, 26 (1987).

[22] R.S. Van Dyck,Jr., F.L. Moore, D.L. Farnham and P. B. Schwinberg, Int. J. Mass Spectrom. Ion Processes **66**, 327 (1985).

[23] R. S. Van Dyck,Jr., F.L. Moore, D.L. Farnham and P. B. Schwinberg, Bull. Am. Phys. Soc. **31**, 244 (1986).

[24] G. Gabriese, H. Kalinowsky, W. Kells, and T. Trainor, CERN Report No. CERN/PSCC/85-21PSCC/P83, 1985.

[25] R.L. Tjoelker, Ph.D. thesis (Harvard University, 1990).

[26] J.C. Evans, Jr. and R.I. Steinberg, Science, **197**, 989 (1977).

[27] Particle Data Group, **Review of Particle Properties**, Phys. Lett. **B204**, (1988).

[28] H. Georgi, and S.L. Glashow, Phys. Rev. Lett. **32**, 438 (1974).

[29] See review by W. Lucha, Comments Nucl. Part. Phys., **16**, 155 (1986).

[30] M. Bregman, M. Calvetti, G. Carron, S. Cittolin, M. Hauer, H. Herr, H. Koziol, F. Krienen, P. Kristensen, G. Lebee, D. Mohl, G. Petrucci, C. Rubbia, D. Simon, G. Stefanini, L.Thorndahl, S. van der Meer, T. Wikberg, Phys. Lett. **78B**, 174 (1978).

[31] M. Bell, M. Calvetti, G. Carron, J. Chaney, S. Cittolin, M. Hauer, H. Herr, F. Krienen, G. Lebee, D. Mohl, P. M. Petersen, G. Petrucci, H. Poth, C. Rubbia, D. Simon, G. Stefanini, L. Tecchio, S. van der Meer and T. Wikberg, Phys. Lett. **86B**, 215 (1979).

[32] B. Autin, G. Carron, F. Caspers, V. Chohan, E. Jones, G. le Dallic, S. Maury, C. Metzger, D. Mohl, Y. Orlov, F. Pedersen, A. Poncet, J.C. Schnuriger, T.R. Sherwood, C.S. Taylor, L. Thorndahl, S. van der Meer, D.J. Williams, in Proc. of Eur. Part. Accl. Conf. (1990).

[33] R.L. Golden, S. Horan, B.G. Mauger, G.D. Badhwar, J.L. Lacy, S.A. Stephens, R.R. Daniel, and J.E. Zipse, Phys. Rev. Lett. **43**, 1196 (1979).

[34] B. Autin, Hyperfine Interact., **44**, 11 (1988).

[35] C.D. Johnson, Hyperfine Interact., **44**, 21 (1988).

[36] S. van der Meer, Rev. Mod. Phys., **57**, 689 (1985).

[37] H. Bichsel, in **American Institute of Physics Handbook**, (McGraw-Hill, New York, 1972), pp.8-142 to 8-189.

[38] **Physics Vade Mecum**, editor in chief H.L. Anderson, 1981.

[39] J.F. Ziegler, J.P. Biersack, and U. Littmark, **The stopping and range of ions in solids**, (Pergamon Press, New York, 1985).

[40] J.L. Wiza, Nucl. Instrum. Method., **162**, 587 (1979).

[41] L.C. Northcliffe and R.F. Schilling, Nucl. Data Tables **A7**, 233 (1970).

[42] T.A. Trainor, in **Annual Report, Nuclear Physics Lab.,University of Washington**, (Seattle, 1988).

[43] H. Stelzer, Nucl. Instrum. Method. **133**, 409 (1976).

[44] W.H. Barkas, W. Birnbaun, and F.M. Smith, Phys. Rev.**101**, 778 (1956); W.H. Barkas, J.N. Dyer, H.H. Heckman, Phys. Rev. Lett. **11**, 26 (1963).

[45] A.R. Clark, R.C. Field, H.J. Frisch, W.R. Holley, R.P. Johnson, L.T. Kerth, R.C. Sah, and W.A. Wenzel, Phys. Lett. **41B**, 229 (1972).

[46] W. Wilhelm, H. Daniel, and F.J. Hartmann, Phys. Lett. **98B**, 33 (1981).

[47] H.H. Andersen, H. Simonsen, and H. Sorensen, Nucl. Phys. **A125**, 171 (1969); H.H. Andersen, J.F. Bak, H. Knudsen, and B.R. Nielsen, Phys. Rev. A **16**, 1929 (1977).

[48] J.C. Ashley, R.H. Ritchie, and W. Brandt, Phys. Rev. B5, 2393 (1972); Phys. Rev. A8, 2402 (1973).

[49] J.D. Jackson, and R.L. McCarthy, Phys. Rev. B6, 4131 (1972).

[50] J. Lindhard, Nucl. Instrum. Methods **132**, 1 (1976).

[51] R.H. Ritchie and W. Brandt, Phys. Rev. A **17**, 2102 (1978).

[52] L.H. Andersen, P. Hvelplund, H. Knudsen, S.P. Møller, J.O. Pedersen, E. Uggerhøj, K. Elsner, E. Morenzoni, Phys. Rev. Lett., **62**, 1731 (1989).

[53] X. Fei, R. Davisson, and G. Gabrielse, Rev. Sci. Instrum. **58**, 2197 (1987).

[54] G. Gabrielse, L. Haarsma, and S.L. Rolston, Int. J. Mass Spectrom. Ion Processes **88**, 319 (1989).

[55] G. Gabrielse and J. Tan, J. Appl. Phys. **63**, 5143 (1988).

[56] G. Gabrielse, J. Tan, P. Clateman, L.A. Orozco, S.L. Rolston, C.H. Tseng, R.L. Tjoelker, submitted to J. of Mag. Res.

[57] C. Baltay, P. Franzini, G. Lütjens, J.C. Severiens, D. Tycko, and D. Zanello, Phys. Rev. **145**, 1103 (1966); C. Baltay, N. Barash, P. Franzini, N. Gelfand, L. Kirsch, G. Lütjens, D. Miller, J.C. Severiens, J. Steinberger, T.H. Tan, D. Tycko, D. Zanello, R. Goldberg and R.J. Plano, Phys. Rev. Lett. **15**, 532 (1966).

[58] C.F. Driscoll, K.S. Fine, and J.H. Malmberg, Phys. Fluids **29**, 2015 (1986).

[59] D. Kind, **An Introduction to High-Voltage Experimental Technique** (Vieweg, Braunschweig, 1978), pp.39-41 and 176-177.

[60] R.C. Hyer, H.D. Stuphin, and K.R. Winn, Rev. Sci. Instrum. **46**, 1333 (1975); S. Dong, W. Krause, F. Volker, and H. Weber, Rev. Sci. Instrum. **57**, 539

(1986); B. Cunin, J.A. Miehe, B. Sipp, M.Ya. Schelev, J.N. Serduchenko, and J. Thebault, Rev. Sci. Instrum. **51**, 103 (1980).

[61] W. Kells, G. Gabrielse, and K. Helmerson, Fermilab Report Conf. No. 84/68 E, 1984

[62] S.L. Rolston and G. Gabrielse, Hyperfine Interact. **44**, 233 (1988).

[63] L. Spitzer, Physics of Fully Ionized Gases (InterScience, New York, 1962).

[64] G.I. Budker, N.S. Dikansky, V.I. Kudelainen, I.N. Meshkov, U.U. Parkomchuk, D.V. Pestrikov, A.N. Skrinsky, and B.N. Sukhina, Part. Accel. **7**, 197 (1976).

[65] D.J. Larson, J.C. Berquist, J.J. Bollinger, W.M. Itano, and D.J. Wineland, Phys. Rev. Lett. **57**, 7 (1986).

[66] D. Wineland, and H. Dehmelt, J. Appl. Phys. **46**, 919 (1975).

[67] G. Gabrielse, Phys. Rev. **A27**, 2277 (1983).

[68] R.S. Van Dyck, Jr., P.B. Schwinberg, and H. Dehmelt, in: **New Frontiers in High-Energy Physics**, B.M. Kursunoglu, A. Perlmutter and L.F. Scott, eds. (Plenum, New York, 1978).

[69] P. Horowitz, and W. Hill, **The art of electronics**, (Cambridge University Press, Cambridge, 1980),p.84.

[70] W.W. Macalpine, and R.O. Schildknecht, in **Proceedings of the IRE**, 2099 (1959).

[71] **The ARRL Handbook for the Radio Amateur**, edited by M.J. Wilson, (The American Radio Relay League, Newington, 1988).

[72] F.L. Walls, and H.G. Dehmelt, Phys. Rev. Lett. **21**, 127 (1968).

[73] L.S. Brown and G. Gabrielse, Rev. Mod. Phys. **58**, 233 (1986).

[74] J.H. Malmberg, and T.M. O'Neil, Phys. Rev. Lett. **39**, 1333 (1977).

[75] W. Thompson and S. Hanrahan, J. Vac. Sci. Technol. **14**, 643 (1977).

[76] D.L. Morgan, Jr. and V.W. Hughes, Phys. Rev. **D2**, 1389 (1970).

[77] L. Bracci, G. Fiorentini and O. Pitzurra, Phys. Lett. **85B**, 280 (1979).

[78] D.L. Morgan, Jr. and V.W. Hughes, Phys. Rev. **A7**, 1811 (1973).

[79] D.L. Morgan, Jr. Hyperfine Interact. **44**, 399 (1988).

[80] **CRC Handbook of Chemistry and Physics**, editor in chief R.C. Weast, (CRC Press, Boca Raton, 1986).

[81] L.S. Brown and G. Gabrielse, Phys. Rev. **A25**, 2423 (1982).

[82] N. Beverini, J.H. Billen, B.E. Bonner, L. Bracci, R.E. Brown, L.J. Campbell, D.A. Church, K.R. Crandall, D.J. Ernst, A.L. Ford, T. Goldman, D.B. Holtkamp, M.H. Holzscheiter, S.D. Howe, R.J. Hughes, M.V. Hynes, N. Jarmie, R.A. Kenefick, N.S.P. King, V. Lagomarsino, G. Manuzio, M.M. Nieto, A. Picklesimer, J. Reading, W. Saylor, E.R. Siciliano, J.E. Stovall, P.C. Tandy, R.M. Thaler, G. Torelli, T.P. Wangler, M. Weiss, F.C. Witteborn, CERN Report No. CERN/PSCC/86-2PSCC/P94,1986.

[83] F.C. Witteborn, and W.M. Fairbank, Rev. Sci. Instrum., **48**, 1 (1977).

[84] D.E. Dorfan, J. Eades, L.M. Lederman, W. Lee, and C.C. Ting, Phys. Rev. Lett.,**14**, 1003 (1965).

[85] H. Koch, Hyperfine Interact., **44**, 59 (1988).

[86] C.D. Johnson, and T.R. Sherwood, Hyperfine Interact., **44**, 65 (1988).

[87] H. Dehmelt, R.S. Van Dyck, Jr., P. Schwinberg and G. Gabrielse, Bull. Am. Phys. Soc. **24**, 757 (1979).